

**Timing and Analysis of Eclipsing Black Widow Pulsar
PSR J2256-1024**

by

Kathryn Crowter

M. Physics, University of Oxford, 2012

A THESIS SUBMITTED IN PARTIAL FULFILLMENT
OF THE REQUIREMENTS FOR THE DEGREE OF

Master of Science

in

THE FACULTY OF GRADUATE AND POSTDOCTORAL
STUDIES
(Astronomy)

The University of British Columbia
(Vancouver)

August 2018

© Kathryn Crowter, 2018

Abstract

Pulsars are rapidly spinning neutron stars emitting radiation about their magnetic field axes. Misalignment of the spin and magnetic axes causes a “lighthouse” effect where we observe radiation pulses, in time with the pulsar’s rotation. Millisecond pulsars are those which have accreted material from a companion star, spinning themselves up to rotate faster. Some millisecond pulsars occur in tight orbits with low mass companions; this combination can lead to the companion losing material, due to bombardment by energetic particles from the pulsar, presumably eventually destroying the companion. These pulsars are known as Black Widows (BWs). This thesis is an analysis of radio observations of PSR J2256-1024, a BW pulsar with a spin period of 2.294531816964939(10)ms.

Observing pulsars, we can calculate the arrival times of individual pulses and compare these with those predicted from various models to find the best-fitting one. This process is known as pulsar timing. We present the timing solution for PSR J2256-1024. We find it has a 5.1091831284(9)hr binary orbit with a semi-major axis of 4.1(3)ltsec and a 0.0312(9) M_{\odot} companion. PSR J2256-1024 shows a radio eclipse over 7.8 % of its orbit - approximately twice the size of the Roche lobe calculated for the companion. This confirms the picture of a Black Widow pulsar with material being stripped from the companion and forming a trailing cloud which blocks the pulsar signal. We also find evidence for variable clumps of material in the system.

We present polarization profiles and mean flux densities at 350 MHz, 820 MHz and 1500 MHz. We discuss polarization changes in the post-eclipse region, where the pulsar signal is transmitted through eclipsing material in the system, and find

evidence of Faraday rotation. At one epoch, synchronous measurements of excess dispersion and rotation measure lead to a detection of a $3.9(0.6)$ mG line-of-sight magnetic field. This field occurs an estimated minimum $3.3(0.3)$ companion-Roche-lobe-radii from the companion. We believe this is the first successful detection of a magnetic field component in eclipsing material within a Black Widow system.

Lay Summary

Here we present an investigation of an undead star. Two stars orbited each other peacefully until one ran out of fuel; it collapsed, went supernova, and died. The spinning remnant became a pulsar - a rapidly spinning, dead star emitting radiation in a beam. We detect this radiation (often radio waves) when this beam points at us, and therefore see pulses in sync with the pulsar's rotation.

The other star continued on with its life, however the pulsar began to consume it, stealing the companion's material and making itself spin faster. This thesis studies one such system where the pulsar is now actually destroying its companion. Material is blasted from the companion star into space forming a cloud trailing behind it. The cloud passes between us and the pulsar, causing eclipses.

This research measures the properties of the pulsar, its orbit with the other star, and investigates its eclipses.

Preface

Although this work presents the first official radio timing solution for PSR J2256-1024, this pulsar was not discovered by the author. In addition many others acquired the data analysed in this thesis.

- PSR J2256-1024 was originally discovered in the Green Bank Observatory's Robert C. Byrd Green Bank Telescope (GBT) 350-MHz Drift-Scan Survey.
- PSR J2256-1024 was identified as a pulsar candidate by former University of British Columbia (UBC) undergraduate Christie McPhee.
- A preliminary phase-connected timing solution was obtained by Ingrid Stairs.
- Data used in this analysis was taken with the GBT using Green Bank Astronomical Signal Processor (GASP) and Green Bank Ultimate Pulsar Processing Instrument (GUPPI). Observations were made by Jason Boyles, Ryan Lynch, Maura McLaughlin, Rachel Rosen, Ingrid Stairs, and Kevin Stovall.
- The software suite PSRCHIVE was used extensively during this research, as was the pulsar timing program TEMPO.

With the above exceptions, the work presented here is the original product of Kathryn Crowter, with immeasurably valuable support and feedback from Ingrid Stairs.

Table of Contents

Abstract	ii
Lay Summary	iv
Preface	v
Table of Contents	vi
List of Tables	x
List of Figures	xiii
Glossary	xvii
Acknowledgments	xix
1 Introduction	1
1.1 Pulsars	1
1.1.1 What is a Pulsar?	2
1.1.2 Millisecond Pulsars	4
1.1.3 Black Widows and Other Spiders	5

1.2	Effects from the Interstellar Medium	8
1.2.1	Dispersion Measure	8
1.2.2	Removing Dispersion Measure Effects	10
1.2.3	Rotation Measure	11
1.3	Timing	12
1.3.1	Pulse Profiles and the Anatomy of a Pulsar Timing Observation File	12
1.4	Polarization	13
1.4.1	Representations of Polarization	14
1.4.2	Polarization Sign Conventions	16
1.4.3	Polarization Calibration	18
1.5	This Thesis	21
2	Data and Processing	23
2.1	GASP and GUPPI	27
2.2	PSRCHIVE	28
2.3	Radio Frequency Interference Excision	28
2.4	Polarization Calibration	30
2.5	Rotation Measure Corrections	31
2.6	TOA Generation	32
2.6.1	Generating Standard Profiles	33
2.6.2	Generating TOAs	34
3	Timing	36
3.1	TEMPO and TEMPO2	36
3.2	Assumptions and Model Parameters	37

3.2.1	Clock Correction and Time Systems	37
3.2.2	Projecting onto the Solar-System Barycenter (SSB)	38
3.2.3	Binary Model	39
3.2.4	Dispersion Effects from the Sun	40
3.3	Error handling - EFAC, EQUAD and Reduced Chi Squared	41
3.4	Data Excluded from the Fit	42
3.5	Parameters Which Could not be Successfully Fit	43
3.5.1	Eccentricity	44
3.5.2	Rate of Change of Projected Distance from the Pulsar to the Center of Mass	44
3.5.3	Proper Motion	45
3.5.4	Further spin frequency and orbital frequency derivatives	45
3.5.5	DM Variations	46
4	Results	47
4.1	Timing Solution	47
4.1.1	Fit Parameters	47
4.1.2	Residuals	49
4.1.3	Derived Parameters	53
4.2	Eclipse Residuals	61
4.3	“Blips”	67
4.4	Rotation Measure	74
4.4.1	Pre-Processing	75
4.4.2	Measuring rotation measure (RM) with <code>rmfit</code>	75
4.4.3	Ionospheric Contributions	77

4.5	Polarization Profiles	78
4.6	Effects of the Eclipse and Blip on Polarization Profiles	84
5	Conclusion	101
	Bibliography	103
A	Supporting Materials	115

List of Tables

Table 2.1	Different configurations used to take data. All observations were taken using standard “timing” mode. All GASP data were taken using coherent dedispersion; all GUPPI data were taken in filterbank mode. Full Stokes refers to full polarization data being taken as opposed to just total intensity data.	25
Table 3.1	Assumptions, model parameters used in the fitting procedure to obtain the values in Table 4.1 and statistics on the input data . .	37
Table 3.2	Statistics for some parameters excluded from the final timing solution. $\eta = \text{value} / \sqrt{\chi_{red}^2} \times \text{uncertainty}$	43
Table 3.3	Values found for PMRA and PMDEC when included in the fit. All uncertainties given are those directly output by TEMPO . .	45
Table 4.1	Final fit parameters for 256 . Quantites in parentheses indicate the uncertainties in the last digits. Errors shown are as output by TEMPO - they have not been processed in any way except for rounding. F1 has not been corrected for galactic acceleration	48

Table 4.2	Derived parameters (i) using TEMPO fit parameters and physical constants alone, or an external model (ii) assuming the pulsar has a moment of inertia of 10^{38} kg m ² , (iii) assuming a pulsar mass of $1.4 M_{\odot}$ and an edge-on orbit with an inclination angle of 90° , and (iv) using the inclination angle of $68(11)^{\circ}$ and filling factor of $0.4(2)$ found in the optical counterpart detection paper [1]. Note the caveat about this filling factor in Subsection 4.1.3. Uncertainties shown have been propagated straight from those output by TEMPO	54
Table 4.3	Possible size of the eclipsing material, X , given the eclipse’s position in orbital phase and the derived semi-major axis (Subsection 4.1.3). The companion’s effective Roche Lobe diameter and its volume-averaged diameter (Subsection 4.1.3) are included for easy comparison	66
Table 4.4	Excess dispersion measure (DM) due to the clumps on Modified Julian Dates (MJDs) 55 181 and 55 191	72
Table 4.5	RM values from using the ”brute force” <code>rmfit</code> algorithm. GASP data has a narrower bandwidth and fewer frequency channels. As RM has a frequency squared dependence, those observations less useful to determine RM. They are shown to demonstrate that GASP RM values are consistent with their GUPPI counterparts for the same observation. The GASP data at MJD 55 191 was unable to be fully calibrated and so RM was not measured.	76
Table 4.6	RM values determined from the pulsar observations by the <code>rmfit</code> iterative algorithm and the average ionospheric contributions to the RM during those observations as computed by the <code>ionFR</code> code, which uses the International Reference Ionosphere (IRI) model for the ionosphere	77
Table 4.7	Mean flux densities found for each fully calibrated backend and frequency combination	83

Table A.1	Complete parameter file as output by TEMPO	116
Table A.2	Alternate values for parameters in Table 4.2, where \dot{F} has been corrected for galactic acceleration using the parallax distance. Only parameters whose values were altered are listed	117

List of Figures

Figure 1.1	Basic picture of the pulsar lighthouse model. Based on [2, Figure 3.1]	3
Figure 2.1	Orbital Phase and Central Frequency of the final residuals are plotted against MJD, showing the data span and coverage. GASP markers differ from the GUPPI ones solely for clarity in the three epochs where scans were taken simultaneously with the two backends	26
Figure 2.2	An example <code>pacv</code> plot of a calibrator file applied to itself, demonstrating depolarization near the edges of the frequency band. The calibration has been applied such that the calibrator has a total flux of 1. Total flux is shown in black, polarized flux is shown in red	29
Figure 2.3	An example calibrator solution, derived from a <code>cal</code> file taken on MJD 55 191, pointing at 256	32
Figure 3.1	Φ_{Sun} and Timing Residuals vs MJD	40
Figure 4.1	Timing Residuals vs MJD, folded into a span of one year to show data coverage for a parallax measurement. The eclipse (plus both ingress and egress) and the blip have been excluded.	49

Figure 4.2	Timing Residuals vs MJD. The eclipse (plus both ingress and egress) and the blip have been excluded.	50
Figure 4.3	Timing Residuals vs Orbital Phase. The eclipse (plus both ingress and egress) and the blip are excluded.	51
Figure 4.4	Higher time resolution close-up of eclipse observed on MJD 55 191 at 350 MHz: Timing Residuals vs Orbital Phase	62
Figure 4.5	Higher time resolution close-up of eclipse observed on MJD 55 181 at 820 MHz: Timing Residuals vs Orbital Phase	63
Figure 4.6	Higher time resolution close-up of eclipse observed on MJD 55 226 at L-band: Timing Residuals vs Orbital Phase	63
Figure 4.7	Higher time resolution close-up of all eclipses observed: Timing Residuals vs Orbital Phase	64
Figure 4.8	Higher time resolution close-up of all eclipses observed: Timing Residuals scaled to give an “Excess DM” vs Orbital Phase. GUPPI L-band data has been excluded for clarity. Vertical lines indicate the location of the eclipse in orbital phase, determined by eye from this plot	65
Figure 4.9	Plots of the “blip” on both MJDs on which it was seen, with each backend	68
Figure 4.10	Higher Time Resolution Close-up of the Eclipse and Blip on MJD 55 181 at 820 MHz	69
Figure 4.11	Higher Time Resolution Close-up of the Eclipse and Blip on MJD 55 191 at 350 MHz	70
Figure 4.12	Higher Time Resolution Close-up of the Eclipse on MJD 55 226 at L-band	70

Figure 4.13	Higher Time Resolution Close-up of the Blip vs Orbital Phase - Data from MJDs 55 181, 55 191 and 55 226 taken at 820 MHz, 350 MHz and 1500 MHz respectively. The GUPPI MJD 55 226 data is omitted from this plot for purposes of clarity - the large error bars obstructed the view of the other data sets	71
Figure 4.14	Higher time resolution close-up of blips observed: “Excess DM” vs Orbital Phase. GUPPI L-band data has been excluded for clarity	73
Figure 4.15	Higher time resolution close-up of the blips recorded on MJDs 55 181(820 MHz) and 55 191(350 MHz): “Excess DM” vs Or- bital Phase	74
Figure 4.16	Polarization profiles for 256 at 350 MHz on MJD 55 191	80
Figure 4.16	Polarization profiles for 256 at 820 MHz on MJD 55 181	81
Figure 4.16	Polarization profiles for 256 at L-band on MJD 55 226	82
Figure 4.17	Higher time resolution close-up of polarization parameters in the GUPPI 820 MHz eclipse region. All left-hand plots show the total intensity I for reference	86
Figure 4.18	Higher time resolution close-up of polarization parameters in the GASP 820 MHz eclipse region. All left-hand plots show the total intensity I for reference	87
Figure 4.19	Higher time resolution close-up of polarization parameters in the GUPPI 350 MHz eclipse region. All left-hand plots show the total intensity I for reference. The horizontal white line is where sub-integrations were zero-weighted due to radio fre- quency interference (RFI)	88
Figure 4.20	Higher time resolution close-up of polarization parameters in the GASP 350 MHz eclipse region. All left-hand plots show the total intensity I for reference. The horizontal white line is where sub-integrations were zero-weighted due to RFI	89

Figure 4.21	tscrunch map of Ψ at 350 MHz on MJD 55 191 next to over-plotted polarization position angle (PA) plots for select sub-integrations, both zoomed in on the pulse	92
Figure 4.22	tscrunch polarization profiles for select sub-integrations at 350 MHz on MJD 55 191	93
Figure 4.23	tscrunch map of Ψ at 820 MHz on MJD 55 181 next to over-plotted PA plots for select sub-integrations, both zoomed in on the pulse	94
Figure 4.24	tscrunch polarization profiles for select sub-integrations at 820 MHz on MJD 55 181, zoomed in on the baseline to make changes in L more apparent	95
Figure 4.25	Fits for the PA profile of select sub-integrations (on MJD 55 191 at 350 MHz) to determine the PA shift. A quadratic was fit to the PA data from the total polarization profile (Figure 4.16), then only the y-intercept was allowed to vary as the fit was performed on the sub-integrations shown. Solid lines show the resulting fits and the range over which the functions were fit. Differentiating between fit lines for sub-integrations 21, 22 and 23 may be difficult as their offsets are very close	97
Figure A.1	Higher time resolution close-up of all eclipses observed: “Excess DM” vs Orbital Phase	118

Glossary

BIPM	Bureau International des Poids et Mesures
BW	Black Widow
COM	center of mass
DM	dispersion measure
FERMI	Fermi Gamma-ray Space Telescope
FPGA	field programmable gate array
GASP	Green Bank Astronomical Signal Processor
GBT	Green Bank Observatory's Robert C. Byrd Green Bank Telescope
GPS	Global Positioning System
GUPPI	Green Bank Ultimate Pulsar Processing Instrument
I	Intensity
IAU	International Astronomical Union
IEEE	Institute of Electrical and Electronics Engineers
IGM	Intergalactic Medium
IRI	International Reference Ionosphere
ISM	interstellar medium

JPL	NASA Jet Propulsion Laboratory
L	linear polarization
LCP	left-handed circular polarization
LMXB	Low-Mass X-ray Binary
MJD	Modified Julian Date
MSP	millisecond pulsar
NRQZ	United States National Radio Quiet Zone
NTT	New Technology Telescope
PA	polarization position angle
RB	Redback
RCP	right-handed circular polarization
RFI	radio frequency interference
RM	rotation measure
RMS	root mean square
SNR	signal to noise ratio
SPIGOT	Green Bank Telescope Pulsar Spigot
SSB	Solar-System Barycenter
TDB	Barycentric Dynamical Time
TOA	Time-of-Arrival
TT	Terrestrial Time
UTC	Coordinated Universal Time
WRMS	weighted root mean square
XB	X-ray Binary

Acknowledgments

This time three years ago I couldn't integrate, differentiate, or go shopping with a list and come back with everything on it. This thesis and any future I have in astrophysics would not exist without the help and patience of some amazing people. With all of my heart, thank you.

I'd like to thank Ingrid Stairs for her steadfast support, insight, and slightly terrifying level of expertise. It continues to be a joy to work with you and I will always be grateful.

Thanks also go to members of the pulsar group at UBC, both past and present, who provided their friendship, laughter, road trip anecdotes, and a fair share of both suggestions and commiserations. Also to Joss Ives for working both with and around me, allowing me to rediscover how much I like teaching when a class full of students still felt like an attack.

I'd like to express my gratitude for my Canadian family (in whichever country you currently reside): you all made The House feel like a home (and one that was filled with fun, love, and gummy bear murders).

Last (but in no way least), I'd like to thank my family. I can't begin to count the ways you've supported me, loved me, and enriched my life - thank you!

Chapter 1

Introduction

1.1 Pulsars

Pulsars were discovered in 1967 [3]. Bell saw a series of radio pulses, with a remarkably short, accurate and stable period. Something this ordered and consistent would usually be human in origin, but Bell noted it was keeping sidereal time, implying an astronomical source. The signal was determined to be coming from something inside our galaxy but far outside the solar system.

Interference or possible faults with the telescope were painstakingly ruled out. The possibility of extra-terrestrial life, perhaps a beacon of some kind, was considered but also ruled out [4]¹. Bell found 3 other instances of these ordered signals, solidifying the discovery, and left us with the detection of a new phenomenon: pulsars.

After the initial detection the race was on to determine the source of these signals. It soon became clear [5, 6] that they were coming from neutron stars. These had been proposed by Baade and Zwicky an impressive 33 years earlier [7, 8] but were largely been dismissed as (if they existed) too faint to be detected.

¹sparking a fair few nicknames - the first pulsar was unofficially known as LGM-1 (Little Green Men - 1)

There was a lot of excitement over these objects among astrophysicists and astronomers. A new phenomenon to explore and discover is always exciting, but pulsars also had the makings of physicist dream objects - accurate clocks in space, and often in interesting environments. They have since been used to indirectly detect gravitational waves [9], to detect the first planets in an extrasolar system [10], and to indicate the Earth's position in space on the Pioneer Plaque, to name just a few.

1.1.1 What is a Pulsar?

A pulsar is a neutron star $\approx 1.4M_{\odot}$ with a radius of ≈ 12 km, spinning. The slowest radio pulsar currently known spins once every 8.509 827 491 s [11], the fastest spins just over 716 times every second² [12].

Pulsars are born in core-collapse supernovae. Stars resist collapsing under their own gravity by generating energy from nuclear fusion. They begin by fusing hydrogen to make helium in their core where the temperature and pressure is high enough for these reactions to occur. Once a star runs out of hydrogen in its core, that core contracts under gravity, also increasing its temperature and pressure. This then heats the surrounding hydrogen which ignites hydrogen fusion in a shell around the core. Helium produced is added to the core, causing it to heat further and further until it's hot enough for helium to start fusing. At this point the star is burning helium in its core (producing carbon and oxygen) with a lower temperature hydrogen-burning shell outside, transitioning into just hydrogen further out where it is too cool for fusion. What happens from here depends on the star and its mass but for those $\gtrsim 8M_{\odot}$ this process continues in a similar fashion until the star has an onion-like structure - a hydrogen envelope surrounding layers of fusion end-products, separated by shells where fusion is occurring, all surrounding an iron core.

The star, out of fuel and unable to balance the force of gravity, undergoes a core-collapse supernova after which is left either a black hole or a neutron star. Before collapse the star likely had some angular momentum and magnetic field

²that's faster than a blender!

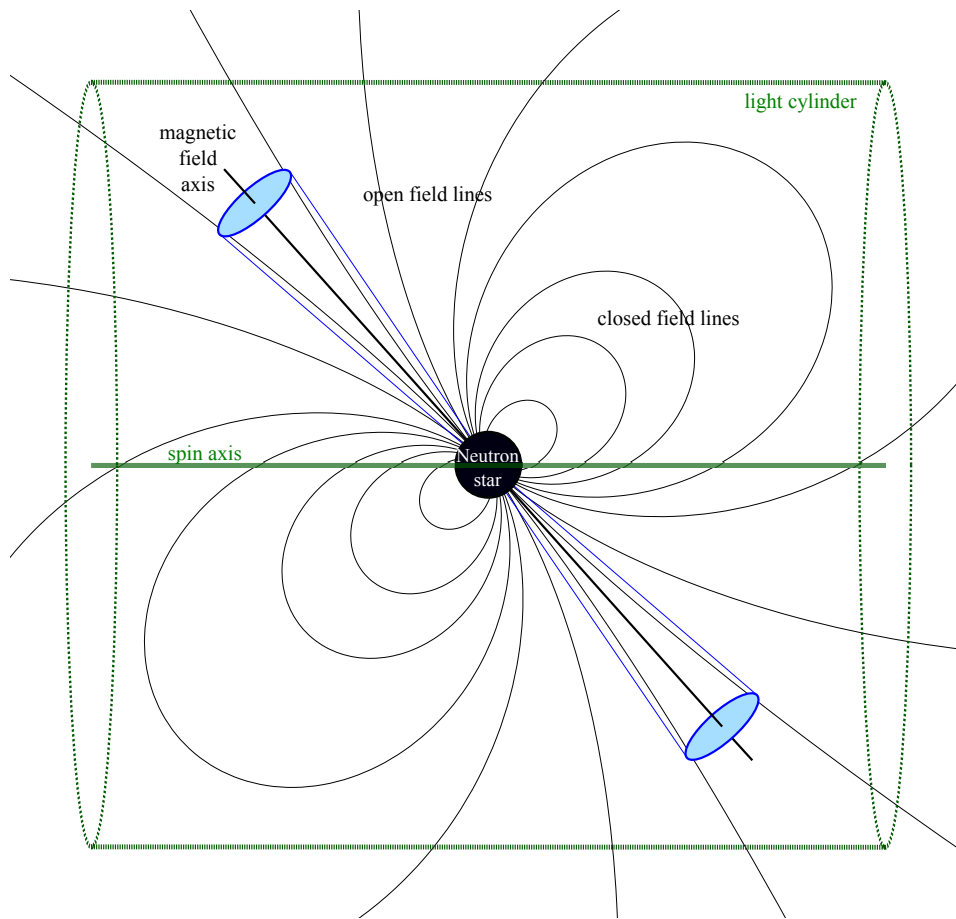


Figure 1.1: Basic picture of the pulsar lighthouse model. Based on [2, Figure 3.1]

which are conserved when the star shrinks. So, as a basic picture³, when the star collapses from a radius $\approx 10 \times 10^5$ km to ≈ 10 km its area decreases by a factor of $\approx 10 \times 10^{10}$ meaning the magnetic field and rate of rotation increase by a factor of $\approx 10 \times 10^{10}$.

This combination of fast rotation and a large magnetic field leads to radiation

³core-collapse supernova are an active area of research and precisely how a star goes from an onion-like structure to either a neutron star or a black hole, and what determines properties such as radius and spin of that end product, is not fully known. For a not-yet-outdated state of research, which also points to further resources, see Adam Burrows' review [13]

being emitted about the magnetic poles of the pulsar. The exact emission mechanism for this radiation, and particularly for the radio emission, is still unclear [14–16]. The basic picture is that pulsars possess a dense magnetosphere containing plasma. Charged particles follow magnetic field lines which co-rotate with the pulsar. However beyond a certain distance away from the pulsar co-rotating would mean travelling faster than the speed of light which is not possible. This boundary surface is referred to as the *light cylinder*. Within the light cylinder field lines can close but field lines that cross the light cylinder cannot, leading to open field lines and a stream of escaping charged particles. This combination of magnetic fields, acceleration and charged particles around the magnetic poles leads to a beam of radiation.⁴

In any case, electromagnetic radiation is emitted about the magnetic field axis. Figure 1.1 shows the classic picture of a pulsar modelled as a magnetic dipole. Radiation is emitted in beams around the magnetic poles and the magnetic axis is misaligned with the rotation axis producing a "lighthouse" effect. In this picture the beam only crosses the line of sight once per revolution⁵, producing a pulse every time it points at us - so we see pulses repeating with the same period as the pulsar's rotation, thus the name "pulsars". In this picture the electromagnetic emission is powered by the pulsar's rotation, and so as energy is lost over time its rotation is gradually slowing down. Its period will get longer and longer until it is spinning too slowly to accelerate particles enough that they emit radiation; the pulsar dies and *turns off*. For a more in-depth picture on the above (and much more besides) see *The Handbook of Pulsar Astronomy* [2] and *Neutron Stars and Pulsars* [19].

1.1.2 Millisecond Pulsars

How a pulsar slows over time and eventually dies, as stated in Subsection 1.1.1 assumed that the pulsar was born from a single star, forming an isolated young pulsar. However many stars are in binary systems and therefore many pulsars are born in binary systems which affects how they age and evolve.

⁴A couple of classic papers on the subject are Goldreich and Julian [17] and Ginzburg et al. [18]

⁵twice if the axes are misaligned by an angle close to 90° - how close depends on how wide the radiation beam is.

As mentioned, pulsars are born in supernovae. A supernova will eject a lot of mass from the system and changing the pulsar's mass will alter the binary orbit. From Virial Theorem considerations, if the mass ejected in the supernova made up more than half of the total system mass then the binary will be disrupted. If the supernova was asymmetrical (which is thought to often be the case) then the pulsar will be given a *kick* by the supernova giving it some additional velocity. If both of these things occur then the result is an isolated young pulsar moving through space with a high velocity.

If the binary is not disrupted, a kick usually results in a more eccentric orbit. Now the companion evolves while in this binary orbit with the pulsar. The evolution path from this point depends on the properties of pulsar, the companion, the binary orbit and the environment (e.g., if the system is in a globular cluster) and there are many possibilities [20–23]. Some evolution paths result in the pulsar being able to steal material from its companion, for instance if that companion overfills its Roche Lobe. If the pulsar can accrete material from the companion it will increase its own angular momentum (increasing its spin) at the expense of the orbital angular momentum of the binary system. This process as the pulsar is *spun up* is known as *pulsar recycling*; the longer it goes on the shorter the spin period of the pulsar becomes. This is how millisecond pulsars (MSPs), also called “old pulsars” or “recycled pulsars”, are formed. The current picture, confirmed by J1023+0038 [24], is that during this accretion stage the system is an X-ray Binary (XB), a binary detected in X-rays. With in-falling matter inhibiting the production of radio emission from the pulsar and forming emitting X-rays. Then after the spinning up phase the pulsar would “turn on”.

1.1.3 Black Widows and Other Spiders

Of the approximately 2600 pulsars [25][26] currently known about 10 % are MSPs. Of these 10 %, a few are “spider” pulsars [27] termed *Black Widows (BW)s*, *Redbacks (RBs)* and also a newer subsection, *tidarrens*.

These spider pulsars are all MSPs in tight binary orbits with low mass companions and earned their monikers from how they behave towards those companions.

Black widow female spiders are notorious for killing their mates; with pulsars BWs are systems where the companion is being destroyed by the pulsar. Pulsars give off a stream of charged particles accelerated to relativistic speeds known as a *pulsar wind* and this wind is ablating, presumably eventually destroying, the companion. The strength of a pulsar wind varies between pulsars; these companions are being destroyed so significantly due to particularly high winds and/or features of the companion star. In BW systems companions are closer to the pulsar than in many others due to the tight binary orbit and those companions are also lighter and less dense making them more prone to losing material.

The original BW is B1957+20. It was discovered in 1988 [28] at 430 MHz, an MSP with a period of 1.6 ms and a binary period of 9.17 h. It was observed that the pulsar signal was eclipsed for about 50 minutes each orbit, and during the few minutes preceding an eclipse and for at least 20 afterwards the signal was delayed. A minimum companion mass of $0.022 M_{\odot}$ was inferred from the timing solution (the current value is $0.021423 M_{\odot}$ [29]). These eclipses indicated plasma and material in the orbit much larger than the Roche lobe of the companion and this, along with the asymmetry of the dispersive smear around the eclipse, lead to the proposal that the companion was in fact being evaporated by its pulsar. More evidence has been gathered since to support this such as; optical observations showed an orbital variation of the luminosity consistent with the bright side of the companion always facing the pulsar [30][31], a $H\alpha$ emission nebula was detected confirming the presence of a pulsar wind [32], X-ray observations of a point source with a strong binary-phase dependence implying an intra-binary shock where the pulsar wind meets the ablated material from the companion [33] and X-ray observations which resolves emission from both a point source and a tail [34].

The only currently known way for an MSP to form is with the help of another star, however isolated MSPs with no companion also exist. These recycled pulsars must have formed in binary systems but are now alone. There are several proposed mechanisms for how this could happen. The binary may have been disrupted (e.g., by the companion going supernova or an interaction with a third body). With the discovery of the initial BW it was proposed that their companions had been evaporated and these isolated MSPs were formerly BWs. However some BWs have

been measured with companion mass-loss rates implying evaporation time-scales longer than the age of the universe, so while isolated MSPs may be the endpoint for some BWs, this cannot be true for all of them.

So what defines a pulsar as being a Black Widow? Ideally the definition would be this companion-destroying behaviour but, while intuitive, this poses a problem when the only information we have about pulsar systems is empirical. The definition of a BW used to require radio eclipses but that is no longer the case⁶, but a radio eclipse is still strong evidence for a BW system. Some refer to cases where eclipses have been detected as “true” or “canonical” BWs. Generally a system may be called a BW if it is a true MSP with $P \sim \text{ms}$, in a close binary e.g., $P_B < 1 \text{ d}$, and a low companion mass $M_C \ll 0.1 M_\odot$. BW systems also tend to have very circular orbits. There are currently 38 known black widows and a further two candidates [36].

It is thought that Low-Mass X-ray Binaries (LMXBs) are likely progenitors of Black Widows. Low mass, faint companions in an XB are associated with older stars; these systems are likely older too, allowing for pulsar recycling to happen for longer time spans and resulting in MSPs on the faster end of the spectrum. This prolonged period of mass-transfer also allows enough time for the binary orbit to be circularized by tidal interactions. The expected result would be fast pulsars in tight, very low eccentricity orbits which are the exact characteristics found for BWs. Evolution modelling for LMXBs supports this scenario [37, 38]

Redback spiders are the Australian cousins of Black Widows. RB pulsars seemed to display features similar to BWs (such as similar orbital periods, and eclipses) but also had some key differences. The major difference being companion masses in RB systems, while still low, are much larger than those for BWs with $M_c \approx 0.2 - 0.4 M_\odot$. At first it was unclear whether RBs were different from BWs or simply the other end of the companion mass scale in the same population, but with the discovery of more systems a clear bimodal distribution for the companion masses emerged.

⁶for example at low inclination angles where the orbit is face on, the pulsar could still be destroying its companion but resulting the material will likely be in or around the plane of the orbit, making eclipses unlikely [35]

There was also a proposal that RBs were the progenitors of BWs. There is some disagreement between in current research (using binary evolution models) as to whether this is the case. Some favour the two evolving from LMXBs[39] in separate paths and others favour all BWs resulting from RBs (although not all RBs ending up as BWs) [40].

Evidence for a connection between LMXBs and RBs is now quite strong; in 2009 a “missing link” object between radio pulsars and X-ray Binary was identified, J1023+0038 [24]. J1023+0038 is a Redback and had previously been detected with an accretion disk but no evidence of one was found in 2009, “suggesting that the radio MSP has turned on after a recent LMXB phase.” Other RBs transitioning between pulsar states and LMXBs have since been found such as J1227-4853 [41] and J1824-2452I (M28I) [42] and the search is on to find more (or a transitioning BW) [43].

In addition to BWs and RBs, some have also started to make a further distinction for cases where the companion mass is incredibly low, e.g., J1311-3430 whose minimum companion mass is $0.008210 M_{\odot}$ [44]. These are the more recently termed tidarren pulsars, named for another species of spider - the *Tidarren sisypoides* whose males are 1 % the size of the females, and also meet an unfortunate end during mating.

1.2 Effects from the Interstellar Medium

1.2.1 Dispersion Measure

The pulsar signal is emitted over a range of frequencies and travels to us through the interstellar medium (ISM)⁷ which is a low density plasma. Different frequencies of light travelling through a plasma “see” different refractive indices and therefore travel at different speeds (with lower frequencies travelling slower). Therefore the pulse of a pulsar signal is delayed at lower frequencies relative to higher ones. If there is a range of frequencies present, just adding data from each frequency to-

⁷assuming a galactic pulsar and a detector in our solar system (probably on Earth). Signals from extragalactic pulsars would also travel through the Intergalactic Medium (IGM)

gether will result in a smeared and broadened pulse shape. Separating this effect from the original pulse shape is desirable, for studying the pulsar and its emission, for examining the ISM the signal passed through and for more accurately determining when the pulse arrived.

It can be shown [2] that a radio signal travelling a distance d through a homogeneous plasma, in the absence of a magnetic field, will be delayed by a time, t , of

$$t = \frac{1}{c} \int_0^d \left(1 + \frac{v_p^2}{2v^2} \right) dl - \frac{d}{c}$$

relative to an infinite frequency signal, where c is of course the speed of light in a vacuum, v is the frequency of the signal, v_p is the plasma frequency, a quantity dependent on the characteristics of the plasma. v_p is given by:

$$v_p = \sqrt{\frac{e^2 n_e}{\pi m_e}}$$

with n_e being the electron number density, e the charge of an electron and m_e the electron rest mass. And so

$$t = \frac{e^2}{2\pi m_e c} \frac{DM}{v^2} \quad (1.1)$$

with dispersion measure (DM) being expressed as

$$DM = \int_0^d n_e dl$$

Note the $1/v^2$ dependence of the time delay and that this means the effect is larger when looking at lower frequency bands. Also note that DM is then an integral of the electron number density along the line of sight to the pulsar and, with a model for n_e in the galaxy such as YMW16 [45, 46] or NE2001 [47, 48], a distance to the pulsar can be estimated.

1.2.2 Removing Dispersion Measure Effects

In real life there is no such thing as a single frequency pulse of radiation, there is always some spread of frequency values, some bandwidth⁸. This means that dispersion will always affect the measured pulsar signal and should be accounted for.

There are two principal methods for dedispersing pulsar observations, incoherent dedispersion (sometimes referred to as filterbank dedispersion) and coherent dedispersion. Incoherent dedispersion uses a filterbank to split the bandwidth up into frequency channels with a smaller width. The pulse is detected in each channel and then shifted to account for the delay, however there will still be dispersive smearing within the channels themselves.

Coherent dedispersion, pioneered in 1975 [49], removes the smearing within each channel. This completely eliminates the dispersive effect of the ISM and recovers the signal with the same time resolution with which it was measured.

With this method the ISM is taken to be a low density, cold, electron plasma and modelled as a filter applied to the pulsar signal. For MHz frequencies this model gives a transfer function (in the frequency domain) of

$$H(\nu) = \exp\left(2\pi i \frac{\text{DM}}{2.41 \times 10^{-4} \text{ sMHz}^2} \frac{\nu_1^2}{\nu_0^2 \nu}\right)$$

where ν_0 is the central frequency of the observation, ν_1 is the offset between the frequency being considered and ν_0 ($\therefore \nu = \nu_0 + \nu_1$), and $2.41 \times 10^{-4} \text{ sMHz}^2$ is a measured proportionality constant [50]. For a full derivation see Hankins and Rickett [49].

To recover the initial electric fields of the signal, the measured electric fields need to be convolved with the inverse of the filter. By the convolution theorem of Fourier transforms, we can do this by transforming the raw voltages (proportional to the original electric fields received by the telescope) into the frequency domain,

⁸pulsed radiation being emitted in a range of frequencies may be due to all sorts of reasons, but the impossibility of a monochromatic pulse comes from the properties of the Fourier transform - such a "pulse" would need to be infinite in time

multiplying by the inverse transfer function of the ISM filter, then performing an inverse Fourier transform back into the time domain, i.e.,

$$E_{recovered}(t) = \mathcal{F}^{-1}\{\mathcal{F}[E_{measured}(t)] \times H^{-1}(f)\}$$

This is computationally intensive, plus as this process requires the phase information from the electric fields it must be performed on the raw voltages rather than after they have been squared to give a measure of intensity. This is why coherent dedispersion took some time before it was routinely implemented, despite being conceived in 1972, and why it cannot be applied to archival data where the phase information has been lost.

1.2.3 Rotation Measure

When discussing the radio signal from the pulsar's path through the ISM in Subsection 1.2.1 it was assumed that there were no magnetic fields or that any magnetic effects were negligible. Of course it has been well established that there is a galactic magnetic field [51].

When a polarized electromagnetic wave travels through a magnetic field (which has a non-zero component in the direction the wave is travelling) the angle of that polarization is rotated; this is known as *Faraday rotation*. The size of this rotation is dependent on the magnitude of the magnetic field parallel to the direction of propagation, B_{\parallel} , weighted by the electron density, and the frequency of the wave. The change in polarization position angle, Ψ , can be expressed as

$$\Delta\Psi = \lambda^2 RM$$

where

$$RM = \frac{e^3}{2\pi m_e^2 c^4} \int_0^d n_e B_{\parallel} dl$$

and is known as the rotation measure [2]. Pulsar signals in general are highly polarized and the Faraday rotation experienced by the signal can be measured⁹ and

⁹In fact pulsar measurements of Faraday rotation have been used as a probe of the Galaxy's

corrected for.

1.3 Timing

Pulsar timing and timing models are how we go from astronomical objects giving off radiation to those accurate clocks in space of Section 1.1 and the measurements, information and exciting discoveries they can provide.

Pulsar timing is the process of observing pulsars, extracting information about when the pulses arrived, then using these measurements to obtain information about the pulsar itself, its motion, and the medium between Earth and the pulsar. It is also a term used to distinguish using pulsar measurements as tools from other areas of pulsar research such as pulsar searches, population studies, and theory.

1.3.1 Pulse Profiles and the Anatomy of a Pulsar Timing Observation File

Individual pulses from the same pulsar can vary wildly in shape and have high levels of noise. This is why, once the period of the pulsar is known, the data are *folded*, averaging many pulses together. This is done by cutting up the data stream into segments with the length of the period and stacking those segments together to form an averaged pulse.

Folding the data stream with the period leads to a (mostly)¹⁰ stable profile shape rising out of the noise. This stable *integrated pulse profile* (sometimes also called an averaged profile or standard profile) will be characteristic of that pulsar for the given observing frequency and is key to pulsar timing.

When data are taken for timing purposes, after dedispersion, small segments of time are folded together to make *sub-integrations* so one observation is made up of multiple sub-integrations which follow on from each other and each one has enough individual pulses contained within them for the stable profile shape to

magnetic field [52]

¹⁰shape changes in average pulse profiles and mode changing between distinct profile shapes are an active area of pulsar research, shedding light on factors such as emission beam geometry and evolution [53, 54]

emerge. A typical sub-integration for PSR J2256-1024 might be 10 s long which would correspond to just over 4358 single pulses.

Of course many sub-integrations can be averaged or *scrunched* together to form an even clearer integrated pulse profile. This is done to form a *standard profile* for that frequency which is compared with individual sub-integration profiles, by cross-correlating in the frequency domain [55], to form a *Time-of-Arrival (TOA)* for that sub-integration. These TOAs are the key tool of pulsar timing.

In order for a timing solution to be found it must be *phase connected* meaning that every single rotation of the neutron star must be accounted for between observations. This is quite impressive considering the data taken from some pulsars spans decades, and one of the things that can make TOAs and pulsar timing such a powerful tool.

The aim is for the timing model to constrain every factor that could affect TOAs: the pulsar's position and motion, including binary parameters if relevant, the position and motion of the Earth, the medium the pulse travels through, characteristics of the pulsar such as its spin period, and many others. This timing model is then used to create predicted TOAs - when the model predicts the TOAs should arrive - and compare those with the actual TOAs recorded, producing residuals. Ideally the model will account for every possible affect influencing the TOAs, the data would match the predicted values exactly, and the residuals will be perfectly flat at zero (with some uncertainty). This is very unlikely to occur but the aim is still flat residuals as close to zero as possible, for example any periodic pattern in the residuals or an increasing deviation from zero are classic signs of a badly fit value or a missing parameter in the model.

1.4 Polarization

In electromagnetic radiation, polarization describes the direction of the electric field vector, \vec{E} , in the plane perpendicular to the direction of propagation (also known as the plane of polarization), and how that changes with time. This topic is covered in an array of textbooks such as Born and Wolf [56], Tinbergen and

Jaap [57] and review articles Trippe [58]. For a heuristic review with a focus on applications to radio astronomy this author recommends [59].

If \vec{E} 's direction is changing randomly in time the wave is said to be unpolarized or randomly polarized. If \vec{E} is behaving in a predictable way then the wave is said to be polarized. For behaviour between the two extremes, the wave is said to be partially polarized and the amount of predictability is expressed through the *degree of polarization*.

If \vec{E} 's direction is confined to a line that \vec{E} is oscillating back and forth along, the radiation is linearly polarized. It is clearly possible to express \vec{E} in terms of components in two orthogonal directions, say \vec{E}_x and \vec{E}_y . This is the basic idea of how linear polarization feeds in a telescope work - measuring the polarization along two orthogonal, linear directions, one in each receiver. This is also known as expressing the polarization in a linear basis.

If the polarization is completely linear, there will be no phase difference between \vec{E}_x and \vec{E}_y . If there is a 90° phase difference between the two (with either \vec{E}_y leading \vec{E}_x or \vec{E}_x leading \vec{E}_y) then \vec{E} will trace out a circle in the plane of polarization. \vec{E} will be moving clockwise or anticlockwise around the circle depending on whether \vec{E}_x or \vec{E}_y is leading. These two cases are known as left-handed circular polarization (LCP) and right-handed circular polarization (RCP) and also make up an orthogonal basis which can be used to describe and measure polarization¹¹.

In the more general case of some other phase difference between \vec{E}_x and \vec{E}_y , \vec{E} will trace out an ellipse in the plane of polarization. This can also be thought of as a combination of linear and circular polarizations.

1.4.1 Representations of Polarization

There are two widely used systems to represent the polarization of electromagnetic waves. One was already referenced above - expressing \vec{E} in terms of two orthogo-

¹¹there has been some purposeful vagueness here as to which direction corresponds to LCP and which to RCP; it is covered in Subsection 1.4.2

nal polarization basis vectors. For example

$$\vec{E} = \begin{pmatrix} E_a(t) \\ E_b(t) \end{pmatrix} \quad (1.2)$$

Where $\begin{pmatrix} 1 \\ 0 \end{pmatrix}$ represents one basis polarization, e.g., horizontal, and $\begin{pmatrix} 0 \\ 1 \end{pmatrix}$ represents the other, e.g., vertical. This is known as the Jones representation of the polarization introduced in 1941 [60]; linear transformations of \vec{E} (e.g., if the signal was put through an amplifier and experienced a gain) can be represented as a matrix such that

$$\vec{E}' = \mathcal{J} \vec{E}$$

where \vec{E}' is the transformed, measured electric field vector, \vec{E} is the initial, input electric field vector and \mathcal{J} is known as the Jones matrix.

The major downfall of the Jones representation is not allowing for descriptions of partially or unpolarized waves; this is where the Stokes representation comes in. Here the polarization is expressed in terms of the Stokes parameters, first proposed in 1852 [61], and the Stokes vector:

$$\mathbf{S} = \begin{pmatrix} I \\ Q \\ U \\ V \end{pmatrix}$$

I is the total intensity of the wave, Q , U , and V describe the polarization. The degree of polarization, P , is given by

$$P = \frac{\sqrt{Q^2 + U^2 + V^2}}{I}$$

Q and U specify the linear polarization. The total linear polarization (L) is given by

$$L = \sqrt{Q^2 + U^2}$$

Note this is the mathematical representation of L, measuring L using this scheme

causes a bias [62]. How one removes this bias is discussed in Everett and Weisberg [63]

V then specifies the circular polarization.

In an analogous way to the Jones representation, transformations to the wave can be expressed by a transformations of the Stokes vector by the *Mueller matrix*, \mathcal{M} , like so:

$$\mathbf{S}' = \mathcal{M}\mathbf{S}$$

1.4.2 Polarization Sign Conventions

Polarization sign conventions involving the exact definition of which circular basis is left-handed, and how LCP and RCP relate to the Stokes V , is the subject of some controversy and confusion¹².

This seems to have four main contributing factors:

1. Variations in the initial definition of LCP and RCP
2. A mismatch between definitions of the Stokes V by the International Astronomical Union (IAU) and seminal radio astronomy books and papers, which can be further confused by 1.
3. These definitions also affect the sign convention of the polarization position angle which is sometimes not accounted for.
4. Vagueness (or no information) about the definition being used.

The definition used in this analysis is the one implemented by the PSRCHIVE software suite [65]. It uses the Institute of Electrical and Electronics Engineers (IEEE) definition of RCP and the Kraus and Tiuri [66] definition for Stokes V - positive for LCP. It should be noted that the IAU uses the same IEEE definition of RCP, but has the opposite sign convention for Stokes V .

¹²Should you wish to dive into the subject, I recommend Section 2.4.2 of Timothy Robishaw's dissertation [64]

The following describes the IEEE and IAU definition for RCP. From the point of view of an observer looking up into the sky at an oncoming wave, we define a right-handed orthogonal coordinate system with \hat{z} pointing towards the observer (and therefore along the direction of propagation), \hat{x} pointing towards North, and \hat{y} pointing towards East. When measured in one location, the observer will see the \vec{E} of a RCP wave moving in the counter-clockwise direction¹³. This corresponds to the electric field along the x-axis, E_x leading that along the y-axis, E_y .

If we were measuring an incoming wave in a linear basis which could be described by the \hat{x} and \hat{y} axes above, we can write:

$$\vec{E} = \begin{pmatrix} E_x \\ E_y \end{pmatrix} = \begin{pmatrix} |E_x| e^{i(\omega t + \phi_x)} \\ |E_y| e^{i(\omega t + \phi_y)} \end{pmatrix} \quad (1.3)$$

The Stokes parameters are then formed by the following relations [56, 66]:

$$\begin{aligned} I &= \langle E_x E_x^* \rangle + \langle E_y E_y^* \rangle \\ Q &= \langle E_x E_x^* \rangle - \langle E_y E_y^* \rangle \\ U &= \langle E_y E_x^* \rangle + \langle E_x E_y^* \rangle = 2\Re\{\langle E_y E_x^* \rangle\} \\ V &= i(\langle E_y E_x^* \rangle - \langle E_x E_y^* \rangle) = 2\Im\{\langle E_y E_x^* \rangle\} \end{aligned} \quad (1.4)$$

Where * denotes a complex conjugate and $\langle \rangle$ an ensemble average. In the case of a monochromatic wave being evaluated instantaneously, these expressions can be expanded using Equation (1.3) to give:

$$\begin{aligned} I &= |E_x|^2 + |E_y|^2 \\ Q &= |E_x|^2 - |E_y|^2 \\ U &= 2|E_x|^2 |E_y|^2 \cos(\phi_y - \phi_x) \\ V &= 2|E_x|^2 |E_y|^2 \sin(\phi_y - \phi_x) \end{aligned}$$

¹³it follows that the wave forms a *left-handed* helix in space along the direction of propagation

From these it is clear that Stokes V will be positive for LCP, when $\phi_y > \phi_x$ which corresponds to E_y leading E_x in Equation (1.3) and within the coordinate system described above.

The $\langle E_i E_j^* \rangle$ of Equation (1.4) are measurable quantities. In radio astronomy, if using a filterbank this is done by *crossing* the feeds from each receiver using a correlator. The complex conjugate is formed by introducing a 90° phase delay. If using coherent dedispersion the 90° phase delay is introduced when the electric fields are first sampled. The signals can then be stored as complex time series, preserving the full phase and amplitude information for later multiplication.

We also define the polarization position angle, Ψ , which describes the orientation of the linear part of the polarization. Here Ψ is taken as starting from North and increasing towards East in the coordinate system described above. With this definition Ψ can be formed from the Stokes parameters like so:

$$\Psi = \frac{1}{2} \tan^{-1} \left(\frac{U}{Q} \right)$$

1.4.3 Polarization Calibration

The measured polarization will not be the same as the intrinsic polarization. Differences come from several sources, the rotation of the telescope receivers with respect to the sky, the receivers themselves and their imperfections, different signal paths and amplifications for each polarization feed. These alterations of the pulsar signal should be accounted for and removed via calibration wherever possible.

The effect of each of these factors on the signal can be described with an individual Mueller matrix. A total matrix can then be formed to give the entire transformation from the intrinsic Stokes vector of the source, \mathbf{S}_{src} , to our measured \mathbf{S}_{meas} . The inverse total Mueller matrix can then be applied to the measured signal - with a perfect Mueller matrix this would completely recover the intrinsic Stokes

parameters of the source.

$$\begin{aligned}\mathbf{S}_{meas} &= \mathcal{M}_{TOT} \mathbf{S}_{src} \\ \mathbf{S}_{calibrated} &= \mathcal{M}_{TOT}^{-1} \mathbf{S}_{meas}\end{aligned}$$

As matrix multiplication is not commutative, when forming the total Mueller matrix, the order of the individual matrices is important. If the signal undergoes process A followed by process B the total Mueller matrix will be

$$\mathbf{S}_{meas} = \mathcal{M}_B \mathcal{M}_A \mathbf{S}_{src}$$

The first factor encountered by the signal is the rotation of telescope with respect to the source. In an equatorially mounted telescope where one of the telescope axes is aligned with the Earth's spin axis, the telescope beam rotates with the source as it arcs across the sky. Consider a source giving off a constant, 100% linearly polarized signal with a constant polarization position angle. If that polarization was aligned with one of an equatorially mounted telescope's feeds at the beginning of the observation, it will remain that way as the telescope tracks it across the sky. For an alt-azimuthally mounted telescope (such as the Green Bank Observatory's Robert C. Byrd Green Bank Telescope (GBT)) the beam does not rotate with the source and will measure a rotating polarization position angle as the Earth rotates and our fictional source traces out its arc. If an alt-az telescope at a latitude of L , is pointing at source with an hour angle of HA and a declination of δ its axes are rotating with respect to the sky by the parallactic angle given by [2]:

$$\Psi_{altaz} = \tan^{-1} \left(\frac{\sin HA \cos L}{\sin L \cos \delta - \cos L \sin \delta \cos HA} \right) \quad (1.5)$$

This rotation can be represented by the Mueller matrix

$$\mathcal{M}_{sky} = \begin{pmatrix} 1 & 0 & 0 & 0 \\ 0 & \cos 2\Psi_{altaz} & \sin 2\Psi_{altaz} & 0 \\ 0 & -\sin 2\Psi_{altaz} & \cos 2\Psi_{altaz} & 0 \\ 0 & 0 & 0 & 1 \end{pmatrix} \quad (1.6)$$

Knowing the position of the

Secondly, the signal arrives at the telescope and there is the response of the receivers themselves. The two feeds could be perfectly orthogonal and preserve the total power of the signal, but still alter the polarization. Then there are effects from any imperfections in the receivers - for example, if the feeds are not quite orthogonal. The form of the Mueller matrix describing the receiver response, \mathcal{M}_{rcvr} , will depend on the geometry and configuration of the feeds, however its elements typically can be described by just four parameters which quantify the orientations and ellipticities of the two receivers.

Thirdly, no matter how much care is taken to put the two polarizations through identical signal paths, processing, amplifier chains, etc, some differences are inevitable - e.g., even a small discrepancy in cable lengths between the two polarizations will introduce a phase difference between them which is linear with frequency. This effect can be expressed as

$$\mathcal{M}_{path} = \begin{pmatrix} 1 & \gamma/2 & 0 & 0 \\ \gamma/2 & 1 & 0 & 0 \\ 0 & 0 & \cos \phi & -\sin \phi \\ 0 & 0 & \sin \phi & \cos \phi \end{pmatrix} \quad (1.7)$$

where γ is the differential gain between the two feeds and ϕ is the differential phase Heiles et al. [67].

The total Mueller matrix will then be given by

$$\mathcal{M}_{TOT} = \mathcal{M}_{path} \mathcal{M}_{rcvr} \mathcal{M}_{sky} \quad (1.8)$$

Knowing the geographic position of the telescope, the coordinates of the source, and the time over the course of the observation, \mathcal{M}_{sky} can be calculated. The other two matrices must be fit for with the help of calibrator files. This fitting is typically done by decomposing the matrices into 7 independent parameters Heiles [59].

The Cal and Fluxcal

In order to perform the calibration a reference of some kind is required. This is the function of calcs and fluxcals (the latter also known as continuum calcs). To generate these files a noise diode injects a signal at the receiver, typically with a square wave 50% off/on duty cycle. This represents a 100% linearly polarized reference source. These cal scans should be performed with the same observational configuration (number of channels, central frequency, number of phase bins, etc) as the observation to be calibrated.

For pulsars, the cal scan can be performed while pointing at the source, this means that cal mirrors the observational setup for the observation itself as closely as possible. This is possible because most pulsars are weakly emitting and their signals are much smaller than the amplitude of the cal. The cal can be used to calibrate out the effects of the receiver and signal path but with this artificially injected signal it is unclear what absolute flux or power its amplitude would correspond to. This is where the fluxcal comes in.

A fluxcal is comprised of two scans, both with the noise diode and the same observational setup as the pulsar observation as described for the cal scan. An “on” scan is taken while the telescope is pointing at a reference source and an “off” scan is taken pointing at least one beam width away from the reference source. These reference sources are objects for which the flux is well known and measured, often a quasar, e.g., B1442+101. Comparing the height of the noise diode square wave both on and off source¹⁴ lets us recover the absolute flux of the source when calibrating.

1.5 This Thesis

In this thesis we present an analysis of radio observations of PSR J2256-1024, a canonical Black Widow pulsar which also shows radio eclipses. PSR J2256-1024 was discovered using the GBT in the GBT 350-MHz Drift-Scan Survey [68], is coincident with a gamma-ray point source detected by Fermi Gamma-ray Space

¹⁴see <http://psrchive.sourceforge.net/appendices/fluxcal/fluxcal.pdf> for details

Telescope (FERMI) [69], and has since been confirmed as a gamma ray pulsar [70]. In addition, PSR J2256-1024's companion star was optically detected in 2013 [1].

Chapter 2 lays out data acquisition, pre-processing, and the generation of TOAs. Chapter 3 discusses particulars of how the pulsar timing of PSR J2256-1024 was performed. In Chapter 4 results of the timing procedure are presented and discussed, along with the effect of the eclipse and polarization profiles of PSR J2256-1024. Finally, concluding remarks and possibilities for the future are given in Chapter 5.

Chapter 2

Data and Processing

The GBT underwent a major track refurbishment from 30th April 2007 to 3rd September 2007 to replace the entire azimuth track. During this time it was unable to point at and track objects as it would during normal operation. Pulsar searches are large undertakings, requiring sizeable amounts of telescope time on sensitive instruments, and this refurbishment provided a perfect opportunity to gather data. 1191 hours of *drift scan* data were collected, a drift scan being where the telescope is stationary and the sky passes through the telescope beam as the Earth rotates. The survey yielded 35 new pulsar discoveries including PSR J2256-1024.

Pulsars in general are weakly emitting objects and so require telescopes with a large collecting area, like the GBT's 100 m parabolic dish, to be detected and measured. Subsequent radio observations used in this analysis were all performed with the GBT, however observations were taken as a part of multiple projects with multiple observers. As a result, while all taken using standard "timing mode", the data have varying configurations, for instance the central observing frequency, number of channels the frequency bandwidth was split into etc all vary. These different observing configurations are summarized in Table 2.1.

Data was taken using three receivers at the GBT. Two receivers were located at the prime focus and cover frequency ranges 290 MHz–395 MHz and 680 MHz–920 MHz. The third is the Gregorian "L-band" receiver operating at 1150 MHz–

1750 MHz [71]. The majority of the data were taken using the Green Bank Ultimate Pulsar Processing Instrument (GUPPI) backend. During three epochs at MJDs 55 181, 55 191 and 55 226 long observations were taken to cover the entire binary orbit of PSR J2256-1024 using Green Bank Astronomical Signal Processor (GASP) and GUPPI concurrently.

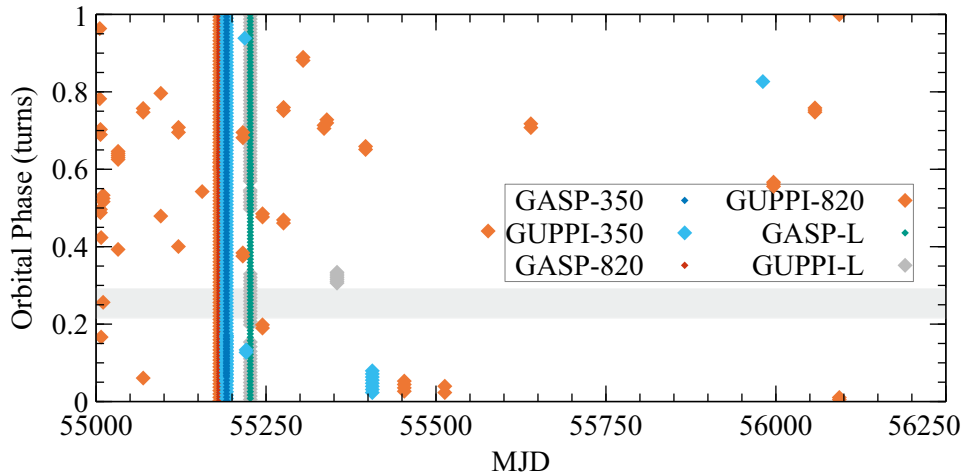
Backend Instrument	Central Frequency MHz	Bandwidth MHz	Number of Frequency Channels	Number of Phase Bins	Full Stokes	MJD Epochs
GASP	352.0	24.0	6	2048	Yes	55191 ⁺
GASP	822.0	64.0	16	2048	Yes	55181
GASP	1392.0	84.0	21	2048	Yes	55226
GUPPI	350.0	100.0	2048	256	No	55406 ⁺
GUPPI	350.0	100.0	2048	512	Yes	55191
GUPPI	350.0	100.0	4096	256	No	55980 ⁺
GUPPI	350.0	100.0	4096	512	No	55218 ⁺ ;55220 ⁺
GUPPI	820.0	200.0	2048	128	No	55215 ⁺ ;55244 ⁺
GUPPI	820.0	200.0	2048	128	Yes	54960 [*]
GUPPI	820.0	200.0	2048	256	No	55005 ⁺ ;55007 ⁺ ;55010 ⁺ ;55032 ⁺ ;55095 ⁺ ;55156 ⁺ ;55275 ⁺ ;55304 ⁺ ;55396 ⁺
GUPPI	820.0	200.0	2048	256	Yes	55006 ⁺ ;55069 ⁺ ;55121, 55335, 55453, 55512, 55576, 55639 ⁺ ;55996, 56057, 56093
GUPPI	820.0	200.0	2048	512	Yes	55181, 55339
GUPPI	1400.0	800.0	2048	256	Yes	55354 ⁺
GUPPI	1500.0	800.0	1024	512	Yes	55226
GUPPI	1500.0	800.0	2048	128	Yes	54897 ^{*+}

* GUPPI data taken before MJD 54999 was excluded from the analysis due to a known error in the field programmable gate array (FPGA) code which was corrected on this date.

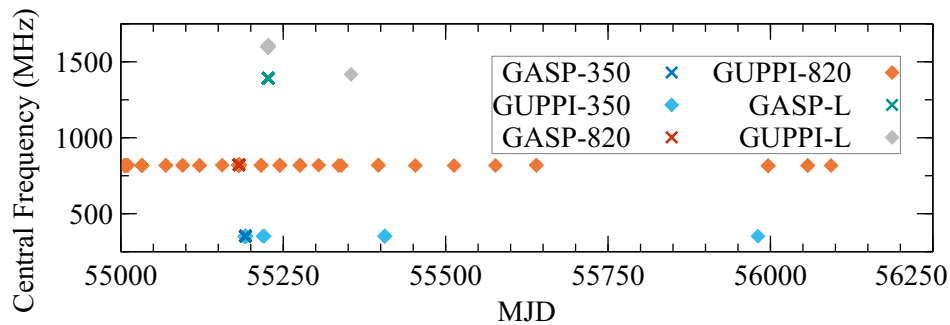
+ These observations were unable to be calibrated due to lack of cal and/or fluxcal data

Table 2.1: Different configurations used to take data. All observations were taken using standard “timing” mode. All GASP data were taken using coherent dedispersion; all GUPPI data were taken in filterbank mode. Full Stokes refers to full polarization data being taken as opposed to just total intensity data.

Figure 2.1 showcases the data coverage with regards to orbital phase and frequency. GUPPI data before MJD 54999 have been excluded. It is worth noting the frequency coverage of the data - the majority of observations were taken at 820 MHz and epochs with multi-frequency observations are rare.



(a) Orbital Phase coverage of observations, including TOAs in and near the eclipse region. The grey band shows the approximate location of the eclipse (Section 4.2) including exit and entering regions



(b) Frequency coverage of observations

Figure 2.1: Orbital Phase and Central Frequency of the final residuals are plotted against MJD, showing the data span and coverage. GASP markers differ from the GUPPI ones solely for clarity in the three epochs where scans were taken simultaneously with the two backends

2.1 GASP and GUPPI

For pulsar timing Green Bank Astronomical Signal Processor (GASP) [72, 73] was the previous backend used at the GBT. It featured a maximum bandwidth of 128 MHz, the ability to record full Stokes information, coherent dedispersion (implemented via software), and 8-bit sampling to reduce quantization distortion¹.

The Green Bank Ultimate Pulsar Processing Instrument (GUPPI) [74, 75] is the current backend used for (almost) all pulsar observations at the GBT. Previously there were many pulsar backends at the GBT, each specialised for a different purpose, e.g., GASP was principally used for timing observations, Green Bank Telescope Pulsar Spigot (SPIGOT) [76] was more suitable for pulsar searches and as a spectrometer. The thesis behind GUPPI was to replace many pulsar backends with just one, combining (and preferably improving on) the best of those systems whilst have enough flexibility that it was suitable for a range of observing styles. For example, some settings available to the user were the bandwidth, number of frequency channels, integration time, and whether the data were coherently dedispersed or filterbank. This flexibility was key in allowing GUPPI to satisfy so many different observing needs.

Both GUPPI and GASP could take timing data with full Stokes polarization information and have a high dynamic range with 8-bit sampling. GUPPI is an improvement over GASP with its wider bandwidth of up to 800 MHz.

GUPPI was implemented in two phases. “Phase I” saw first light 17th April 2008. Phase II, which included coherent dedispersion mode, was implemented December 2009 which happens within the data span². Despite the availability of coherent dedispersion after December 2009 observations were still taken using the filterbank system.

¹which produces a non-linear relationship between the analogue signal and the digital output, and a lowered signal to noise ratio (SNR)

²31st December 2009 being MJD 55196

2.2 PSRCHIVE

PSRCHIVE [77] is large software suite with programs designed to manipulate and analyse pulsar data. Its capabilities go above and beyond what will be mentioned here but PSRCHIVE’s part in the flow from ”pulsar emits pulses” to ”a timing solution with residuals” is to get from the data recorded by the backend to TOAs. It has programs to produce plots and examine data (`pav`, `psrplot`), to perform calibration (`pac`, `fluxcal`, `pcm`), to excise or zero-weight certain parts of an observation (`paz`, `pazi`), to perform the frequency- and time-scrunching mentioned in Subsection 1.3.1, and much more. For documentation on how PSRCHIVE can be used in pulsar analysis van Straten et al. [78] is an excellent resource as is the PSRCHIVE homepage [79]. PSRCHIVE was used extensively for this analysis and of its any programs used are typeset as `program`.

2.3 Radio Frequency Interference Excision

Pulsars are not the only objects giving off radio signals and as mentioned in the beginning of this chapter pulsars are relatively weakly emitting. Often observations also detect these other signals or radio frequency interference (RFI); they drown out the pulsar signal and must be removed. Most RFI is due to objects manufactured by humans. There are intentional signals such as satellites, radio transmitters, etc. There is also incidental radio emission from human-made objects, for example only diesel vehicles are permitted in the immediate area surrounding the GBT because spark plugs give off wide-band radiation, including radio, which is detected by the GBT. There was also an incident at Parkes Observatory where an intriguing transient radio signal was discovered to be due to a microwave [80].

Zero-weighting or *zapping* frequency channels and/or sub-integrations due to the presence of radio frequency interference (RFI) is standard procedure in pulsar timing and was done using PSRCHIVE’s `paz` program. As all observations were taken with the GBT at its enviable position within the United States National Radio Quiet Zone (NRQZ) occurrences of RFI were relatively low and minimal zapping was necessary.

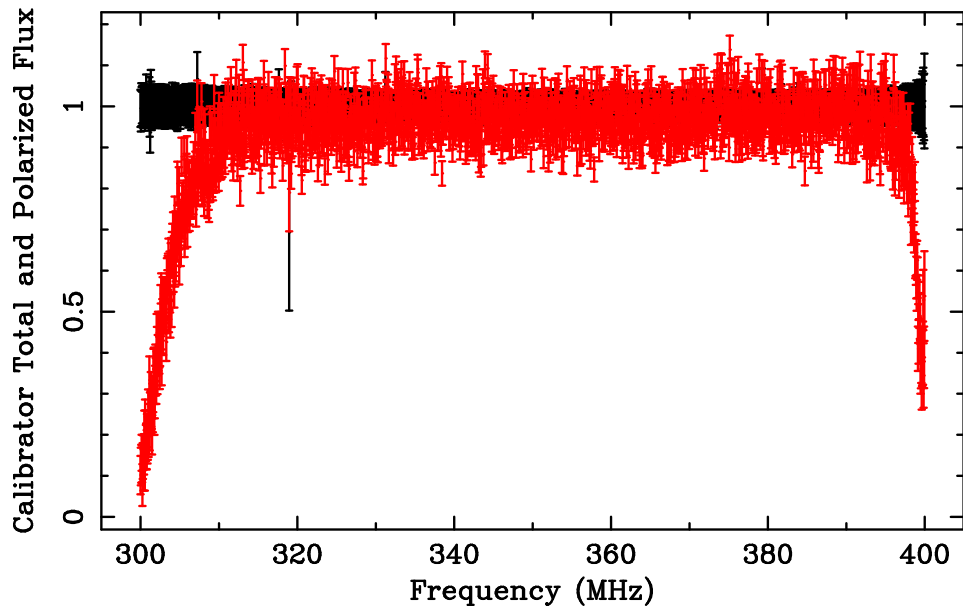


Figure 2.2: An example `pacv` plot of a calibrator file applied to itself, demonstrating depolarization near the edges of the frequency band. The calibration has been applied such that the calibrator has a total flux of 1. Total flux is shown in black, polarized flux is shown in red

The edges of the frequency band are known to be affected by quantization distortions and data therefore corrupted in these regions [78]. For GUPPI observations how much of the band edge to zero-weight was determined by looking at distortion in the cal files. `pacv` was used to plot the height of the cal's square wave vs frequency, for the total and polarized flux, when the calibrator file had been applied to itself. The cal signal is injected and by nature should be perfectly polarized; any drop off in the polarized flux is evidence of depolarization occurring due to instrumental effects. An example of one such plot is shown in Figure 2.2 and the degradation near the band edges is clear. As can be seen in Figure 2.2 these distortions affect band edges asymmetrically; the zapped regions at the band edges corresponded to $\approx 5\%$ of the total bandwidth at the upper edge and $\approx 10\%$ at the lower edge.

For GASP observations no band-edge zapping was performed. Due to the

smaller total bandwidth and the higher bandwidth per frequency channel, this effect can be neglected in GASP observations.

Other zapping in the frequency domain was done by eye and by use of the `paz` median smoothed difference algorithm.

This algorithm takes a subset of the frequency band (a window) and compares data in that window to a median smoothed version of itself³. This window should therefore be larger than the bandwidth of any expected RFI so that the RFI does not dominate the window. For the GUPPI filterbank data where the band has been split into a higher number of channels (typically 2048, see Table 2.1) a median smoothing window of 100 channels was used. For observations with very low signal to noise ratio (SNR) this procedure is naturally less effective and can erroneously target the pulsar signal, lowering the SNR. Therefore, for very short observations if median smoothed zapping lowered the SNR it was not performed.

Zapping by eye was done by observing `pav` plots of frequency vs pulse phase, and zapping when a frequency channel or band of channels was obviously affected.

Sometimes RFI is present due to a transient signal over a wide frequency range but only for a short amount of time, just affecting a few sub-integrations. These cases were detected by eye based on `pav` plots and interactive zapping using the `pazi` program. The appropriate sub-integrations were zapped with `paz`.

This was done for pulsar observation files, cal files and fluxcal files⁴ as, for each frequency channel, accurate measurements are needed from all three files for that channel to be present in the resulting calibrated pulsar observation.

2.4 Polarization Calibration

Where cal and fluxcal files were available, observations were polarization calibrated using `pac -x`. `pac` is PSRCHIVE’s polarization calibration program and the `-x` specifies that the “Single Axis” model was used, with Stokes parameters being derived from the fluxcal (when a fluxcal was available). The Single Axis

³for more details refer to the PSRCHIVE documentation [79]

⁴if being used

model assumes that the two polarization receivers are perfectly orthogonal; combining this model with information derived from the fluxcal allows for differences in how the two receivers are illuminated by the source. Under these assumptions the 7 parameters which can be used to model the instrumental response mentioned in Subsection 1.4.3 have been reduced to three: the absolute gain, G , the differential gain, γ , and the differential phase, ϕ . These three parameters are calculated for each frequency channel using the cal file according to⁵:

$$\begin{aligned}\tan 2\phi &= \frac{UV' - VU'}{UU' + VV'} \\ \tan 2\gamma &= \frac{IQ' - QI'}{II' - QQ'} \\ G^2 &= \frac{I^2 - Q^2}{I'^2 - Q'^2}\end{aligned}$$

where $[I, Q, U, V]$ are the known or input Stokes parameters coming from the fluxcal (if available) and $[I', Q', U', V']$ are the observed Stokes parameters in the cal file.

Figure 2.3 shows an example calibrator solution with the calculated G , γ , and ϕ for each frequency channel.

2.5 Rotation Measure Corrections

For details on how the rotation measure (RM) was determined see Section 4.4.. In that section it is noted that (i) RM was measured and corrected for using the `rmfit` program within PSRCHIVE, (ii) RMs were found using GUPPI observations at three epochs (MJDs 55181, 55191 and 55226) with frequencies of 820 MHz, 350 MHz and 1500 MHz respectively, and (iii) three values of RM were found which agree at just under 3 sigma.

For timing purposes only the full intensity profile was used to generate TOAs and therefore these corrections have no effect. For clarity and reproducibility we

⁵assumes a linear basis

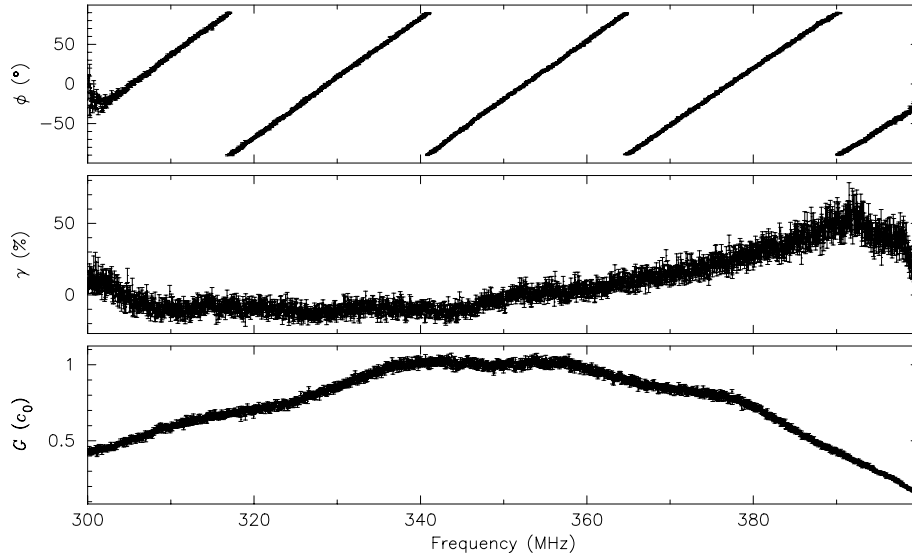


Figure 2.3: An example calibrator solution, derived from a cal file taken on MJD 55 191, pointing at PSR J2256-1024

report the following: all observations for which it was possible (i.e., which had full Stokes data) were corrected for Faraday rotation using a RM of 14.93 rad/m^2 , the value found using the GUPPI 350 MHz observation, as this gave the strictest condition on the RM value.

For generating the polarization profiles shown in Section 4.5, each observation was corrected for Faraday rotation using the specific RM measured using that observation - i.e., the $RM_{\text{rfit-iterative}}$ values of Table 4.6.

2.6 TOA Generation

By this point files have had any RFI excluded, have been polarization calibrated assuming an ideal feed (where possible) and corrected for Faraday rotation (again where possible).

2.6.1 Generating Standard Profiles

Due to the different configurations data were taken in (see Table 2.1) some extra processing went into the generation of standard profiles. A different standard profile was created for each observational frequency and backend combination, and separate standard profiles were created for coherently dedispersed and filterbank data.

It was not possible to perform flux and polarization calibration for all of the data. In instances where there is a combination of calibrated and uncalibrated data taken in one mode, only the calibrated files were used to generate the standard profile. Additionally only those with full Stokes data were able to be corrected for Faraday rotation, so in those instances only RM corrected observations were used to generate the standard profile. This procedure has been included for clarity and reproducibility but it should also be noted that these corrections do not matter for the standard timing procedure.

Data going into the same standard profile (and the observations to which it was going to be applied) all needed to match in number of phase bins (`nbin`) and number of frequency channels (`nchan`). To make the number of phase bins match this just meant binning to the lowest `nbin` of the data subset using `pam`. Altering the number of frequency channels was only necessary in a few cases and for all of these the data were taken in filterbank mode.

In order to make an equivalent-looking observation with fewer channels it was necessary to add channels together (`fscrunching`) without dedispersing them. While dedispersing the channels and adding them would lead to narrower, less smeared profiles, this would be different from an observation which had been initially recorded with fewer channels. To do this the DM was uninstalled by setting it to 0, the channels were `fscrunched` together by the appropriate factor (using `pam`), and the DM was then reinstalled afterwards.

Once this had all been done, to generate a standard profile, observations were frequency `scrunched` down to one channel and sub-integrations containing or near

the eclipse were excluded⁶. Then observations were added together and time scrunched to one sub-integration after each new addition using `psradd`. They were then smoothed using `psrsmooth` to reduce the effect of noise. When comparing a standard profile with an observation that also went into generating it, then there will be some noise in the standard profile that is the same as in the observation being compared. This can affect the cross correlation used to generate TOAs [81]. This is often the case and so smoothing the standard template is necessary to reduce those effects. The smoothing algorithm used was the default which is translation-invariant and uses 8 orders of the Daubechies wavelet family [82]. The data is transformed into the wavelet domain. Here the noise is measured and used to set a threshold below which wavelet coefficients are set to zero. The data is then transformed back to produce a smoothed profile.

The profiles were then aligned, using the GASP 820 MHz profile as a reference, using `pas`.

2.6.2 Generating TOAs

Observations were frequency scrunched to one channel. In order to maximise the SNR of each individual profile used to make a TOA, observations were also scrunched in time. However to get a good timing solution, a decent level of time-resolution needs to be preserved - as an extreme example, if an observation spans one entire period of the binary system, scrunching it down to one sub-integration and making one TOA from that removes a lot of useful information about the binary system. Keeping this in mind, observations were time scrunched such that a) $n_{subint_{old}}$ was a multiple of $n_{subint_{new}}$ and b) so that the duration of the new sub-integration was based on a starting point of 184 s, a minimum value of 60 s and a maximum of 368 s (corresponding to approximately 1 %, 0.33 % and 2 % of the binary period respectively). This gave a compromise between the need for high SNR and the need for good binary period coverage.

The TOAs were then generated using `pat`, PSRCHIVE’s TOA generation program. `pat` determines the phase shift between a pulse profile and the standard by

⁶along with any containing the “blip” discussed in Section 4.3

computing the cross-correlation between the two profiles in the Fourier domain. There are several methods for this available in `pat`; the standard algorithm - the “Fourier Phase Gradient” described by Taylor [55] - which compares the total intensity between the profiles was used for this analysis. One TOA was generated per sub-integration from the tscrunch files described in the previous paragraph.

Even when observing the same pulsar, signal paths through GUPPI vary depending on the mode and configuration data were taken in. This results in known delays which were calculated with the `guppi_offsets` tool for each observational configuration. These time shifts were then added to the files containing the TOAs.

Once a good timing solution and a stable `par` file was arrived at, observations were re-folded with the new `par` file. New standards profiles and TOAs were then regenerated as per the system described above.

Chapter 3

Timing

3.1 TEMPO and TEMPO2

In Subsection 1.3.1 the idea behind pulsar timing was covered - computing predicted TOAs from a model, then comparing these to the measured TOAs to fit for an improved model. The TEMPO software package [83] and its descendant TEMPO2 [84] are the programs which perform this heavy lifting (and much more besides).

In addition to computing the new model, being able to account for a wide range of effects, and producing residuals, TEMPO must first process the TOAs. One TOA contains little information; being able to compare it and combine it with other TOAs is the basis of pulsar timing. But comparing a TOA which arrived at the UK in December to one which arrived at Puerto Rico in March takes some work; they arrived at different clocks, at different times, in different time-zones, at different locations on the Earth, which was rotating, when the Earth itself was in different locations moving with differing spins and velocities, etc. Therefore we transform TOAs to when they would arrive at the Solar-System Barycenter (SSB)¹. TEMPO performs these transforms and corrections, more details are given in Sections 3.2 and 3.3.

¹Ideally an inertial reference frame would be used, but the SSB is the best feasible frame

3.2 Assumptions and Model Parameters

Assumptions and Model Parameters		
POSEPOCH	Epoch of position measurement (MJD)	55549.0000
PEPOCH	Epoch of period determination (MJD)	55549.000000
EPHEM	Solar system ephemeris used	DE436
CLK	Clock correction used	TT(BIPM)
UNITS	Relativistic coordinate time scale	TDB
TIMEEPH	Time ephemeris used	FB90
T2CMETHOD	Method for transforming from terrestrial to celestial frame	TEMPO
CORRECT_	Whether tropospheric delay corrections were applied	N
TROPOSPHERE		
PLANET_	Whether calculation of the planetary Shapiro delays were included	N
SHAPIRO		
DILATEFREQ	Whether gravitational redshift and time dilation was applied to observing frequency	N
SOLARN0	Proportionality constant for solar wind model (electrons cm ⁻³ at 1 AU)	5.00
BINARY	Binary model used	BTX
Data Statistics		
START	Start of data span (MJD)	55005.385
FINISH	End of data span (MJD)	56093.266
NTOA	Number of TOAs	773
TRES	RMS timing residual (μ s)	0.99

Table 3.1: Assumptions, model parameters used in the fitting procedure to obtain the values in Table 4.1 and statistics on the input data

3.2.1 Clock Correction and Time Systems

The pulses were originally measured at the GBT using a hydrogen maser clock² - this would give the local topocentric time. This is then transformed to Coordinated Universal Time (UTC) with the help of Global Positioning System (GPS). The TOAs are then converted into Terrestrial Time (TT). This is a coordinate timescale based on atomic clocks, taking into account relativistic effects and defined so that

²these clocks themselves have the high timing resolution pulsar observing requires but are not stable over long timescales and have their own set of clock corrections applied

its second would match an SI second on the surface of the Earth³. The version of TT used is that published by the Bureau International des Poids et Mesures (BIPM) which re-analyses data and retrospectively corrects for errors, publishing a new version of TT(BIPM) approximately every year. There is then a final transformation to Barycentric Dynamical Time (TDB), a coordinate timescale which accounts for time dilation due to the combination of the orbital speed of an observer in the gravitational potential of the Sun and planets.

3.2.2 Projecting onto the Solar-System Barycenter (SSB)

When transforming to TDB shifts are added to project the TOAs onto the SSB. These include the *Römer delay*, the *Shapiro delay* and the *Einstein delay*; their expressions below are as per Lorimer and Kramer [2].

The Römer delay stems from the time it takes light to travel through the solar system. It is expressed as:

$$\Delta_{R_{\odot}} = -\frac{1}{c} (\vec{r}_{SSB} + \vec{r}_{EO}) \cdot \hat{s}$$

where \hat{s} is a unit vector pointing from the SSB to the pulsar, \vec{r}_{SSB} is the vector from the SSB to the centre of the Earth, and \vec{r}_{EO} connects the geocentre to the telescope.

However space-time in the solar system is not flat, it's curved due to the presence of the Sun and other massive bodies. This is accounted for with the Shapiro delay. The main contributions are due to the Sun and Jupiter but the complete form of the expression sums over all solar system bodies:

$$\Delta_{S_{\odot}} = -2 \sum_i \frac{GM_i}{c^3} \ln \left[\frac{\hat{s} \cdot \vec{r}_i^E + r_i^E}{\hat{s} \cdot \vec{r}_i^P + r_i^P} \right]$$

where M_i is the mass of body i , \vec{r}_i^P is the position of the pulsar relative to that body and \vec{r}_i^E is the position of telescope relative to it.

The Einstein delay then corrects for gravitational redshift due to the gravita-

³or rather on the surface of the geoid

tional potential of massive bodies in the solar system and also time dilation due to the motion of the Earth. It can be expressed as:

$$\frac{d\Delta_{E\odot}}{dt} = \sum_i \frac{GM_i}{c^2 r_i^E} + \frac{v_E^2}{2c^2} - \text{constant}$$

where r_i^E is the distance between body i and the Earth, v_E is the velocity of the Earth relative to the Sun, and the sum is over all solar system bodies except for the Earth.

For all three of these corrections accurate positions and movements of the bodies in the solar system is necessary. For this the NASA Jet Propulsion Laboratory (JPL) planetary and lunar ephemeris DE436 was used. The TOAs are also corrected for the frequency-dependent dispersion(as per Subsection 1.2.1) due to the material between the SSB and the Earth.

Of course these factors will also be present in the binary system of the pulsar. With long term timing, a suitable pulsar, and a suitable system, all three can be fit for and measured. With PSR J2256-1024 the binary's Romer delay is accounted for but the Einstein and Shapiro delays are not⁴.

3.2.3 Binary Model

The BTX model⁵ was used to model the orbit of the pulsar. This is based on the BT model [85], but uses the binary orbital frequency and its derivatives as opposed to the binary orbital period. Implemented in the BTX model was also the ability to add instantaneous jumps in the binary orbital frequency and allowing for multiple derivatives in the orbital size, but these features were not necessary in this analysis.

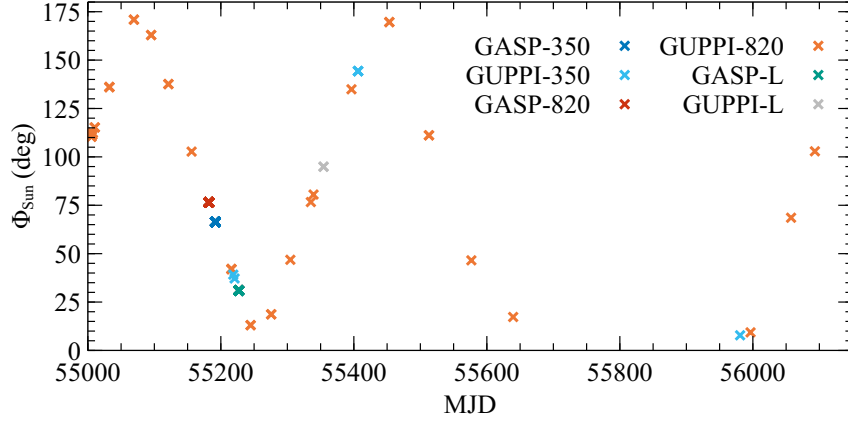


Figure 3.1: Φ_{Sun} and Timing Residuals vs MJD

3.2.4 Dispersion Effects from the Sun

We expect the DM to vary due to fluctuations in the ISM and the changing line of sight to the pulsar. There will also be a dispersive effect from the Sun, most pronounced when the Sun is close to the line of sight to the pulsar [86–88]. Due to PSR J2256-1024’s position in the sky, it spends the majority of its time far from the Sun. However, as can be seen from Figure 3.1, there are some epochs where the angular distance between the two is much smaller; therefore this effect cannot be neglected. Within TEMPO this effect can be modelled with a “toy model” which assumes this wind is constant and spherically symmetric, where the electron density following a $1/r^2$ law with distance from the Sun. In TEMPO this is described by SOLARN0, the electron density at 1 AU.

In the literature a range of values from $0 \text{ e}^{-\text{cm}^{-3}}$ to $10 \text{ e}^{-\text{cm}^{-3}}$ are used for SOLARN0. A range of integer values for SOLARN0 were tried; residual statistics were most improved by using $5 \text{ e}^{-\text{cm}^{-3}}$. With no clear standard procedure in the literature, and fitting for variations in DM not being possible (Subsection 3.5.5), this was the value used in the final timing solution.

⁴Even with a longer data span with better frequency coverage, the small companion mass would make these delays difficult to detect

⁵D. Nice, unpublished

3.3 Error handling - EFAC, EQUAD and Reduced Chi Squared

The chi squared statistic is given by Equation (3.1) and one way of measuring how “good” a model fits the data. TEMPO used this with a least-squares fitting procedure, to find the fit which minimises the reduced chi squared. The chi squared statistic takes the form:

$$\chi^2 = \sum_{i=1}^N \left(\frac{x_i - \mu}{\sigma_i} \right)^2 \quad (3.1)$$

where the data is in the form $x_i \pm \sigma_i$ and μ is the prediction from the model. It assumes the data points (in the case of pulsar timing, the residuals) are uncorrelated⁶ and that their errors are Gaussian. The reduced chi squared is simply the chi squared statistic divided by the number of degrees of freedom (the number of data points minus the number of free parameters in the model). For a perfect model one would expect $\chi^2 \approx n$, where n is the number of degrees of freedom.

Ideally the fit output by TEMPO would give in a reduced chi squared of approximately 1. A $\chi_{red}^2 \ll 1$ is often a symptom of either over-fitting or over-estimation of the data’s uncertainties. A $\chi_{red}^2 \gg 1$ can be a result of a “bad” fit or an under-estimation of uncertainties in the data.

The uncertainty attached to each TOA is output by `pat` and results from cross-correlating the pulse with the standard profile. However it is commonly accepted that there will be some systematic errors in the TOAs due to factors such as *pulse phase jitter* [90, 91], instrumental effects, insufficient calibration or calibration errors [92], a badly chosen standard profile, *timing noise* [93, 94], etc, which these uncertainties do not account for.

If a reduced chi squared larger than 1 and there is a reasonable belief that this is due to undervaluing of TOA errors. In this scenario commonly the uncertainties are manipulated to increase the errors and reduce the reduced chi squared. This is done through parameters such as EFAC which scales TOA uncertainties by the given

⁶TEMPO does have a generalised least-squares fitting procedure [89] which does not make this assumption but for timing at the level needed for PSR J2256-1024 this made no difference to the resulting model parameters or reduced chi squared.

factor, or EQUAD which adds the given value in quadrature to TOA uncertainties. These can be applied to all TOA uncertainties or only a given subset e.g., specific receiver and backend combinations.

Looking at the residuals for PSR J2256-1024 there is some scatter and some residuals which look like outliers but have no reason, such as obviously corrupt profiles, to be excluded - a $\chi_{red}^2 > 1$ is therefore expected. There is also no reason to suspect that uncertainties from a particular instrumental configuration have been undervalued. Therefore no error-raising parameters were used. For the whole data set $\chi_{red}^2 = 1.41$, this means that the uncertainties associated with the best-fit parameters output by TEMPO are likely slightly undervalued. The parameter uncertainties have not been processed - all appearing in tables and quoted in text are the values directly output by TEMPO. Quantities derived from TEMPO fit parameters uncertainties have been propagated using the correlation matrix (also output by TEMPO) also using these directly output uncertainties.

3.4 Data Excluded from the Fit

Some observations were excluded altogether - they were not included in the fitting procedures and no residuals were generated from them. This was done if the data had been compromised in some way, e.g., as already said in Table 2.1 GUPPI data taken before MJD 54999 was subject to a known error in the FPGA code which resulted in unpredictable timing offsets. Other reasons include a very low signal to noise ratio, so much so that the pulsar was undetectable, and one occasion where the entire observation fell during the eclipse. There was also one observation performed at 2000 MHz but the pulsar was very weak at this frequency and the SNR for this observation was too low to make a standard profile.

Some observations were only excluded from the fitting procedure but residuals were still generated - so they had no effect on the generation of new fit parameters but those new fit parameters were applied to them and those residuals appear in some plots. This was the case for any TOAs that fell during the eclipse or some buffer region either side where the pulses would be delayed by the eclipsing material. At certain MJDs a “blip” of delayed TOAs, discussed in Section 4.3, is present

just after the eclipse and these TOAs were also omitted from the fit.

Unless explicitly stated otherwise e.g., for plots of the blip in Section 4.3, the residuals discussed above are excluded from plots. Otherwise plot scales would be dominated by the eclipse during which the residuals become large and random as no pulses are detected.

3.5 Parameters Which Could not be Successfully Fit

Version of Parameter File	χ_{red}^2	t_{WRMS} μs	η
Final Timing Solution	1.41	0.994	
Including E	1.41	0.992	$\eta_E = 1.65916$
Including XDOT	1.41	0.994	$\eta_{XDOT} = 0.60866$
Including PMRA and PMDEC	1.40	0.989	$\eta_{PMRA} = 2.57661$ $\eta_{PMDEC} = 2.67859$
Including just PMRA	1.41	0.993	$\eta_{PMRA} = 0.7706$
Including just PMDEC	1.41	0.993	$\eta_{PMDEC} = 1.05979$
Including F2	1.41	0.993	$\eta_{F2} = 1.05545$
Including FB1	1.40	0.988	$\eta_{FB1} = 2.96744$
Including F2 and FB1	1.39	0.984	$\eta_{F2} = 2.40077$ $\eta_{FB1} = 3.67318$

Table 3.2: Statistics for some parameters excluded from the final timing solution. $\eta = \text{value}/\sqrt{\chi_{red}^2} \times \text{uncertainty}$

There were a number of parameters that were considered but not included in the final fitted parameters for PSR J2256-1024. In order to be included in the final timing solution when including a new parameter: TEMPO should be able converge on a stable solution, the value found for the new parameter should be significant with respect to its uncertainty, there should be an improvement in the weighted root mean square (WRMS) post-fit residual, the reduced chi squared of the fit, and in the post-fit residuals. To consider a parameter significant normally a threshold of three times the uncertainty in the parameter as output by TEMPO would be reasonable. However because the reduced chi squared for the fit is greater than 1 (see Section 3.3) these uncertainties will be undervalued which should be taken into account. To approximate this effect the significance threshold was taken to be

three times the TEMPO uncertainty multiplied by the square root of the reduced chi squared, or $\eta > 3$ where for each parameter $\eta = \frac{\text{value}}{\sqrt{\chi_{red}^2} \times \text{uncertainty}}$. Table 3.2 shows some statistics from the alternate TEMPO fits where additional parameters were included.

In this section when referring to including parameters in the fit etc, all parameters other than jumps were allowed to vary during TEMPO's fitting process, unless explicitly stated otherwise.

3.5.1 Eccentricity

From Table 3.2 it is clear that fitting for the eccentricity, E, does not meet our criteria for inclusion in the fit. In addition any resulting changes to the residuals could not be distinguished by eye. Therefore the eccentricity was held fixed at 0.

Periastron is when the pulsar is at its shortest distance from the centre of mass of the binary system. With the eccentricity of the system fixed at 0 the orbit is perfectly circular the pulsar is always at its shortest distance to the system centre of mass, making the position of periastron somewhat arbitrary. Therefore the longitude of periastron, ω (or OM in TEMPO shorthand), can be set to 0° with a corresponding epoch of periastron (T0).

3.5.2 Rate of Change of Projected Distance from the Pulsar to the Center of Mass

The TEMPO fit includes A1, which is often referred to in pulsar papers as simply the semi-major axis. This is because A1 is intimately tied to the semi-major axis, but is in fact the projected distance between the center of mass (COM) of the pulsar, and the COM of its binary system - A1 corresponds to $a_p \sin i$ in Equation (4.1). Changes in A1 clearly correspond to those in the projected semi-major axis which is why the terms tend to be used interchangeably, particularly when discussing pure Keplerian orbits.

A1 may evolve with time due to several factors, in TEMPO this is allowed for with the parameter \dot{X} . The projection of the system may change due to its

proper motion [95], or changes in the orbit itself, e.g., precession. In addition the semi-major axis could be evolving, e.g., due to mass-loss from the system, energy loss from the emission of gravitational waves, etc. As PSR J2256-1024 is a Black Widow (BW) and therefore known to be losing material, fitting for an \dot{X} value was attempted but (as can be seen from Table 3.2) was not successful.

3.5.3 Proper Motion

Fit Includes	PMRA mas/yr	PMRA mas/yr	Composite Proper Motion mas/yr
PMRA and PMDEC	3.2(11)	-8(3)	9(3)
PMRA	-0.11(12)	-	0.11(12)
PMDEC	-	-0.4(3)	0.4(3)

Table 3.3: Values found for PMRA and PMDEC when included in the fit. All uncertainties given are those directly output by TEMPO

TEMPO allows for fitting the proper motion in the directions of right ascension through PMRA, and declination through PMDEC. Values attained including these parameters in the fit, either separately or together, are given in Table 3.3. From Table 3.2 fitting PMRA and PMDEC together give results which are close to fulfilling the previously stated criteria for inclusion.

However, the data span is quite short -2.978 yr - and not well sampled, as can be seen from Figure 2.1 or any of the residual plots Subsection 4.1.2; most notably there are no observations between MJDs 55639.55980. This would make determining the proper motion difficult. As such, evidence justifying its inclusion should be particularly solid to ensure the value is physically meaningful. This is not the case and so proper motion was not included in the fit

3.5.4 Further spin frequency and orbital frequency derivatives

From Table 3.2, while the next spin frequency derivative, F2, should obviously not be included, FB1 seems like a possible candidate. Including FB1 gave a value of $-2.2(6) \text{ s}^{-2}$, and we do expect to see some orbital evolution in this system since it

is known to be losing mass. However, no change in the residuals was visible and the ability to measure higher frequency derivatives is very dependent on the length of the data span. With a data set this short we determined there was not strong enough evidence to include FB1.

3.5.5 DM Variations

Over the approximately 3 yr data span small variations in the DM are expected due to shifting material in the ISM and variations in the path between Earth and PSR J2256-1024 due to their changing positions. These variations are expected to be on a scale of $10^{-3} \text{ cm}^{-3} \text{ pc}$ [89, 96, 97].

As discussed in Subsection 1.2.1, DM dispersion is a frequency dependent phenomenon; observations at a range of frequencies are necessary for a proper measurement. The DMX functionality in TEMPO splits the data into bins in time and then allows for a different DM value in each bin. For this to be effective there should be data from at least two well-spaced frequencies in each bin, otherwise it becomes less believable that TEMPO is modelling actual changes in the DM rather than merely fitting out other variations. The data span for PSR J2256-1024 does not have good frequency coverage (see Figure 2.1a) and also has some notable gaps in time, both of which made determining DM fluctuations less likely. No robust solution for DM variations could be found, even when splitting observations into several frequency channels (rather than the Fscrunching described in Subsection 2.6.2) to take advantage of GUPPI's large bandwidth. Given that DM variations are certainly occurring, especially in a system that is itself ejecting material, not accounting for this in the model will be one contributing factor to the reduced chi squared [98].

Chapter 4

Results

4.1 Timing Solution

4.1.1 Fit Parameters

Table 4.1 shows the resulting parameters fit by TEMPO. For the assumptions used to obtain this fit and information about the fit assumptions and statistics refer to Tables 3.1 and 3.3. For the full parameter file as output by TEMPO see Table A.1 in Appendix A. The values given in Table 4.1 are those as output by TEMPO; the value shown for the first spin frequency derivative has not been corrected for the effects of galactic acceleration.

Derived parameters, such as the corrected first spin frequency derivative, the mass function of the system, and the characteristic age of the pulsar, are given in Table 4.2

Pulsar Parameters		
TEMPO Shorthand	Description	Value
RAJ	J2000 Right ascension (hh:mm:ss)	22 ^h 56 ^m 56.392734(22) ^s
DECJ	J2000 Declination (dd:mm:ss)	−10°24 ^m 34.3769(8) ^s
F0	Rotational frequency (s ^{−1})	435.8187550969490(19)
F1	1st time derivative of the rotational frequency (s ^{−2})	−2.15604(13) × 10 ^{−15}
DM	Dispersion measure (cm ^{−3} pc)	13.776020(3)
PX*	Parallax (mas)	0.51(14)
Binary Parameters		
A1	Projected semi-major axis of orbit (lt – sec)	0.08296576(5)
E	Eccentricity of orbit	0.000000000
T0	Epoch of periastron (MJD)	55548.92435239(6)
OM	Longitude of periastron (°)	0.000000000000
FB0	Orbital frequency (s ^{−1})	5.4368334585(9) × 10 ^{−5}

* tentative - see discussion in Subsection 4.1.1

Table 4.1: Final fit parameters for PSR J2256-1024. Quantites in parentheses indicate the uncertainties in the last digits. Errors shown are as output by TEMPO - they have not been processed in any way except for rounding. F1 has not been corrected for galactic acceleration

A Note on Parallax

We are presenting the parallax in the final timing solution as a tentative measurement. Strictly PX did not fulfil the criteria in Section 3.5. Its inclusion improved the reduced chi squared by 0.01, the WRMS post-fit residual by 0.006 μ s, and no visible effect on the residuals could be seen. However, unlike parameters such as proper motion and higher frequency derivatives, parallax is a repeating signature rather than a growing effect. Folding the residuals into a timespan of one year, as in Figure 4.1, shows a reasonable coverage of data across the year, making a parallax measurement more feasible. In addition the parallax gives a distance of 1.3(4) kpc to PSR J2256-1024, which is compatible with the value of 2.0(6) kpc derived from the DM in Subsection 4.1.3.

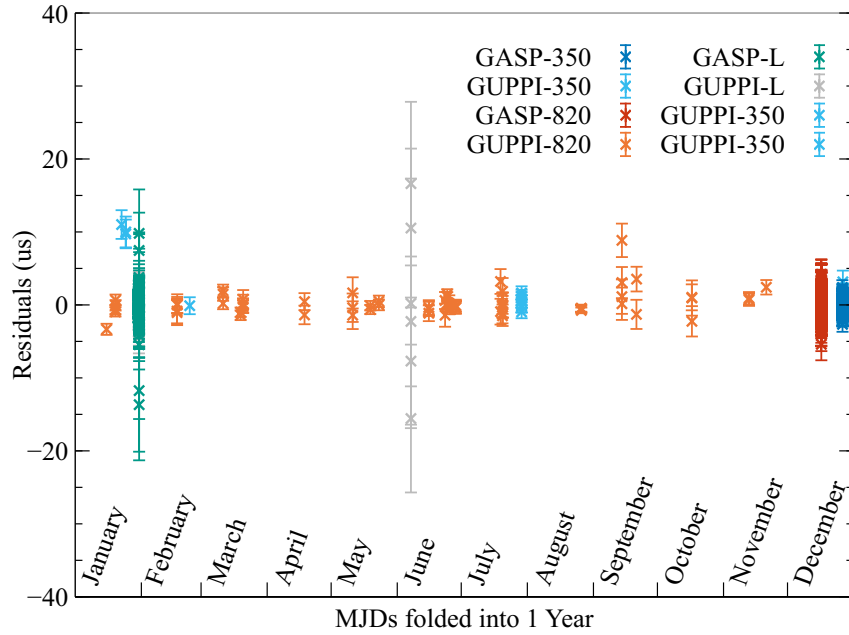


Figure 4.1: Timing Residuals vs MJD, folded into a span of one year to show data coverage for a parallax measurement. The eclipse (plus both ingress and egress) and the blip have been excluded.

4.1.2 Residuals

As mentioned in Section 1.3 the residuals are what is left once the model has been subtracted from the data. Figure 4.2 shows residuals resulting from the final timing solution¹ plotted against MJD, excluding regions where the pulsar was in or near eclipse. Figure 4.3 shows these same residuals plotted against the phase of the binary orbit. TEMPO does not model the eclipse in any way so residuals in that region are large, dominate the scale of plots, and aren't indicative of how well the model fits otherwise. Thus in this section, plots and discussion of the residuals exclude those in the eclipse region (including the blip discussed in Section 4.3). For observations showing a blip the excised range was 0.21 to 0.32 in binary orbital phase, for observations with no blip orbital phases 0.21 to 0.3 was excluded.

¹parameters given in Tables 4.1 and 3.2, or Table A.1 for the full parameter file

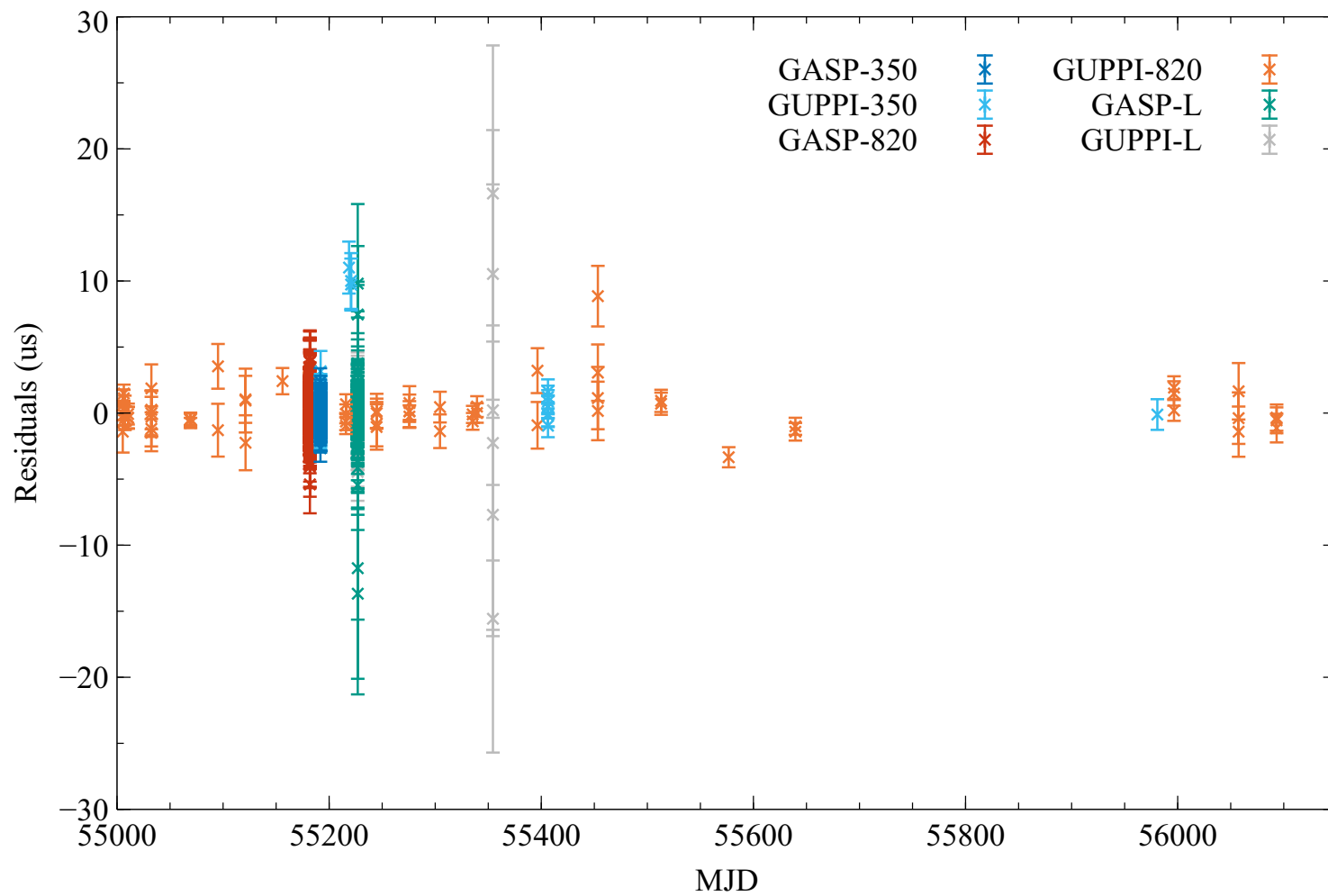


Figure 4.2: Timing Residuals vs MJD. The eclipse (plus both ingress and egress) and the blip have been excluded.

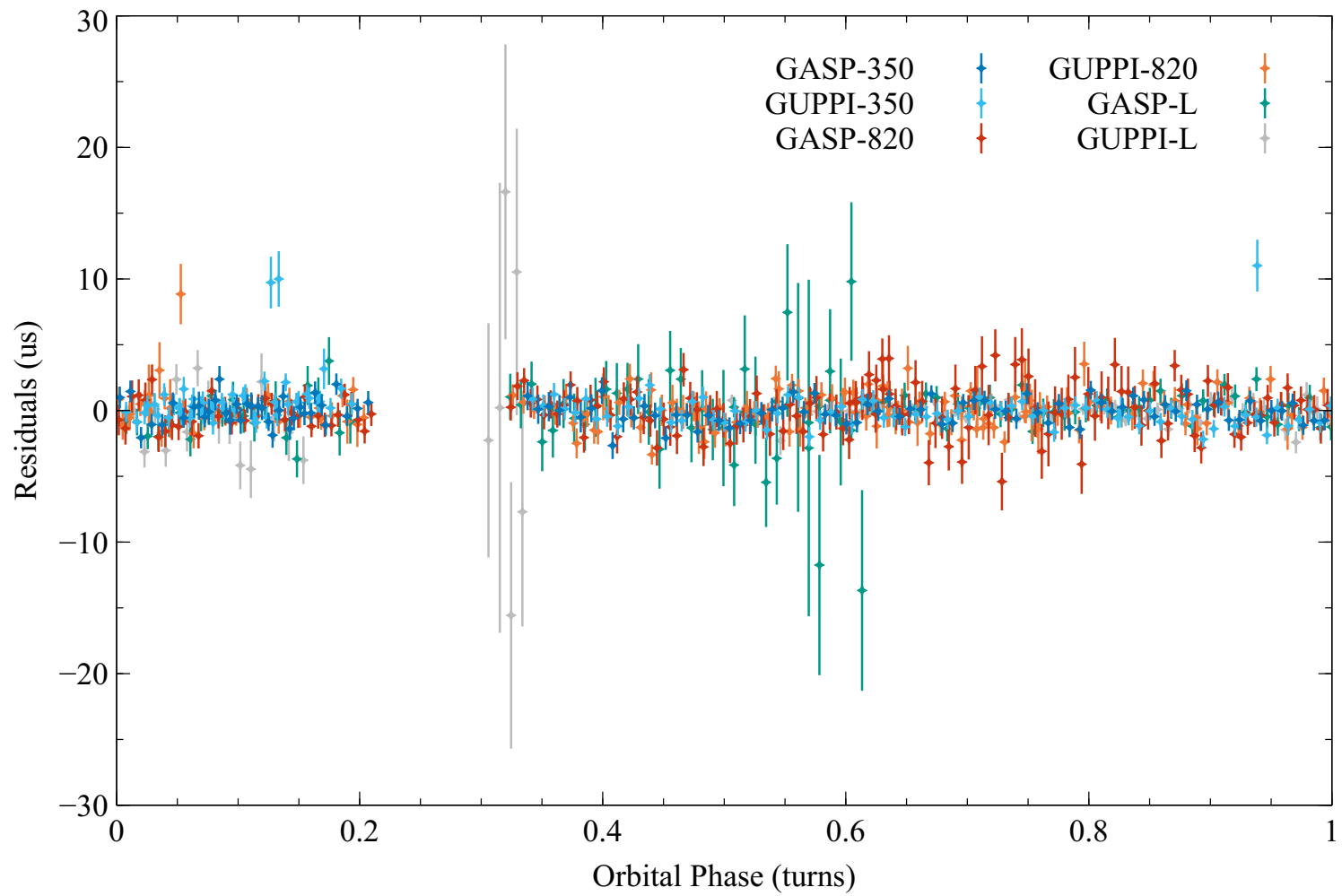


Figure 4.3: Timing Residuals vs Orbital Phase. The eclipse (plus both ingress and egress) and the blip are excluded.

The residuals plotted in Figure 4.2 show a phase-connected solution. There are no obvious periodic patterns and the residuals do not diverge from zero as they get further from the epochs at which values are given², which would be obvious indications of a parameter missing from the model.

That being said there are some residuals which look like outliers. Points with a large spread and large error bars, such as the L-band observation on MJD 55 226, are not concerning. On inspection the pulsar signal fades out towards the end of that observation, likely due to scintillation, causing an accompanying drop in SNR. The large error bars reflect this and mean these points were given less weight in the fitting procedure.

What is cause for concern are residuals which are distinctly off zero and have small uncertainties, e.g., those on MJDs 55 219.

Observation files for outlier TOAs were inspected with `pav`; there were no unaccounted for RFI, the observations had good SNR with the pulsar present and detectable in all of them, and there were no ghost signals or aliasing issues present. As can be seen in Figure 4.3 the outliers are spread throughout the binary orbital phase range and so are unrelated to the eclipse.

There is one possible explanation for the outliers on MJDs 55 219. These TOAs were generated from an observation taken with the band split into a higher number of channels. Therefore their files were `fscrunch`d with the procedure described in Section 2.6. It is possible there was some unforeseen problem caused by this procedure, producing these offsets. However, these `fscrunch`d observations were taken at 350 MHz; the overwhelming majority of other TOAs are at 820 MHz and so these are exactly the TOAs which would be sensitive to frequency dependent parameters like variations in DM.

In any case, a fit was also performed with these `fscrunch`d TOAs removed, and the resulting fit showed no significant changes to any fit parameters.

²PEPOCH, POSEPOCH, T0

4.1.3 Derived Parameters

From the timing parameters fit by TEMPO shown in Table 4.1, by making some assumptions and/or combining this information with independent measurements and models, we can derive more parameters to describe this pulsar system. These derived parameters are shown in Table 4.2.

(i) Using TEMPO Fit Parameters			
Symbol	Description	Value	
l	Galactic Longitude	59.2306563(4) $^\circ$	
b	Galactic Latitude	$-58.2925669(2)^\circ$	
$f(m_p, m_c)$	Mass function	0.00001353004(3) M_\odot	
d_{DM}	Distance, extrapolated from DM	1.3(4) kpc	
d_{px}	Distance, from PX	2.0(6) kpc	
\dot{F}	F1, corrected for Galactic acceleration	$-2.072(9) \times 10^{-15} \text{ s}^{-2}$	
(ii) Assuming a Pulsar with Moment of Inertia 10^{38} kg m^2			
τ	Characteristic age	3.332(15) Gyr	
E_{rot}	Rotational kinetic energy	$3.74922559066686(3) \times 10^{44} \text{ J}$	$3.74922559066686(3) \times 10^{51} \text{ erg}$
\dot{E}_{rot}	Rate of change of rotational kinetic energy	$-3.565(16) \times 10^{27} \text{ W}$	$-3.565(16) \times 10^{34} \text{ ergs}^{-1}$
		$-9.31(4) L_\odot$	
B_{min}	Minimum surface magnetic field	$1.601(4) \times 10^4 \text{ T}$	$1.601(4) \times 10^8 \text{ G}$
(iii) Assuming a Pulsar Mass of $1.4 M_\odot$			
m_c^{min}	Minimum Companion Mass	0.030248746(19) M_\odot	
a	Semi-Major Axis	3.922863(3) lt – sec	
		1.6904446(15) R_\odot	
R_L	Companion's Effective Roche Lobe Radius	0.220(2) R_\odot	
(iv) Including Inclination Angle and Filling Factor			
m_c	Companion Mass	0.0312(9) M_\odot	
a	Semi-Major Axis	4.1(3) lt – sec	
		1.77(15) R_\odot	
R_L	Companion's Effective Roche Lobe Radius	0.232(2) R_\odot	
R_c	Volume-Averaged Radius of Companion	0.09(5) R_\odot	

Table 4.2: Derived parameters (i) using TEMPO fit parameters and physical constants alone, or an external model (ii) assuming the pulsar has a moment of inertia of 10^{38} kg m^2 , (iii) assuming a pulsar mass of $1.4 M_\odot$ and an edge-on orbit with an inclination angle of 90° , and (iv) using the inclination angle of $68(11)^\circ$ and filling factor of $0.4(2)$ found in the optical counterpart detection paper [1]. Note the caveat about this filling factor in Subsection 4.1.3.

Uncertainties shown have been propagated straight from those output by TEMPO

Using the parameters found given by the timing solution, and making a few assumptions, some further parameters can be found to describe the binary system and its components. The timing solution assumes the pulsar and its companion follow a Keplerian orbit, so a mass function can be computed using the standard formula shown in Equation (4.1).

$$f(m_p, m_c) = \frac{(m_c \sin i)^3}{(m_p + m_c)^2} = \frac{4\pi^2 (a_p \sin i)^3}{G P_b^2} \quad (4.1)$$

The right hand side of Equation (4.1) only involves parameters that are fit for by TEMPO, plus physical constants, and so can be easily computed.

Writing the left hand side as

$$f(m_p, m_c) = \frac{m_c}{\left(\frac{m_p}{m_c} + 1\right)^2} \sin^3 i$$

it can be seen that the upper limit for the mass function is $m_c \sin^3 i$ and therefore

$$m_c > \frac{f(m_p, m_c)}{\sin^3 i}$$

From this it is clear the mass function is the absolute lower limit for the companion mass, which is under the assumption that $i = 90^\circ$ and the (far less realistic) assumption of a pulsar with zero mass.

As mentioned in Subsection 1.2.1, with a model for the free electron density distribution in the Galaxy, an estimated distance to the pulsar can be generated from the coordinates of a pulsar and its DM. The result of 1.3289 kpc given in Table 4.2 was obtained using the YMW16 model [45, 46] which determines the parameters for its Galactic model from 189 pulsars with independently measured distances and DMs. For ease of comparison, the previous “standard” electron density model NE2001 [47, 48] gives a DM distance of 0.645 kpc. The NE2001 model gives an estimated uncertainty on the distance by assuming a 20 % error in the DM, finding a range $0.543 \text{ kpc} < d_{DM} < 0.759 \text{ kpc}$. The YMW16 model provides no estimate for the uncertainties on the distance, but following NE2001’s procedure and assuming

a 20 % error in the DM gives $0.9932 \text{ kpc} < d_{DM} < 1.7515 \text{ kpc}$. For Table 4.2 the largest variation ($1.7515 - 1.3289$) was taken as the uncertainty.

Corrections of Effects Due to the Pulsar System's Motion Through the Galaxy

There are a few reasons why the observed first spin period derivatives which we measure with the timing solution, \dot{P}_{obs} , may be different from its intrinsic value at the pulsar, \dot{P}_{int} . This would also impact parameters derived from the observed \dot{P} such as τ , E_{rot} , \dot{E}_{rot} and B_{min} in Subsection 4.1.3. The major contribution to this difference is Doppler shifts due to the pulsar system and SSB moving relative to one another. The following follows Nice and Taylor [99] closely.

Doppler shifts due to their relative velocities are of the form

$$\frac{P_{obs} - P_{int}}{P_{int}} = \frac{\vec{v} \cdot \vec{n}}{c}$$

where \vec{v} is the velocity of the pulsar system relative to the SSB and \vec{n} is a unit vector along the line of sight. This is small correction, ($\ll 1$), and the line of sight velocity cannot usually be measured with pulsar timing. Therefore this correction is generally neglected.

Doppler shifts due to the relative accelerations take the form of

$$\frac{\dot{P}_{obs} - \dot{P}_{int}}{P} = \frac{\vec{a} \cdot \vec{n}}{c} + \frac{\mu^2 d}{c} \quad (4.2)$$

where the transverse component from that along the line of sight, a is the acceleration of the pulsar relative to the SSB, μ is its proper motion, and d its distance from the SSB. Particularly with millisecond pulsars (due to their short periods) this correction is often significant.

The second term in Equation (4.2) due to the transverse motion is known as the *Shklovskii effect* [100]. Unfortunately in this analysis of PSR J2256-1024 values for the proper motion could not be fit and therefore estimating the Shklovskii effect was not possible. Values shown for \dot{F} (a.k.a. F1), and any parameters derived from

it, should be considered with this caveat in mind.

The first term in Equation (4.2) can be decomposed into two parts - acceleration towards the galactic plane, a_Z and acceleration due to the differential galactic rotation between the SSB and the pulsar (within the plane), a_{DGR} . (In the following, l and b are the galactic longitude and latitude of the pulsar respectively)

$$\frac{\vec{a} \cdot \vec{n}}{c} = \frac{\vec{a}_Z}{c} + \frac{a_{DGR}}{c}$$

Nice and Taylor [99] show that, using the Kuijken and Gilmore [101] model for mass distribution in the galactic disc and their values of local mass density ($\rho = 1 \times 10^{-2} M_\odot \text{pc}^{-3}$) and total disk column density ($\Sigma = 46 M_\odot \text{pc}^{-2}$), the acceleration towards the galactic plane can be expressed as

$$a_Z = 1.08 \times 10^{-19} \text{ s}^{-1} c \left(\frac{1.25z}{(z^2 + 0.0324)^{1/2}} + 0.58z \right) \quad (4.3)$$

where z is the distance between the pulsar and the plane, $z \equiv d \sin b$.

For PSR J2256-1024 this component alters the observed period derivative by $(\delta\dot{P}/P)_Z = 1.74(20) \times 10^{-19} \text{ s}^{-1}$. For reference $\dot{P}_{obs}/P = 4.9471(3) \times 10^{-18} \text{ s}^{-1}$. Here the uncertainty in $(\delta\dot{P}/P)_Z$ was calculated by assuming zero uncertainty in the values for l and b^3 , then propagating the estimated uncertainty in d_{DM} through Equation (4.3).

For the shift due to the differing galactic rotations at the pulsar and the SSB, assuming a flat rotation curve it can be shown [99, 102]

$$a_{DGR} = -\cos b \left(\frac{\Theta_0^2}{R_0} \right) \left(\cos l + \frac{\beta}{\sin^2 l + \beta^2} \right) \quad (4.4)$$

where $\beta \equiv d/R_0 \cos b - \cos l$. Using the Reid et al. [103] values for the distance to the galactic center, $R_0 = 8.34(16) \text{ kpc}$, and its rotational velocity, $\Theta_0 = 240(8) \text{ km s}^{-1}$, for PSR J2256-1024 this gives $(\delta\dot{P}/P)_{DGR} = 1.9(7) \times 10^{-20} \text{ s}^{-1}$. Here the uncertainty in $(\delta\dot{P}/P)_{DGR}$ was calculated by again assuming zero uncertainty in l , b , then

³given the relative scale of these errors compared to d_{DM} this is reasonable

propagating the estimated uncertainty in d_{DM} and the Reid et al. [103] uncertainties in R_0 and Θ_0 through Equation (4.4), treating R_0 and Θ_0 as independent variables.

This gives a total correction (not including the Shklovskii component) to \dot{P}/P ($= -\dot{F}/F$) of $1.92(21) \times 10^{-19} \text{ s}^{-1}$, yielding a corrected value of $\dot{F} = -2.072(9) \times 10^{-15} \text{ s}^{-2}$.

Of course these corrections are dependent on the distance measurement used. The values here and in Table 4.2 were computed using the distance derived from the DM, as our parallax measurement is a tentative one. For values which were altered if the parallax distance was used, parallax-distance-corrected versions are given in Table A.2 in Appendix A.

Assuming a Pulsar with Moment of Inertia 10^{38} kg m^2

We assume a pulsar with moment of inertia $I = 1 \times 10^{38} \text{ kg m}^2$, losing rotational energy which is all transformed into magnetic dipole radiation. These assumptions allow us to estimate some characteristic properties of the pulsar, such as its surface magnetic field strength. Derivations of all these quantities are very well covered in Lorimer and Kramer [2].

The canonical pulsar's rotational kinetic energy is given by

$$E_{rot} = \frac{2\pi^2 I}{P}$$

and that energy is changing at a rate of

$$\dot{E}_{rot} = \frac{-4\pi^2 \dot{P}}{P^3}$$

which may also be referred to as the *spin-down power*, \dot{E} , or the *spin-down luminosity* of the pulsar, L_p .

Assuming the rotational energy is being lost solely due to dipole radiation we

can then estimate the surface magnetic field via

$$B \sin \alpha = \sqrt{\frac{3\mu_0 c^3 I}{32\pi^3 R^6} P \dot{P}}$$

where α is the angle between the magnetic dipole axis and the rotational axis of the pulsar, μ_0 is the permeability of free space, and all parameters are in SI units⁴. Letting $\sin \alpha = 1$ then gives the minimum value of B .

The same assumption also leads us to a characteristic age of the pulsar

$$\tau = \frac{P}{2\dot{P}}$$

also called the *spin-down time-scale*.

Values for these derived parameters are given in Subsection 4.1.3. τ , E_{rot} and B_{min} were all calculated using the corrected value for the spin frequency derivative described in Subsection 4.1.3.

Assuming a Pulsar Mass of $1.4 M_{\odot}$

Assuming a standard pulsar mass of $1.4 M_{\odot}$, the mass function can be inverted to produce a minimum mass for the companion. This gave $0.030248765(19) M_{\odot}$, where the uncertainty was calculated treating both the pulsar mass and inclination angle as constants. This very light companion is typical of Black Widow (BW) systems.

Using the minimum value as the companion mass, and assuming an inclination angle of 90° (as radio eclipses are detected, the orbit is expected to be close to edge-on) the semi-major axis of the binary orbit can be found using

$$a = a_p \left(1 + \frac{m_p}{m_c} \right)$$

where a_p is the projected distance from the pulsar to the center of mass (COM), A1.

⁴the more commonly seen equation $B \sin \alpha = \sqrt{\frac{3c^3 I}{8\pi^2 R^6} P \dot{P}}$ assumes CGS units

This can then be used to find an approximation for the effective radius of the companion’s Roche lobe via the Eggleton approximation [104] (Equation (4.5))

$$R_L = \frac{0.49aq^{2/3}}{0.6q^{2/3} + \ln(1 + q^{1/3})} \quad (4.5)$$

where $q = \frac{m_c}{m_p}$ and a is the semi-major axis of the binary orbit. Eggleton notes that this equation agrees with numerically integrated results to 1 % or better and this 1 % was the value used for the Roche lobe uncertainties appearing in Table 4.2.

Incorporating Results from Optical Companion Detection Paper

Breton et al. [1] detected optical counterparts to four BW and RB millisecond pulsars which had been detected with FERMI, among them PSR J2256-1024. Breton et al. [1] took observations using Gemini North [105] and the New Technology Telescope (NTT)’s the tri-band ULTRACAM imager [106] to produce light-curves for the optical companion to PSR J2256-1024. Modelling these light curves (combined with orbital parameters from preliminary timing solution provided to them) the authors were able to constrain some features of the optical companion.

Breton et al. [1] detected an irradiated companion and their models give day-side and night-side temperatures of 4200(700) K and 2450(350) K respectively. This leads to an irradiation efficiency for converting energy emitted from the pulsar’s spin-down into heat on the companion’s surface, ϵ_{1irr} , of 0.07. The best fit model for PSR J2256-1024 also produced an inclination angle of 68(11)° and a filling factor (the ratio of the companion’s volume-averaged radius to its effective Roche lobe radius) of 0.4(2). They note that a corresponding size for the companion would make it “not inconsistent with a solar-composition, degenerate object.”

Still assuming a 1.4 M_⊙ pulsar, these results - namely the inclination angle and the filling factor were used to find the values shown in Table 4.2(iv).

A companion under-filling its Roche lobe to this degree gives rise to the question, how does plasma escape the companion to form the eclipsing cloud? However it is very possible that this filling factor is undervalued. The distance measurement used to constrain the prior of Breton et al. [1]’s model was derived from the DM

using the NE2001 model mentioned above. Holding the filling factor fixed at 1 and removing this distance prior the authors determined PSR J2256-1024 would need to be at 2.3 times this distance to produce their measured fluxes. This would be a distance of 1.495 kpc which is consistent with our value of 1.3(4) kpc, found using the YMW16 model for the galactic free electron density. Therefore, although a volume-averaged radius was computed using the given filling factor and included in Table 4.2, it is very possible that PSR J2256-1024's companion has a filling factor much closer to unity and a radius closer to that of its Roche lobe.

4.2 Eclipse Residuals

The initial hope for this research was to use the highly polarized pulses as a probe of the eclipsing material in the edge-regions of the eclipse, before the signal is completely blocked. Unfortunately the eclipse is quite sharp making gleaning any polarization information from individual sub-integrations difficult. In Section 4.6 we present some effects of the eclipse on the polarization profile of the pulsar. Here, we examine the timing residuals in these regions, looking at delays in the signal as the pulsar enters and exits the eclipse.

Previously, when generating TOAs to find a final timing solution, observations had been scrunched in time to improve the SNR. As mentioned the ingress/egress of the eclipse are both quick and so to investigate the eclipse further, higher time-resolution versions of the appropriate TOAs and residuals were generated. The eclipse was only observed at three epochs as can be seen from Figure 2.1a. The new TOAs were made from the same files as previously and processed exactly as laid out in Chapter 2 except that

1. the observations were not scrunched in time at all in order to give the highest possible time-resolution - that of the original sub-integrations the data was written with.
2. for the GUPPI 820 MHz observation only, a new standard profile was made using solely the data from MJD 55181 observation. For the other eclipse epochs and backends this was already the case but the GUPPI 820 MHz stan-

standard profile used for timing was made from the sum of data from several dates. With no need to add data from multiple epochs the number of bins was also not crunched for this observation.

These were the ways in which the procedure used to generate the higher resolution TOAs differed from that described in Subsection 2.6.2

Residuals were then generated from these by running the new TOAs through TEMPO with the final timing solution parameter file, with all variables frozen so no fit parameters were altered. These residuals are shown for each epoch in Figures 4.4, 4.5 and 4.6.

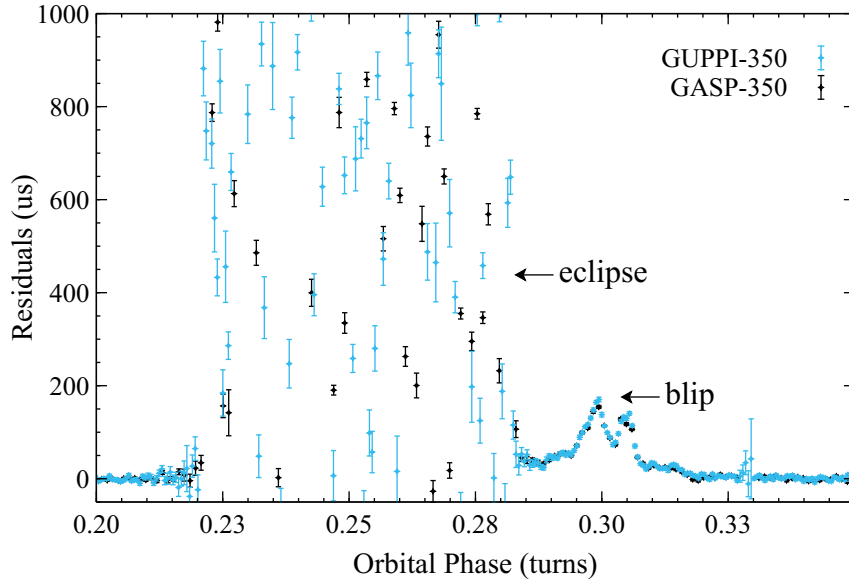


Figure 4.4: Higher time resolution close-up of eclipse observed on MJD 55191 at 350 MHz: Timing Residuals vs Orbital Phase

From Figures 4.4, 4.5 and 4.6 we see the pulses encounter the companion/surrounding material, experiencing larger and larger delays until the signal is completely blocked. With no pulse present the residuals become random until the signal approaches the other edge of the surrounding material. There we again see delayed pulses, with the delays getting shorter and shorter as the line of sight exists the material cloud. It should also be noted that the edges of the eclipse are asymmetrical

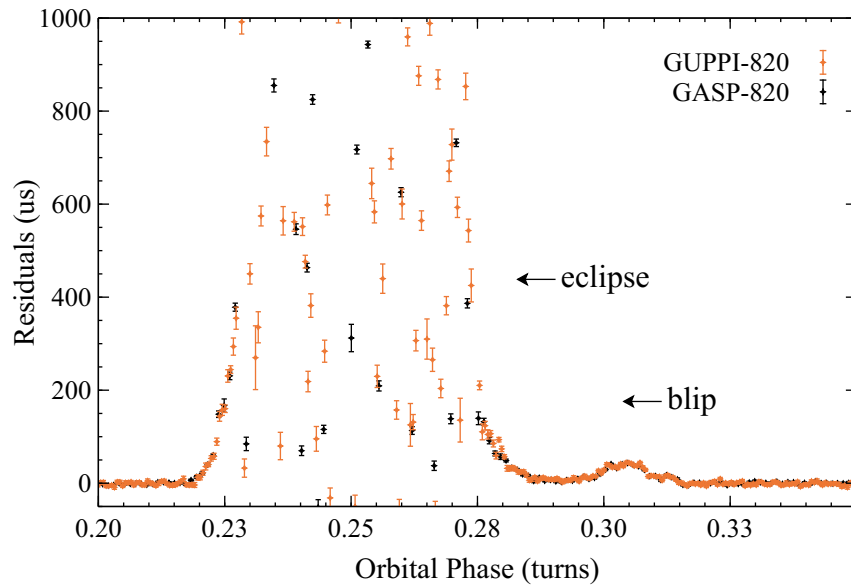


Figure 4.5: Higher time resolution close-up of eclipse observed on MJD 55 181 at 820 MHz: Timing Residuals vs Orbital Phase

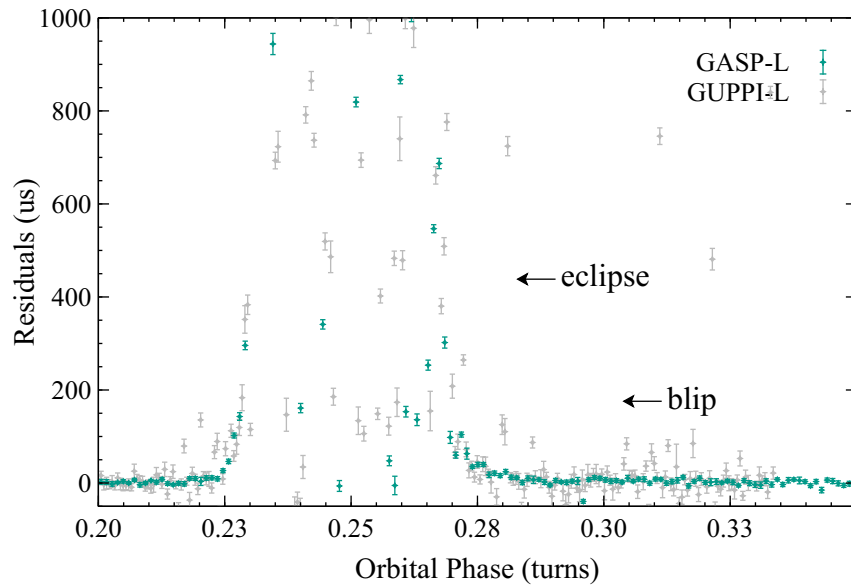


Figure 4.6: Higher time resolution close-up of eclipse observed on MJD 55 226 at L-band: Timing Residuals vs Orbital Phase

with a sharper ingress and a less sharp egress, as it typical of a BW system (and in fact was noticed in the original BW B1957+20 [28]).

In Figures 4.4 and 4.5 after the eclipse there is then a region of delayed residuals separate from the eclipse which has been labelled “blip”. This will be discussed later in Section 4.3.

In Figure 4.6 it is clear that the GUPPI residuals at L-band have larger error bars than those for the GASP data. This is unexpected given GUPPI has a larger bandwidth as covered in Section 2.1. Over the course of this particular observation, the pulsar signal faded out of an increasing amount of the bandwidth which meant that, by the time of the eclipse, there was no benefit from GUPPI’s larger band. In addition because the pulse is only present in a very small subset of the GUPPI band, there is comparatively more noise being added to the GUPPI-measured pulsar signal from the rest of the band. This resulted in lower SNR profiles and larger error bars in the residuals.

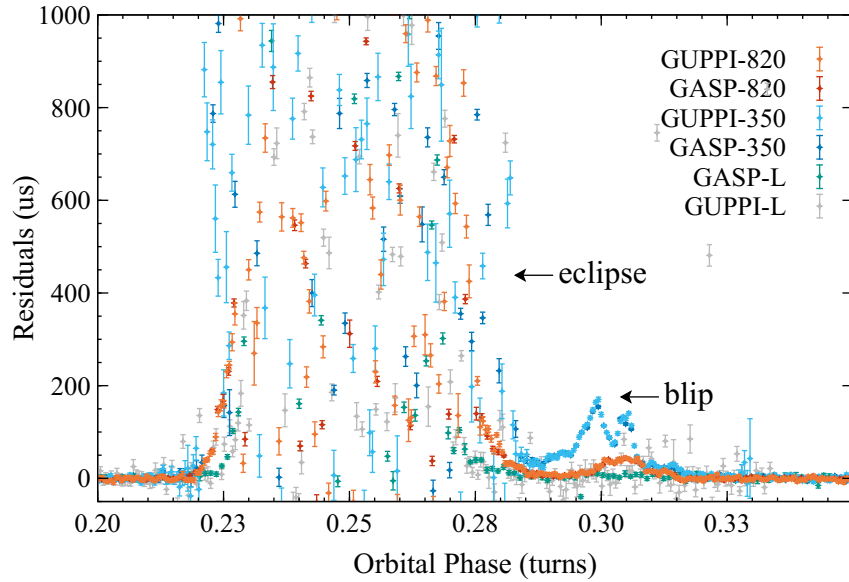


Figure 4.7: Higher time resolution close-up of all eclipses observed: Timing Residuals vs Orbital Phase

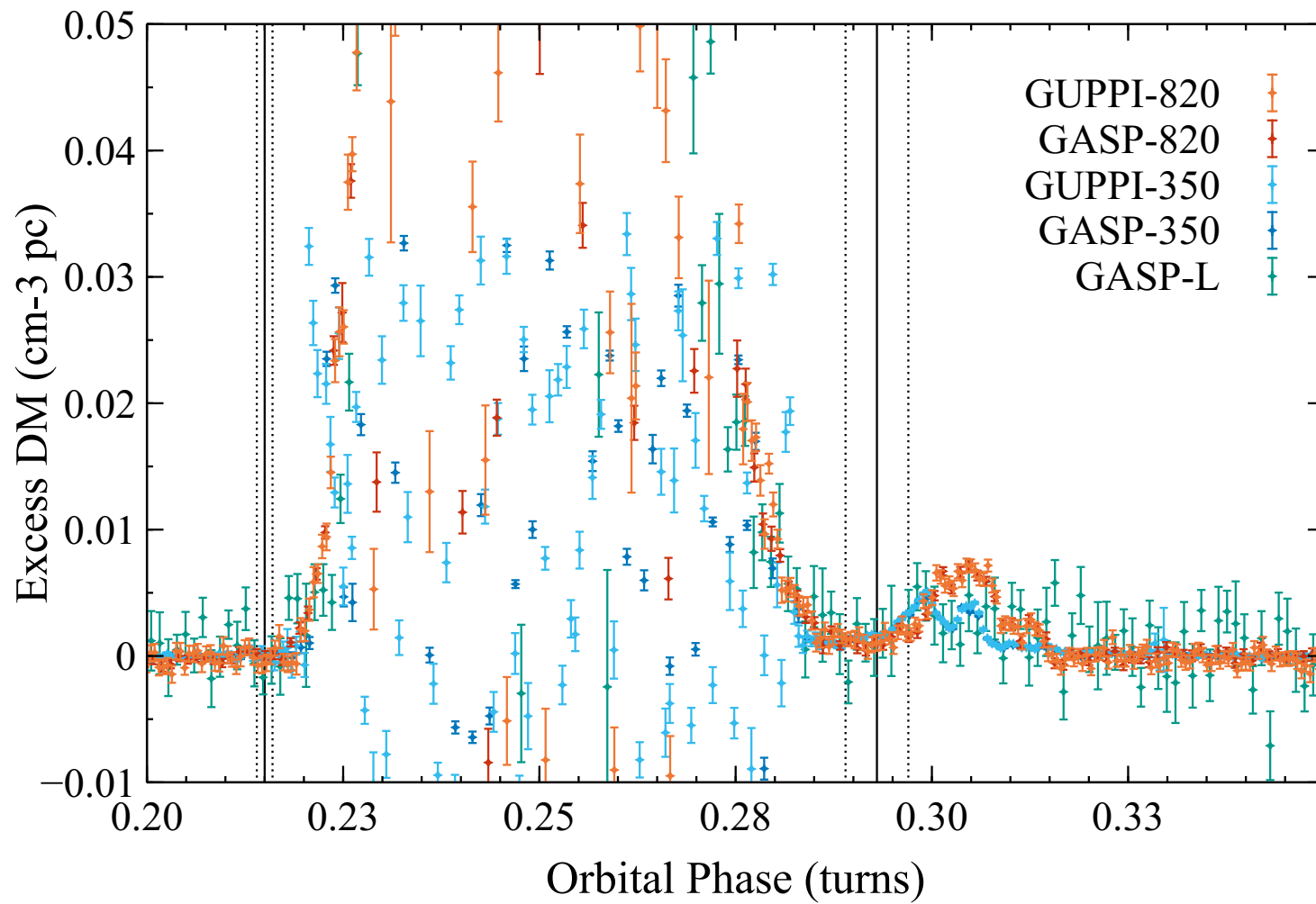


Figure 4.8: Higher time resolution close-up of all eclipses observed: Timing Residuals scaled to give an “Excess DM” vs Orbital Phase. GUPPI L-band data has been excluded for clarity. Vertical lines indicate the location of the eclipse in orbital phase, determined by eye from this plot

Figure 4.7 shows all three eclipses observed. There is clearly some frequency-dependent behaviour; we can see the eclipse is wider at lower frequencies. To explore whether this frequency-dependence is the classic $1/v^2$ behaviour typical of DM, the residuals were scaled by a factor of v^2/\mathcal{K} as per Equation (1.1),⁵ to form an “Excess DM”. This is then plotted in Figure 4.8. The residuals’ uncertainties were also scaled by the same factor, thus the already-large GUPPI L-band error bars would dominate the plot and have been excluded. Figure A.1 in Appendix A shows this plot with the L-band GUPPI included.

From Figure 4.8 the eclipse approximately follows a $1/v^2$ frequency dependence. There is a hint that there may be some divergence from this, particularly comparing the 350 MHz and 820 MHz data at the eclipse exit, but nothing definitive. The extent occurs approximately from 0.215(1) to 0.293(3) in binary orbital phase; this range is marked on the plot. This allows for the size of the eclipsing material to be estimated. Both the eclipse limits and the uncertainties were determined by eye from Figure 4.8. It should be noted that determining the orbital phase of the end of the eclipse was complicated by the presence of the blip. From Figures 4.4 and 4.5 it can be seen that the residuals do not revert to normal levels in between the eclipse and the blip, therefore some degree of personal judgement was used determining the eclipse “end”.

Parameter	Assuming $i = 90^\circ$	Using $i = 68(11)^\circ$, filling factor = 0.4(2)
a	1.6904446(15) R_\odot	1.77(15) R_\odot
X_{orbit}	0.81(3) R_\odot	0.84(8) R_\odot
$2R_L$	0.440(4) R_\odot	0.464(5) R_\odot
$2R_c$	–	0.19(9) R_\odot

Table 4.3: Possible size of the eclipsing material, X , given the eclipse’s position in orbital phase and the derived semi-major axis (Subsection 4.1.3). The companion’s effective Roche Lobe diameter and its volume-averaged diameter (Subsection 4.1.3) are included for easy comparison

Given the extent of the eclipse in orbital phase, the size of the eclipsing cloud

⁵ \mathcal{K} therefore being $4.148808 \times 10^3 \text{ MHz}^2 \text{ cm}^3 \text{ s pc}^{-1}$

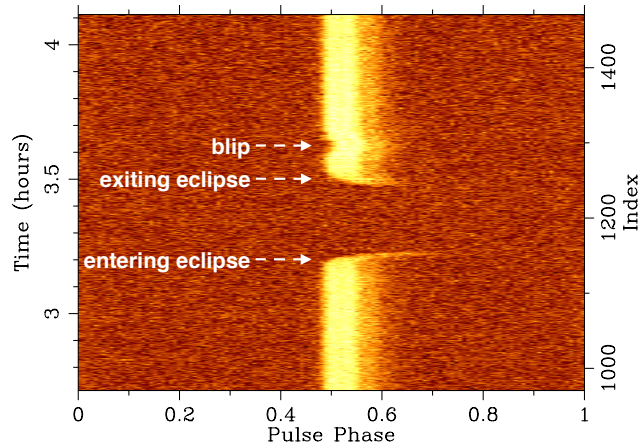
was calculated, X_{orbit} , assuming the material follows the companion along its orbit.

As mentioned in Subsection 4.1.3 the optical counterpart paper [1] found a filling factor of 0.4(2) for the companion but noted their distance may be undervalued and the companion may well be larger. From Table 4.3 even if the companion is filling its Roche Lobe the eclipsing material is approximately double the companion's size. This confirms that the eclipses are due to surrounding material rather than just the companion itself. In practice both the pulsar wind and the solar wind from the companion will be affecting the cloud of material so for it to follow in the companion's orbit is improbable. The cloud is more likely to form some sort of cometary tail as noted by Rasio et al. [107] in their numerical model of possible eclipse mechanisms in B1957+20.

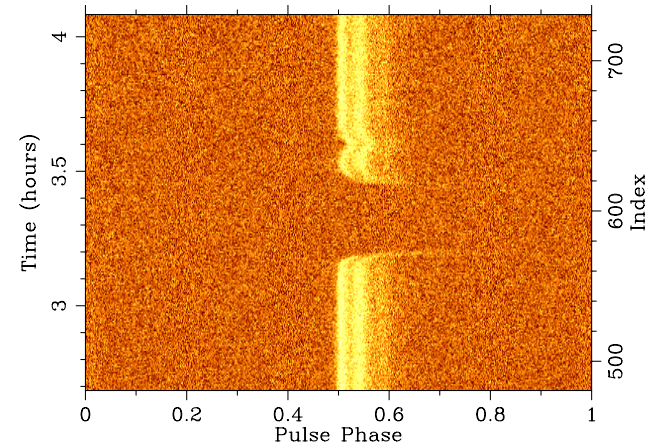
4.3 “Blips”

In two observations a section of delayed pulses closely following (but distinct from) the eclipse is seen. For lack of a better term, these are referred to as “blips” throughout this thesis. A blip is seen on MJD 55 181 at 820 MHz. On this occasion data was being taken simultaneously with GASP and GUPPI; both backends recorded the blip. A blip also appears in the following observation 10 days later, this time data was taken at 350 MHz and again recorded with both backends. Figure 4.9 shows intensity as a function of pulse phase and orbital phase, during the eclipse and surrounding region, for both observations where the blip was recorded. The only other observations which sample this region of the orbital phase were both taken at L band on MJDs 55 226 and 55 354 and no blip is seen.

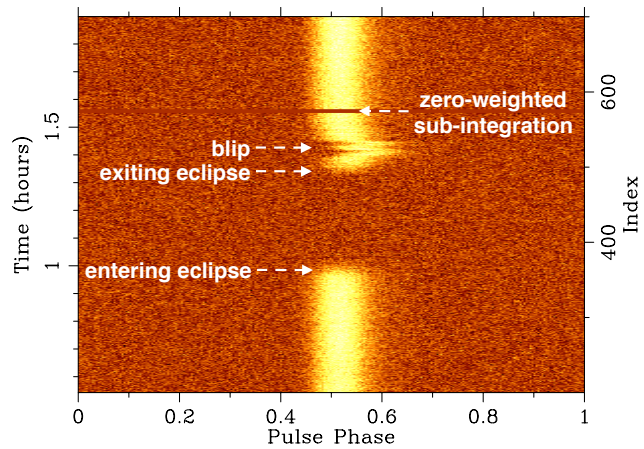
Figure 4.9 shows plots of the pulse phase against time for the region in and around the eclipse. As in Figures 4.4, 4.5, 4.6 and 4.7, we see (a) the pulsar signal encounter the companion/cloud, (b) a dispersive smear as the pulses are delayed by the excess material, (c) a gap where the pulses are completely blocked, (d) another dispersive smear as the pulsar comes out of the eclipse, (e) another section of delayed pulses - a blip, before the pulses resume their “normal” behaviour.



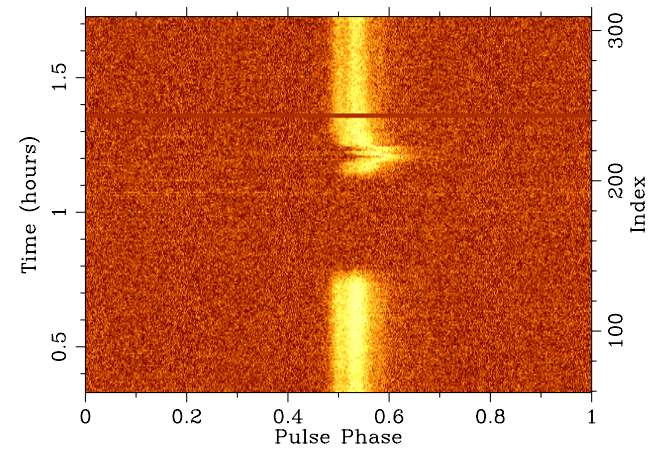
(a) Eclipse at 820 MHz on MJD 55 181 - GUPPI



(b) Eclipse at 820 MHz on MJD 55 181 - GASP



(c) Eclipse at 350 MHz on MJD 55 191 - GUPPI



(d) Eclipse at 350 MHz on MJD 55 191 - GASP

Figure 4.9: Plots of the “blip” on both MJDs on which it was seen, with each backend

A blip appears on two separate days, in observations at two different frequencies and is recorded with two different backends, with no sign of data corruption or other errors. Given these factors we are reasonably confident it is a real feature and likely due to a clump of material in the system blown off from the companion and surrounding eclipsing material.

To examine the blips more closely higher time-resolution residuals were used - the same ones as described in Section 4.2, and these are plotted in Figures 4.10, 4.11 and 4.13.

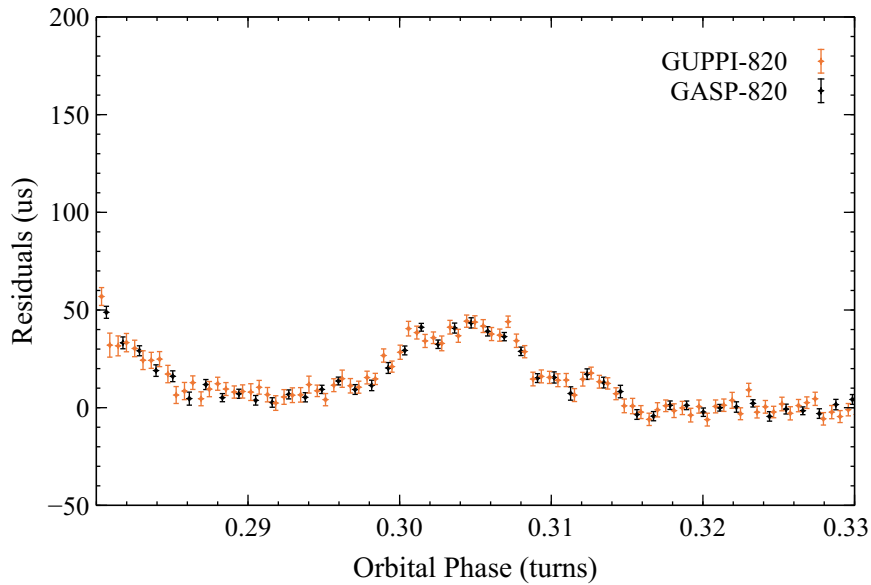


Figure 4.10: Higher Time Resolution Close-up of the Eclipse and Blip on MJD 55 181 at 820 MHz

Comparing Figures 4.10 and 4.11 shape differences in the blips are evident. From this several possibilities suggest themselves:

1. Both blips are due to a single clump. There has been some physical change in the clump's shape or density distribution during the 10 days between observed blips.
2. Both blips are due to a single clump. Differences in morphology are the

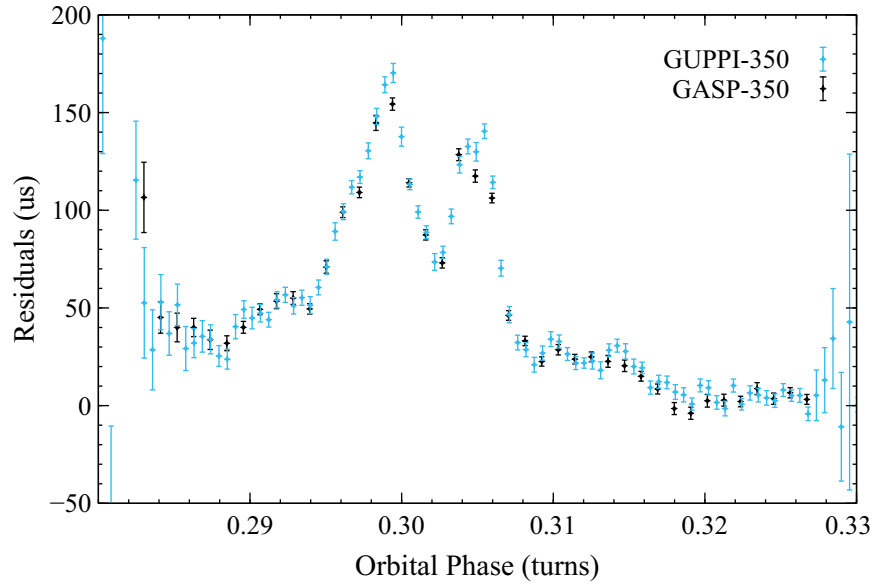


Figure 4.11: Higher Time Resolution Close-up of the Eclipse and Blip on MJD 55 191 at 350 MHz

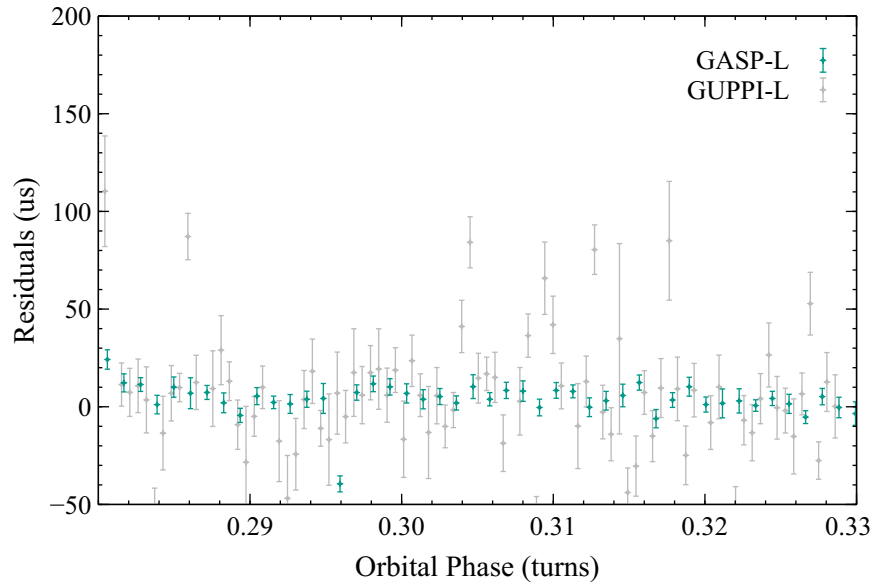


Figure 4.12: Higher Time Resolution Close-up of the Eclipse on MJD 55 226 at L-band

result of probing the material with two different frequencies.

3. The blips are due to different clumps.

Of course in the event of either 1 or 3 they will likely be combined with the effect from probing with different frequencies. One or all of these factors would also account for why the blip is not seen on MJDs 55226 and 55354; both are some time later by which time the clump could have moved away or dispersed, and also at a higher frequency which would be less affected by scattering or dispersive processes.

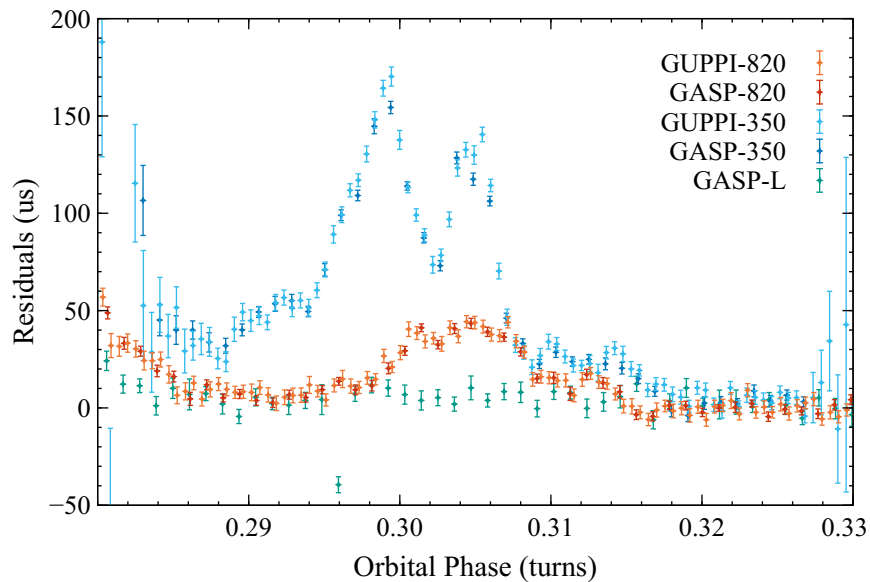


Figure 4.13: Higher Time Resolution Close-up of the Blip vs Orbital Phase - Data from MJDs 55181, 55191 and 55226 taken at 820 MHz, 350 MHz and 1500 MHz respectively. The GUPPI MJD 55226 data is omitted from this plot for purposes of clarity - the large error bars obstructed the view of the other data sets

From Figures 4.10, 4.11, 4.12 and 4.13 a few features are worth noting. Firstly, the blip was not detected on MJD 55226 at L-band. Secondly, many peaks are seen within the blips - the clumps of material must themselves be clumpy. Thirdly, the residuals do not drop back to baseline between the eclipse and the blip at 350 MHz

or 820 MHz. There is likely some continuum of material between the clumps and the eclipsing cloud or, if not a continuum, additional material in the orbit along the line of sight in this phase region.

MJD	Central Frequency MHz	Excess DM cm^{-3}pc
55181	820	0.0073(16)
55191	350	0.0048(4)

Table 4.4: Excess DM due to the clumps on MJDs 55 181 and 55 191

An excess DM was calculated for each blip by taking the peak residual (in the blip region) for each MJD, and its uncertainty, then combining these with Equation (1.1) and the central frequency of the observation⁶. Table 4.4 shows the results of this procedure, the peak excess DMs extrapolated from each blip are consistent with each other at 2σ implying they could be due to the same clump. However scaling the residuals were by a factor of v^2 to form an excess DM (as per the method described for Figure A.1) gives a clearer picture. These excess DMs are plotted in Figure 4.14.

Immediately from Figure 4.14 it is clear that timing delays from a clump which caused either or both blips would not have been detected at L-band. The only other two observations covering this orbital phase region (on MJDs 55 226 and 55 354), were both taken at L-band and so if any similarly-sized clumps were present at these times they would not have been detected.

Figure 4.15 shows the excess DM for the two blips that were detected. The blips are not consistent with each other leaving the possibilities that both are due to one clump of material which spread out over the intervening 10 days, or the blips are due to two separate clumps. Without more information we are unwilling to say which of these two scenarios cause the blips. There is also the possibility that the clump does not cause a $1/v^2$ relationship but given that (from Figure A.1) the eclipse itself obeys that relation, this seems unlikely.

No other blips or evidence of clumps are seen in observations. However, this

⁶remember that these TOAs had been Fscrunchd - summed to one frequency channel

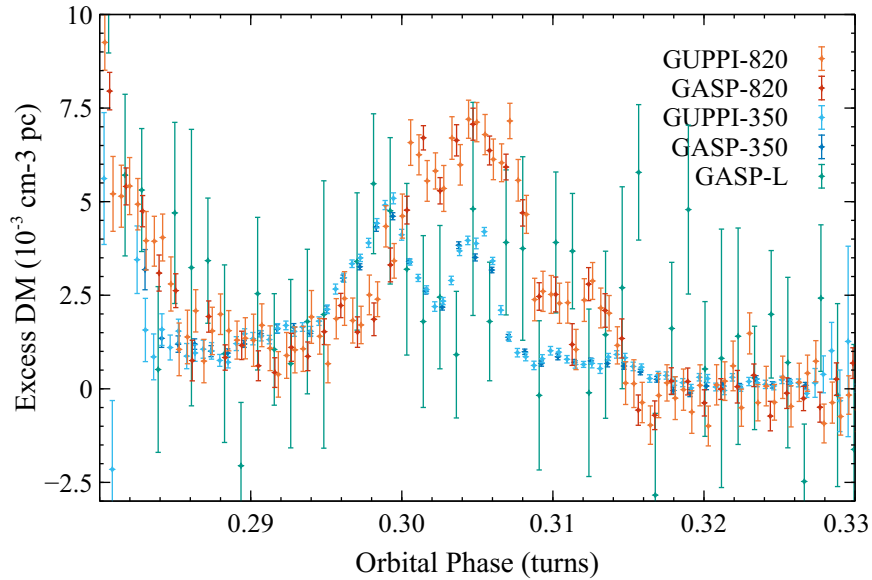


Figure 4.14: Higher time resolution close-up of blips observed: “Excess DM” vs Orbital Phase. GUPPI L-band data has been excluded for clarity

is likely due to the key factor that observations were not scheduled with the aim of looking for them. If the blips are due to clumps of matter coming off the companion and surrounding material, we’d expect to see them in the region just after the eclipse. For most observations in the data span, the object was to get TOAs over a longer time span to improve the timing solution. So, to be reasonably sure of detecting the pulsar and getting TOAs, times when PSR J2256-1024 was in or near eclipse were purposefully avoided. This can be seen clearly in Figure 2.1a MJDs. 55 181, 55 191 and 55 226 were special and the exceptions to this rule - data was intentionally taken to cover the eclipse region and as much of the binary orbit as possible.

With just two data points we can only make speculations. It may be that clumps are rare and we were lucky to catch them on MJD 55 181 and 55 191. However given we found evidence of separate clumps on the only two occasions when sampling the appropriate region of orbital phase with a frequency that would detect them it is likely that this is a common occurrence. This is supported by reviewing

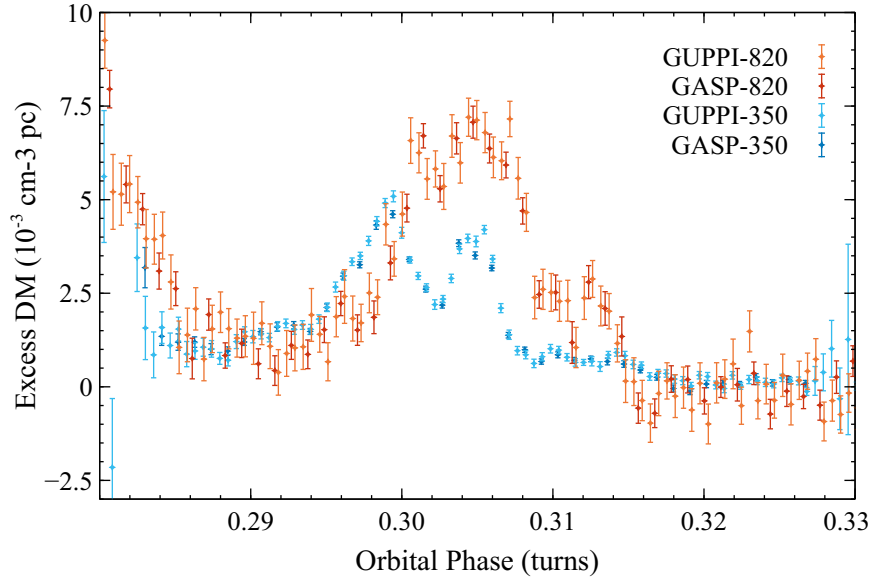


Figure 4.15: Higher time resolution close-up of the blips recorded on MJDs 55 181(820 MHz) and 55 191(350 MHz): “Excess DM” vs Orbital Phase

literature on RBs and other BW systems. A blip can be seen in a recent paper on B1957+20 [108, Figure 1], Archibald et al. [24] note a blip in their data due to large variations in DM at the eclipse egress in J1023+0038, “mini-eclipses” are seen in radio observations of J1048+2339 [109], and Polzin et al. [110] see “significant deviations from the out-of-eclipse electron column density” in J1810+1744 eclipse egresses. Stappers et al. [111] found evidence for both structure and variability in the eclipsing medium of J2051-0827; given Rasio et al. [107] makes it clear that even when past the “eclipse region”, the proposed cometary tail of plasma streaming from the companion is still being sampled, it follows that structure and variability are likely to be seen in later parts of the tail too.

4.4 Rotation Measure

The observations’ RM was measured and corrected for using the `rmfit` program within the PSRCHIVE software suite [77]. RMs were found using observations

at three epochs (MJDs 55 181, 55 191 and 55 226) during which data was taken concurrently with both GASP and GUPPI over a long enough stretch of time to cover the entire binary orbit⁷.

The hope was to look for RM changes as PSR J2256-1024 approaches and exits eclipse at multiple frequencies and thus gain some insight into the eclipsing medium. Unfortunately, as mentioned, the entrance and exit from the eclipse is comparatively sharp, happening over just a few sub-integrations and the SNR was not high enough in individual sub-integrations to allow any RM changes to be measured.

4.4.1 Pre-Processing

Observation files underwent RFI excision as per Section 2.3 and were polarization calibrated as described in Section 2.4. Sub-integrations containing eclipses, showing dispersive smears pre- or post-eclipse, and any containing “blips” (see Section 4.3) were zero weighted using `paz`. During a long observation data is written to multiple files, starting a new file once a maximum size has been reached. Individual files from one epoch and backend combination (e.g., , GUPPI on MJD 55 181) were combined together using `psradd`, phase aligning the added profile with the total before the addition and Tscrunching the total after each file was added. So for each observation session being used for RM determination, there are four total integrated Stokes profiles for each frequency channel.

4.4.2 Measuring RM with `rmfit`

`rmfit` has a few algorithms for determining RM, a “Quadratic fitting algorithm”, a “Brute force search for peak linear polarization” and an “Iterative differential position angle refinement”. The quadratic fitting algorithm [112] although shown to be an improvement over the other methods [112] was found to not be appropriate for PSR J2256-1024. It first computes an average polarization position angle for every frequency channel, then fits a quadratic function to these average polariza-

⁷for more details of the observations see Table 2.1

tion position angles, using a Bayesian likelihood test to determine the best fit to the data. When applying this procedure to PSR J2256-1024 it was likely the first step causing problems - PSR J2256-1024's polarization position angle profile is mostly flat and jumps between plateaus (see Section 4.5), in what is known as orthogonal polarization mode changes [113], and so computing an average polarization position angle per frequency channel produced results which could be very different in consecutive frequency channels.

MJD	Backend Instrument	Central Frequency MHz	Bandwidth MHz	Number of Frequency Channels	RM rad/m ²
55191	GUPPI	350.0	100.0	2048	15.21(2)
55181	GUPPI	820.0	200.0	2048	14(1)
55181	GASP	822.0	64.0	16	10(3)
55226	GUPPI	1500.0	800.0	1024	20.7(2)
55226	GASP	1392.0	84.0	21	24(6)

Table 4.5: RM values from using the "brute force" `rmfit` algorithm.

GASP data has a narrower bandwidth and fewer frequency channels. As RM has a frequency squared dependence, those observations less useful to determine RM. They are shown to demonstrate that GASP RM values are consistent with their GUPPI counterparts for the same observation. The GASP data at MJD 55 191 was unable to be fully calibrated and so RM was not measured.

The brute force search produces a list of trial RMs from a given minimum, maximum and number of steps. Per trial RM, it then corrects the observation for that RM and computes the total L. A Gaussian is fitted to the resulting plot of L against the trial RMs. The RM returned is the centroid of this Gaussian⁸. An initial estimate of PSR J2256-1024's RM was found in this way using a minimum RM of -100 rad/m², a maximum of 100 rad/m² and 1000 steps, producing the results in Table 4.5. This is a good rough method but can produce some odd results, for example if the plot is asymmetrical the Gaussian fit is often visibly offset from the peak. Plus it has been noted [114] there are some problems with just using the maximization of L to determine RM.

⁸if the Gaussian fit fails, the RM which produced the maximum L is returned

The iterative method is then a means of refining an initial rough RM value. This was done for PSR J2256-1024 using the values given by the brute force method as input.

The iterative algorithm takes the initial input RM and corrects the observation for Faraday rotation using the given RM. It then splits the frequency band in half and computes the *weighted differential polarization position angle*⁹ between the band halves. If the weighted differential polarization position angle is significant (larger than its uncertainty) the observation is corrected using the new derived RM and the process is repeated until a final RM is arrived at.

The resulting RMs from this iterative method are shown in Table 4.6. The values found were not all consistent with each other; ionospheric effects were considered as a possible explanation for this discrepancy.

MJD	Backend Instrument	Central Frequency MHz	RM _{rmfit-iterative} rad/m ²	Average RM _{ion} over observation rad/m ²
55191	GUPPI	350.0	15.04(5)	1.8(3)
55181	GUPPI	820.0	13.4(5)	1.5(3)
55226	GUPPI	1500.0	14.2(8)	1.7(3)

Table 4.6: RM values determined from the pulsar observations by the `rmfit` iterative algorithm and the average ionospheric contributions to the RM during those observations as computed by the `ionFR` code, which uses the IRI model for the ionosphere

4.4.3 Ionospheric Contributions

As discussed in Subsection 1.2.3 the pulsar signal undergoes Faraday rotation by virtue of being a strongly linearly polarized wave travelling through a plasma with a magnetic field component along the direction of propagation. However the pulse goes through (at minimum) two plasmas - the ISM and the Earth’s ionosphere. In order to determine any intrinsic variations in the RM or those due to changes in the line of sight to the pulsar, we must first account for those in the ionosphere.

⁹details of which can be found here <http://psrchive.sourceforge.net/manuals/rmfit/DeltaPA.pdf>

The Faraday rotation due to the Earth’s ionosphere was modelled using the *ionFR* code [115], which in turn uses data from the IRI [116]. The IRI uses ”all available data sources” to produce an empirical model of the ionosphere for a given time and place. The *ionFR* code then models this as a thin shell and accounts for things such as the line of sight to the source, producing an hourly value and uncertainty for the ionospheric RM, RM_{ion} , for a given source and observing location.

Each of the observations used to measure RM are several hours long; Table 4.6 shows the average RM_{ion} during the observation and the uncertainty quoted is the maximum uncertainty for any RM over the observation.

As can be seen from Table 4.6, accounting for ionospheric effects, the RMs measured for PSR J2256-1024 overlap just under 3 sigma. This could hint at some intrinsic RMs variations but it is more likely there are some unaccounted for systematic errors, or the uncertainties given by `rmfit` are undervalued.

Due to the position of PSR J2256-1024 RM variations are unlikely to be due to solar activity in our solar system (sunspots, coronal mass ejections, etc) as the signal path does not pass very close to the sun. There could be some variation from the proper motion of the pulsar (and therefore changing line of sight) or in the ISM itself but these are not expected [117] and in that case we would expect variation over longer time-scales. The MJDs 55 181 and 55 191 values for RM are furthest apart here so the timescale to consider is ~ 10 days. Variations could be due to short-term ISM fluctuations or deviations in the local environment of the pulsar system. Given it’s a Black Widow (BW) system which is expected to be populated with excess material from the ablated companion this is a possibility, but investigating would require further RM measurements over more epochs.

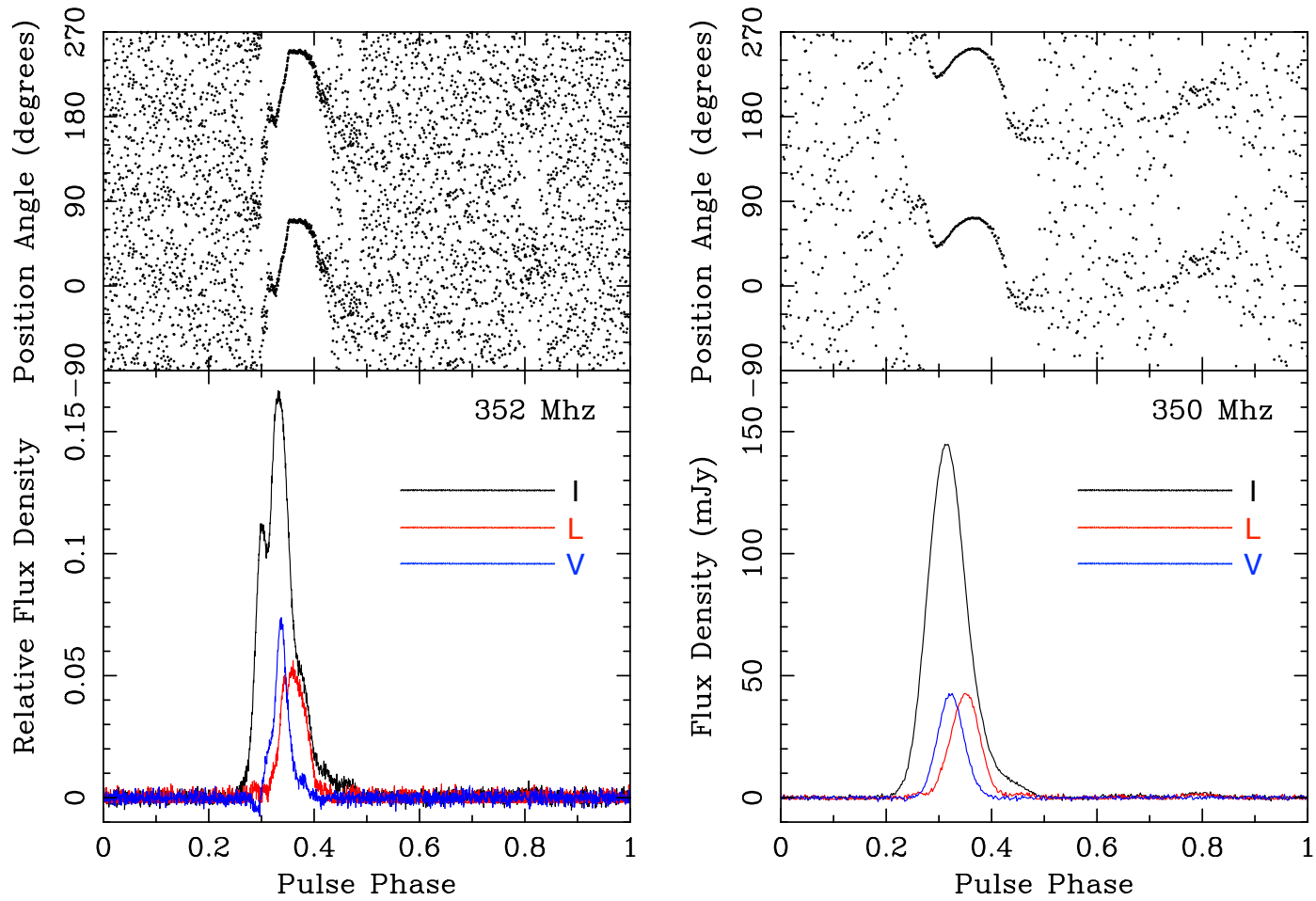
4.5 Polarization Profiles

Presented here are the polarization profiles found for PSR J2256-1024 at 350 MHz, 820 MHz and 1500 MHz. These were made using data from three epochs where observations covering the whole binary period were taken, MJDs 55 181, 55 191

and 55226 respectively. During these three epochs data was taken simultaneously with both GUPPI (in filterbank mode) and GASP backends. One polarization profile is presented per frequency and backend combination. The effect of the eclipse on polarization profiles are discussed in Section 4.6.

To form these profiles RFI mitigation and polarization calibration as described in Sections 2.5 and 2.4 were performed. Note that each profile was corrected for rotation measure (RM) using the RM measurement obtained from the GUPPI scans on that epoch. It should also be noted that, due to a lack of fluxcal, the GASP MJD 55191 observation underwent the less robust calibration procedure described in Section 2.4. This profile is therefore a plot of relative (rather than absolute) flux density vs pulse phase. The eclipse and any blips were cut out of the observation files with `paz`, then the remaining files were summed together with `psradd`. Files were phase-aligned with the total before being added to it, and after each addition the total was fully time-scrunched down to one sub-integration. The files were also Fscrunched to one frequency channel. To avoid blurring any potential features in the profile shapes, no bscrunching (scrunching in phase bins) was done.

Figure 4.16 shows these polarization profiles. On the bottom is a plot of the Intensity (I), linear polarization (L) and the circular polarization - Stokes V, plotted against pulse phase. On the top is the polarization position angle, Φ , displayed over a 360° range (therefore appearing twice) to more clearly show features and shapes. The profiles were rotated by 0.3 in pulse phase for easier viewing of the pulse shape.



(a) GASP coherently dedisersed, summed over 24 MHz of bandwidth. Note the flux density here is relative as this observation could only be partially calibrated

(b) GUPPI filterbank, summed over 100 MHz of bandwidth

Figure 4.16: Polarization profiles for PSR J2256-1024 at 350 MHz on MJD 55191

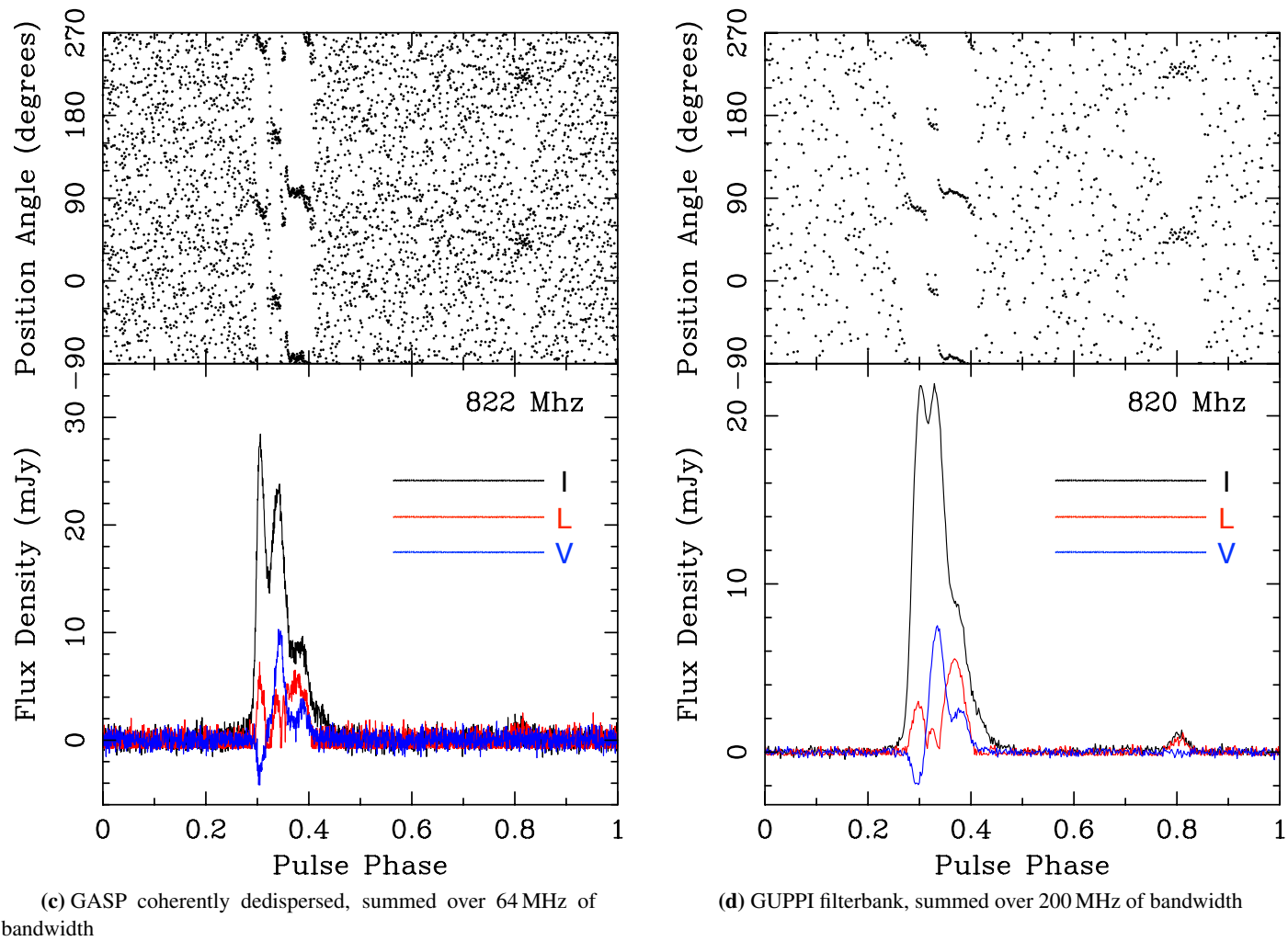


Figure 4.16: Polarization profiles for PSR J2256-1024 at 820 MHz on MJD 55181

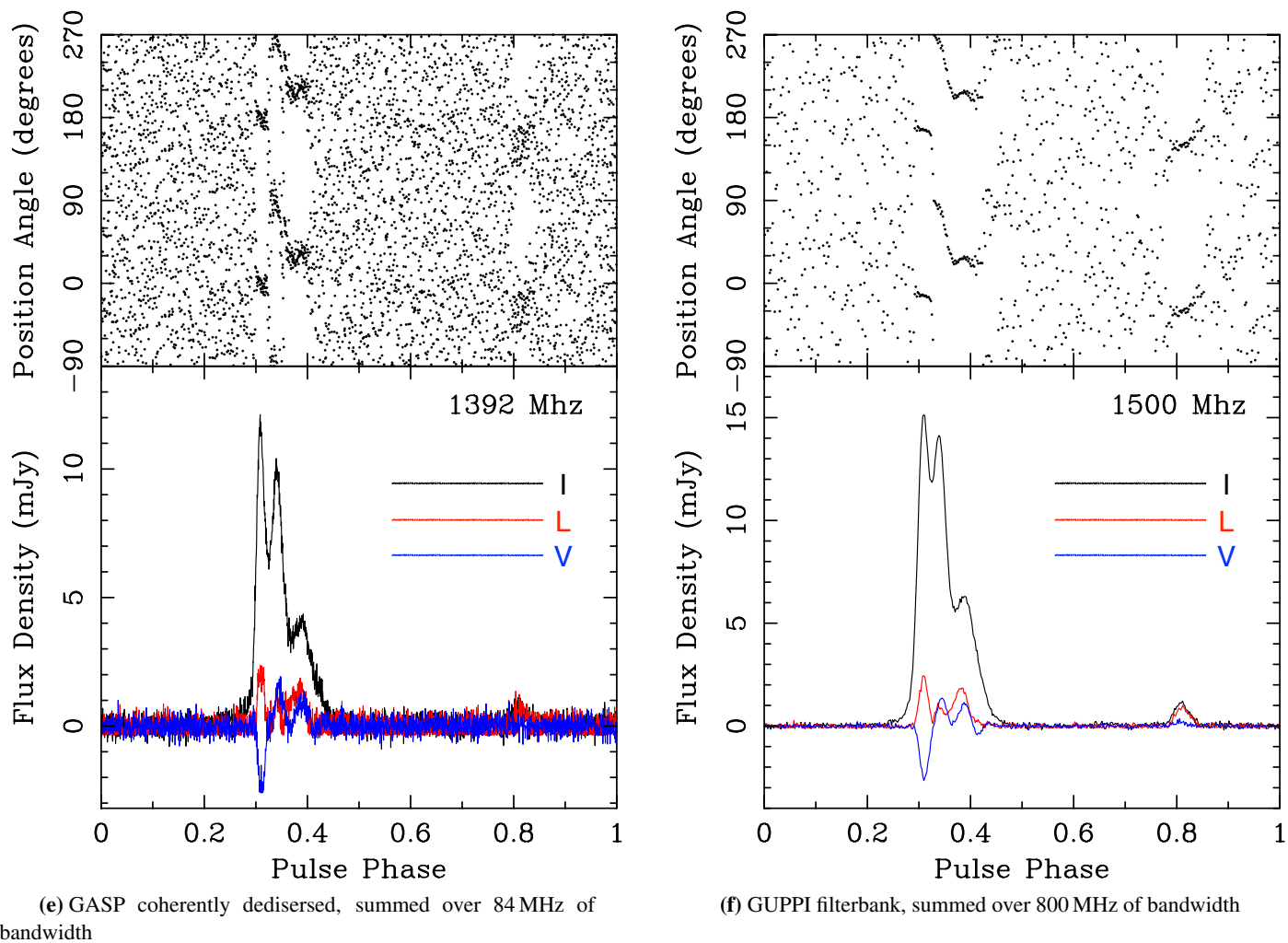


Figure 4.16: Polarization profiles for PSR J2256-1024 at L-band on MJD 55226

From Figures 4.16 and 4.16 we can clearly see an interpulse opposite (offset by 0.5 in pulse phase) the main pulse which is also suggested in Figure 4.16. Features of the main pulse include a large double peak with a smaller, additional peak to one side, and large circular polarization comparable to or larger than L.

By comparing plots at different frequencies we get some idea of the profile's frequency evolution. As the observing frequency increases the height difference between the double-peak and its subsidiary to the side decreases. Within the double-peak, the left peak is smaller than that the right at 350 MHz, their relative height then decreases and changes direction until at L-band the left peak is taller.

Comparing the GUPPI and GASP profiles at the same frequency, the GASP profiles have a lower SNR since GASP has a smaller bandwidth than GUPPI. Some differences between GUPPI and GASP profiles will be caused by coherent dedispersion offering greater resolution of the profile shape - e.g., at 350 MHz the GUPPI profile is very Gaussian whereas in the GASP profile more structure emerges. However, since GASP's bandwidth is contained within GUPPI's, some differences are likely due to a varying profile shape over the GUPPI band. It should also be noted, at 350 MHz, some changes will be due to the different calibration procedures.

From these profiles we can also compute a mean flux density at each frequency by summing over the pulse shape and dividing by the number of bins within the pulse. These results are given in Table 4.7.

Backend Instrument	Central Frequency MHz	Mean Flux Density mJy
GUPPI	350	51
GASP	822	16
GUPPI	820	8.7
GASP	1392	5.8
GUPPI	1500	5.2

Table 4.7: Mean flux densities found for each fully calibrated backend and frequency combination

The difference between the GUPPI and GASP flux densities at 820 MHz is due to PSR J2256-1024 being bright in the GASP part of the band at this particular epoch.

Pulsar flux densities vary in time with the major contribution being from refractive scintillation [118]. Without reliable measurements of the flux density at more epochs, the scale of this variability is difficult to determine and is approximated to be 20 %.

Assuming a 20 % uncertainty, performing a simple linear fit on a logarithmic plot of the values in Table 4.7, gives a spectral index of $-1.56(17)$. The spectral index being α within the assumption that the flux density, S , has a power law dependence on frequency, $S(\nu) \propto \nu^\alpha$.

$-1.56(17)$ is a fairly typical value for α for the pulsar population as a whole; a recent paper on the spectral properties of 441 pulsars found a weighted mean spectral index of $-1.60(3)$ for pulsars whose spectra could be described with a simple power law [119].

However, for the population of gamma-ray MSPs (to which PSR J2256-1024 also belongs [70]), there have been suggestions that steeper spectral indices may be more common. Kuniyoshi et al. [120] note a tendency for gamma-ray pulsars to be steeper spectrum outliers in their sample. Frail et al. [121], when looking at the spectral index distribution of pulsars, find among their steepest-spectrum ($\alpha < -2.5$) objects a “preponderance of gamma-ray pulsars” along with an “unusually large fraction of (eclipsing) binaries”. If true (both papers caution that this “correlation” may be due to biases) PSR J2256-1024 would have a comparatively shallow spectrum compared to other eclipsing binaries and gamma-ray MSPs.

4.6 Effects of the Eclipse and Blip on Polarization Profiles

As mentioned previously the eclipse ingress and egress are rather sharp, so the higher time resolution observations of Section 4.2 were used to look for polarization changes. The SNR is very low but some distinct features can be discerned.

Figures 4.17, 4.18, 4.19 and 4.20 show the degree of linear polarization, L/I , the polarization position angle, Ψ , and the degree of circular polarization V/I plotted against the pulse phase of the pulsar and the orbital phase for GASP and GUPPI observations on MJDs 55 181 and 55 191 (at 820 MHz and 350 MHz respectively). Plotting the parameters in this way lets us observe how the polarization profile shape changes as the pulse encounters the eclipse and blips. L-band data is not shown as the SNR was too low.

For these plots, with both degrees of polarization and the polarization position angle, two low SNR Stokes parameters have been combined to form the plotted values. This means where there is no signal, combining the two noise values produces results over a large range. In these plots the signal then emerges from the rapidly varying colours of the noise as regions of similar colour.

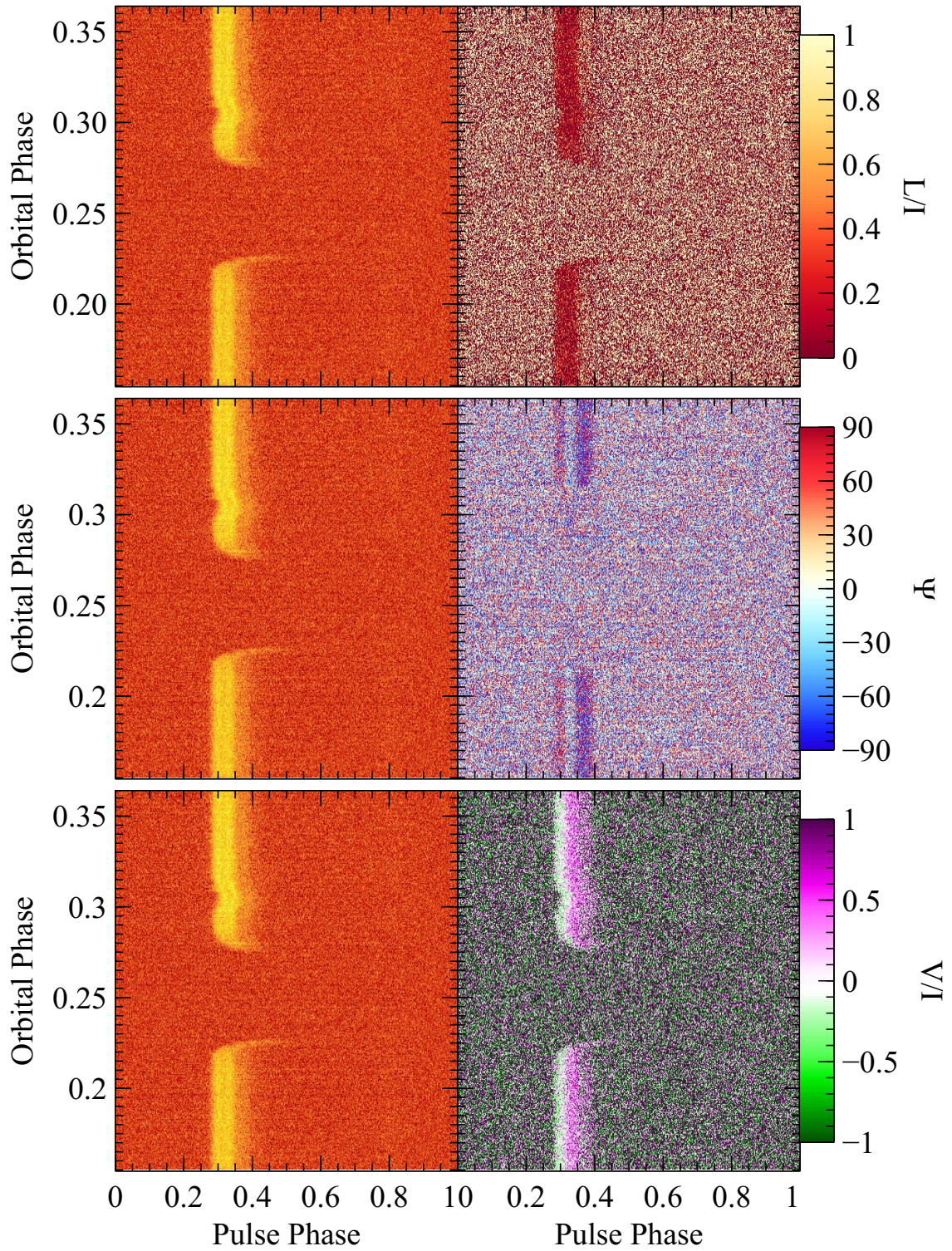


Figure 4.17: Higher time resolution close-up of polarization parameters in the GUPPI 820 MHz eclipse region. All left-hand plots show the total intensity I for reference

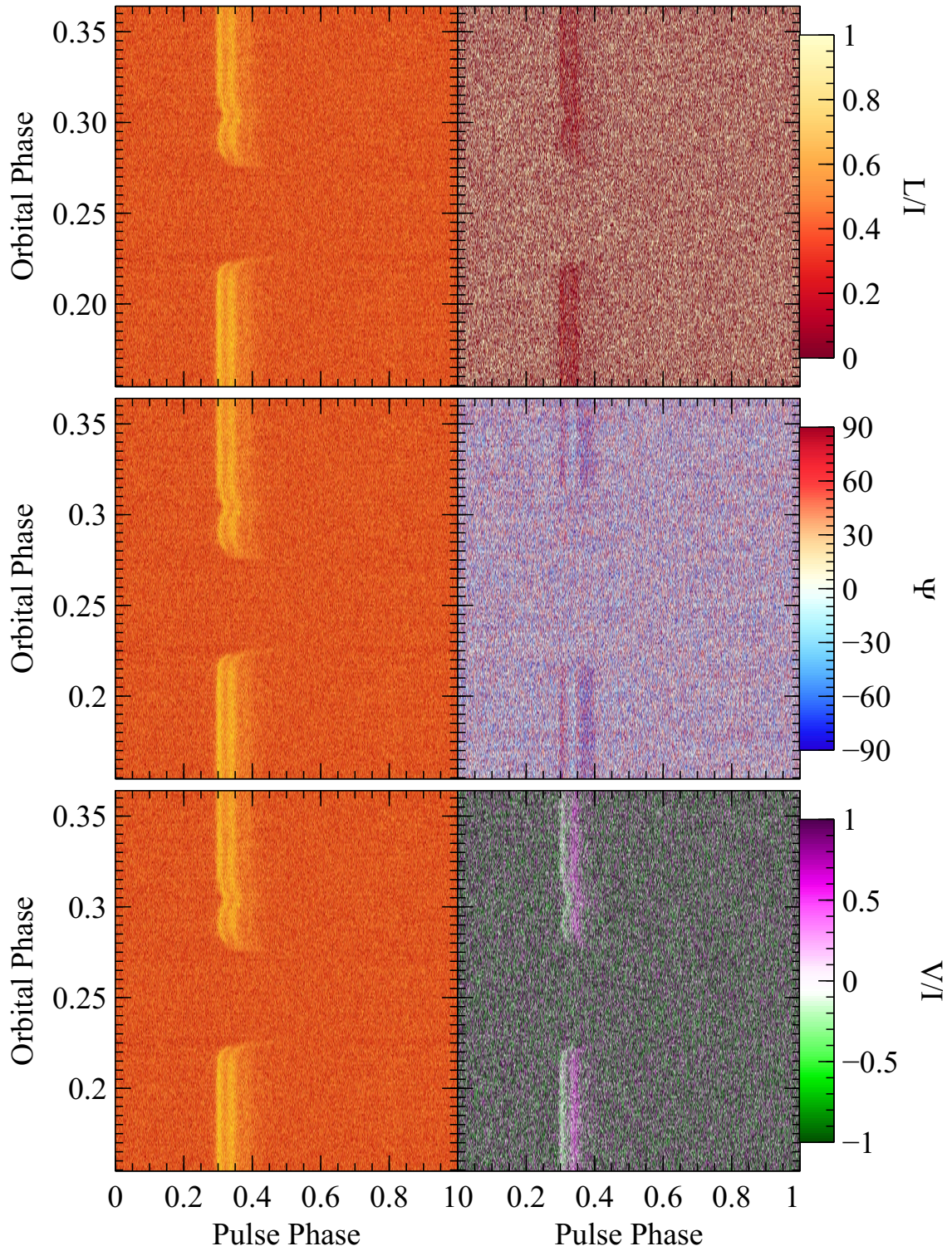


Figure 4.18: Higher time resolution close-up of polarization parameters in the GASP 820 MHz eclipse region. All left-hand plots show the total intensity I for reference

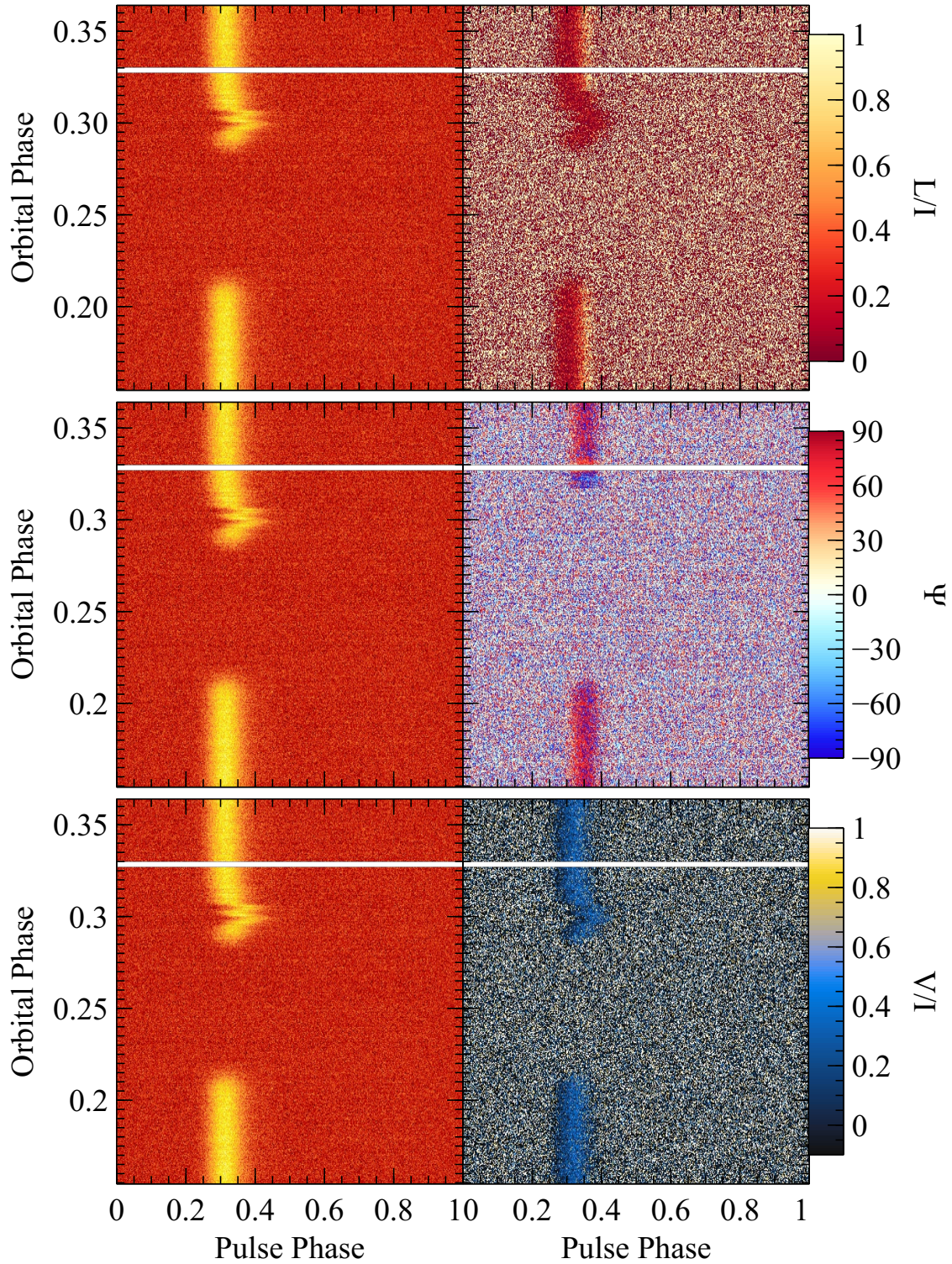


Figure 4.19: Higher time resolution close-up of polarization parameters in the GUPPI 350 MHz eclipse region. All left-hand plots show the total intensity I for reference. The horizontal white line is where sub-integrations were zero-weighted due to RFI

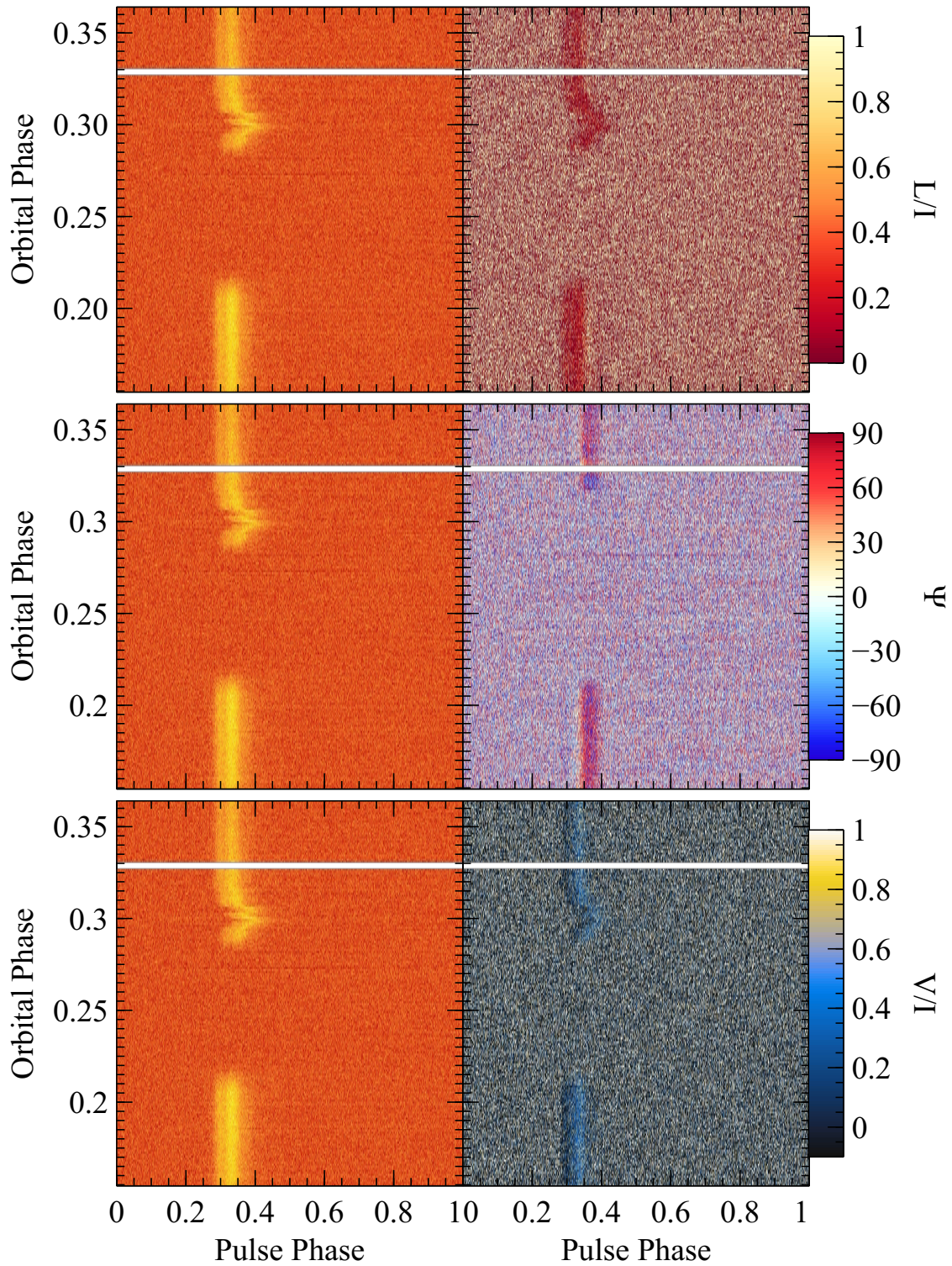


Figure 4.20: Higher time resolution close-up of polarization parameters in the GASP 350 MHz eclipse region. All left-hand plots show the total intensity I for reference. The horizontal white line is where sub-integrations were zero-weighted due to RFI

To prevent extreme values in the off-pulse regions from dominating in plots of either degree of polarization¹⁰, these scales have been restricted. However, allowing too large (or too small) a range makes the profile more difficult to discern. Based on the polarization profiles Figures 4.16 and 4.16 : for the 350 MHz plots both L/I was restricted to a range of 0 to 1 and V/I from -0.1 to 1; for 820 MHz plots L/I was given a range of 0 to 1 and the range for V/I was set to -1 to 1.

In Figures 4.17, 4.18, 4.19 and 4.20 we see no change between the GASP and GUPPI plots, other than a higher SNR in the GUPPI plots due to its wider bandwidth. Therefore the discussion below refers to only the GUPPI figures.

At 820 MHz (Figure 4.17) we see profile shapes emerging from the noise. L/I is difficult to see, and would be especially difficult to relate back to the profile shape in Figure 4.16. There is a clear trough of zero or low linear polarization followed by the suggestion of a possible peak to its right. For Ψ , due to the wrap between -90° and 90° , we can clearly see both outer slopes of the polarization position angle (PA) profile shape. The PA slope in the central pulse section (between approximately 0.32 and 0.35 in pulse phase in Figure 4.16) occurs close to 0° and it is unclear if it can be seen at all in Figure 4.17. V/I is the only plot for which we can discern all the features of its polarization profile - the negative dip on the left, then (looking to the right) it passes through zero to one peak and then drops to a lower second peak.

Interestingly, while the eclipse in V follows that in I , the PA clearly does not and the PA profile is only recovered after the blip. There is also a hint that the peak in the L/I plot also disappears in this region, leaving only a zero-linear polarization trough.

Turning to 350 MHz (Figure 4.19) this behaviour is clear. V/I follows I nicely - the pulsar's circular polarization has not been altered, but L/I is zero or very low for the blip, with its peak completely disappearing. When the PA reappears after the blip, it has clearly been altered before it then resumes its regular profile. Unfortunately, exactly at the point of this transition back to "normal", some transient RFI occurred and thus those sub-integrations are not usable.

¹⁰e.g., from dividing a spike in the noise of the Stokes V by a dip in the noise of the intensity. The polarization position angle does not have this issue as its range wraps

As the SNR is very low for individual sub-integrations; to investigate further, scans were tscrunched with 16 sub-integrations summed together. Note that in Figure 4.21 this makes it falsely appear that the data completely cover the region over which the PA transitions back to normal.

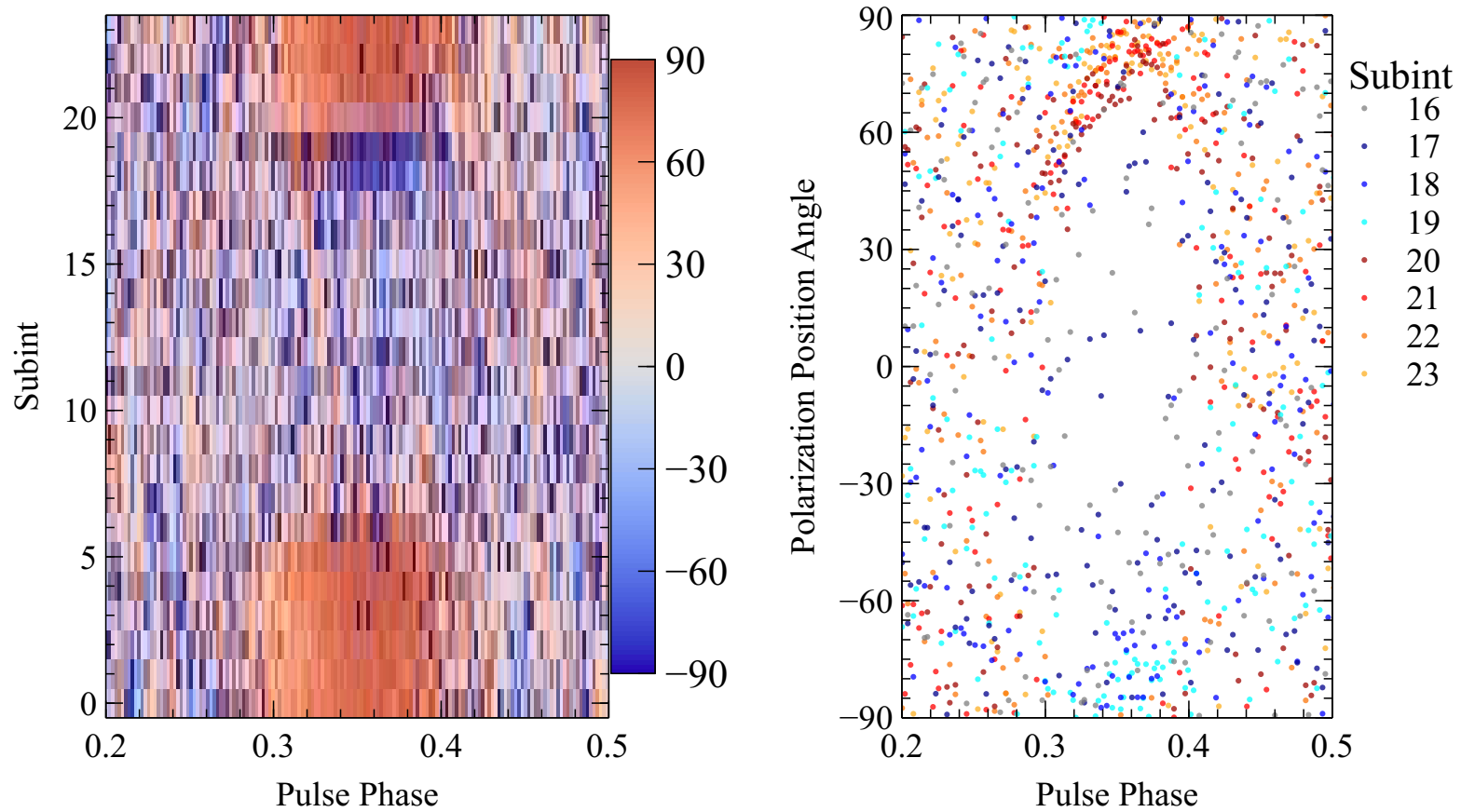


Figure 4.21: tscrunch map of Ψ at 350 MHz on MJD 55 191 next to over-plotted PA plots for select sub-integrations, both zoomed in on the pulse

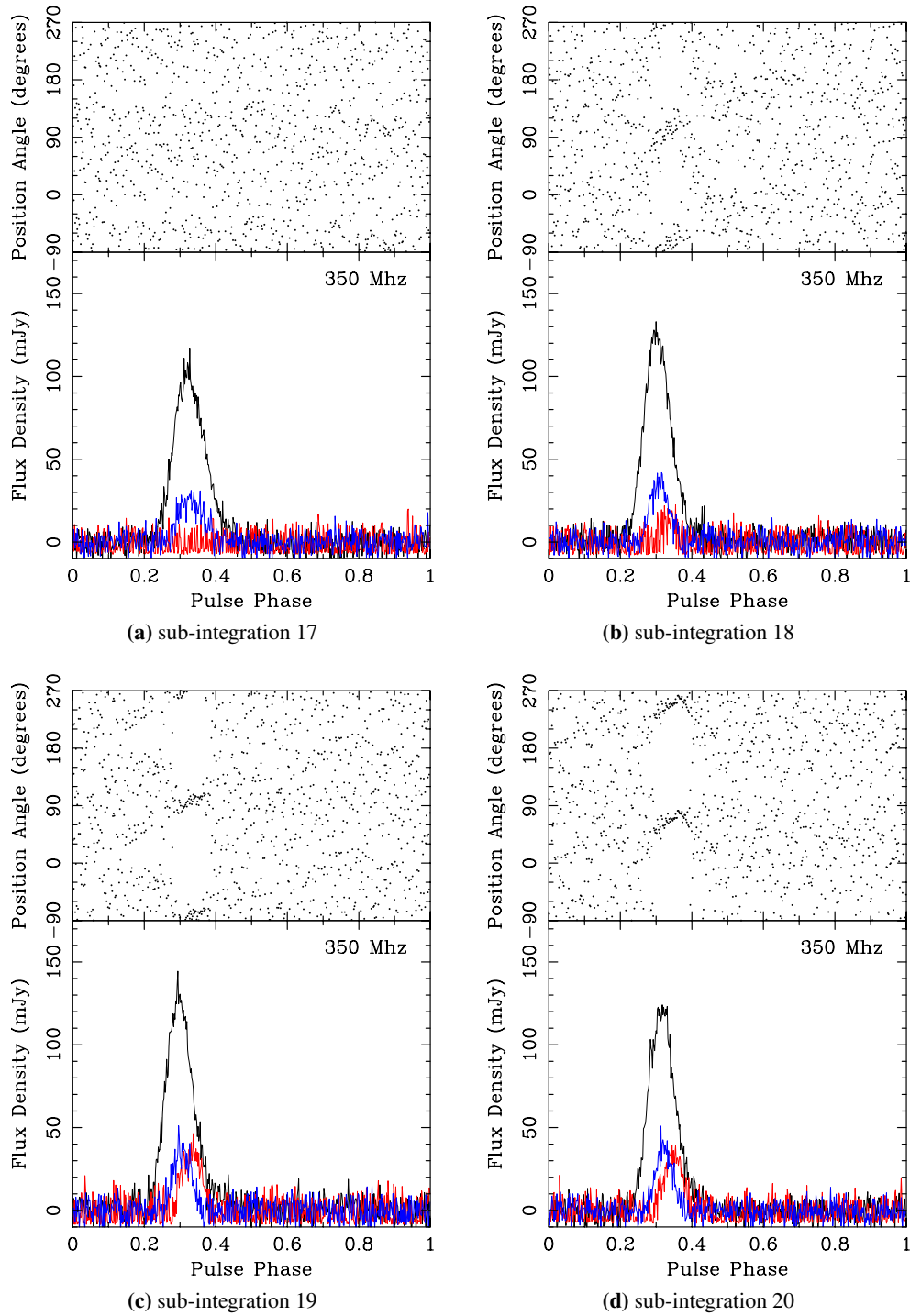


Figure 4.22: tscrunch polarization profiles for select sub-integrations at 350 MHz on MJD 55191

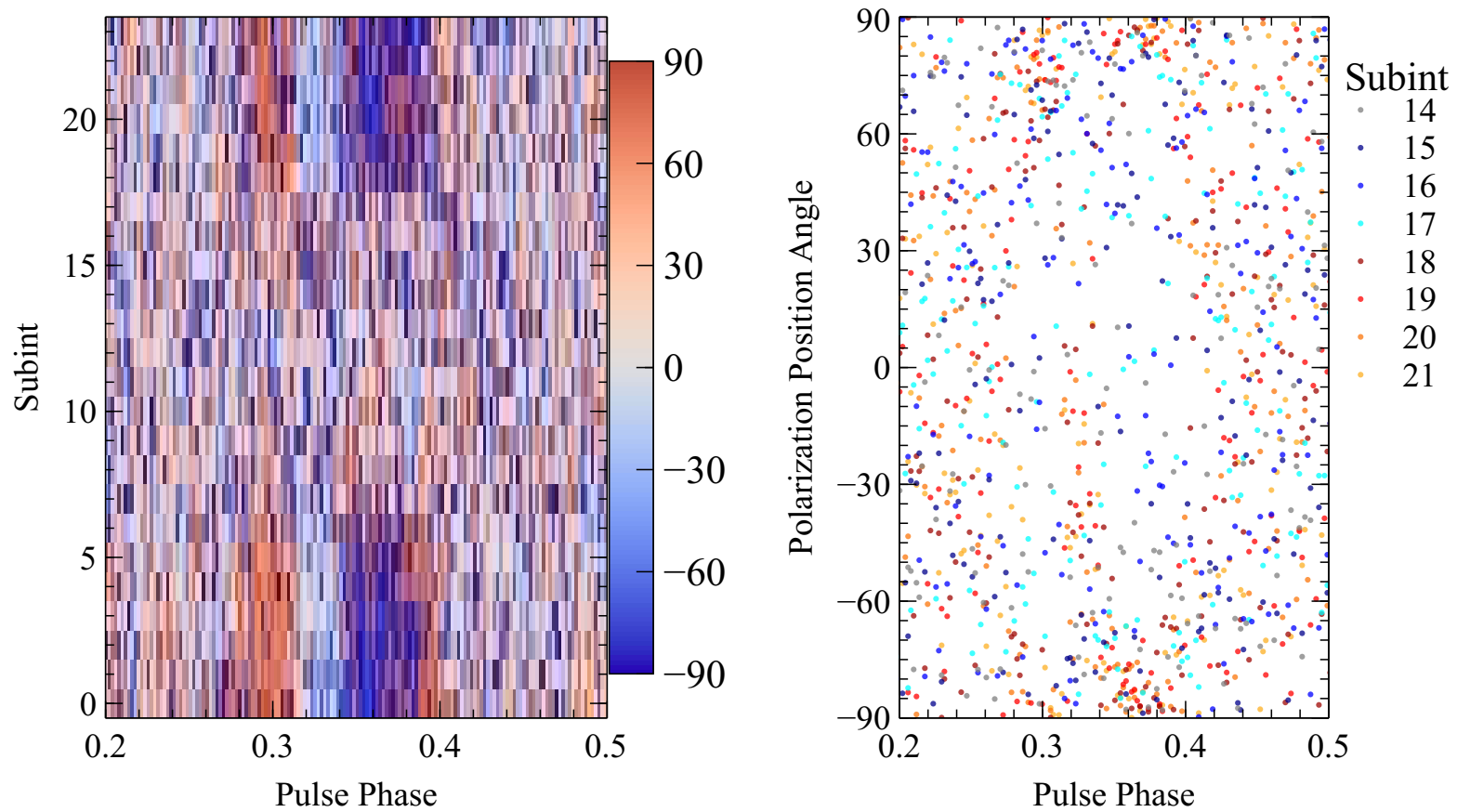


Figure 4.23: tscrunch map of Ψ at 820 MHz on MJD 55 181 next to over-plotted PA plots for select sub-integrations, both zoomed in on the pulse

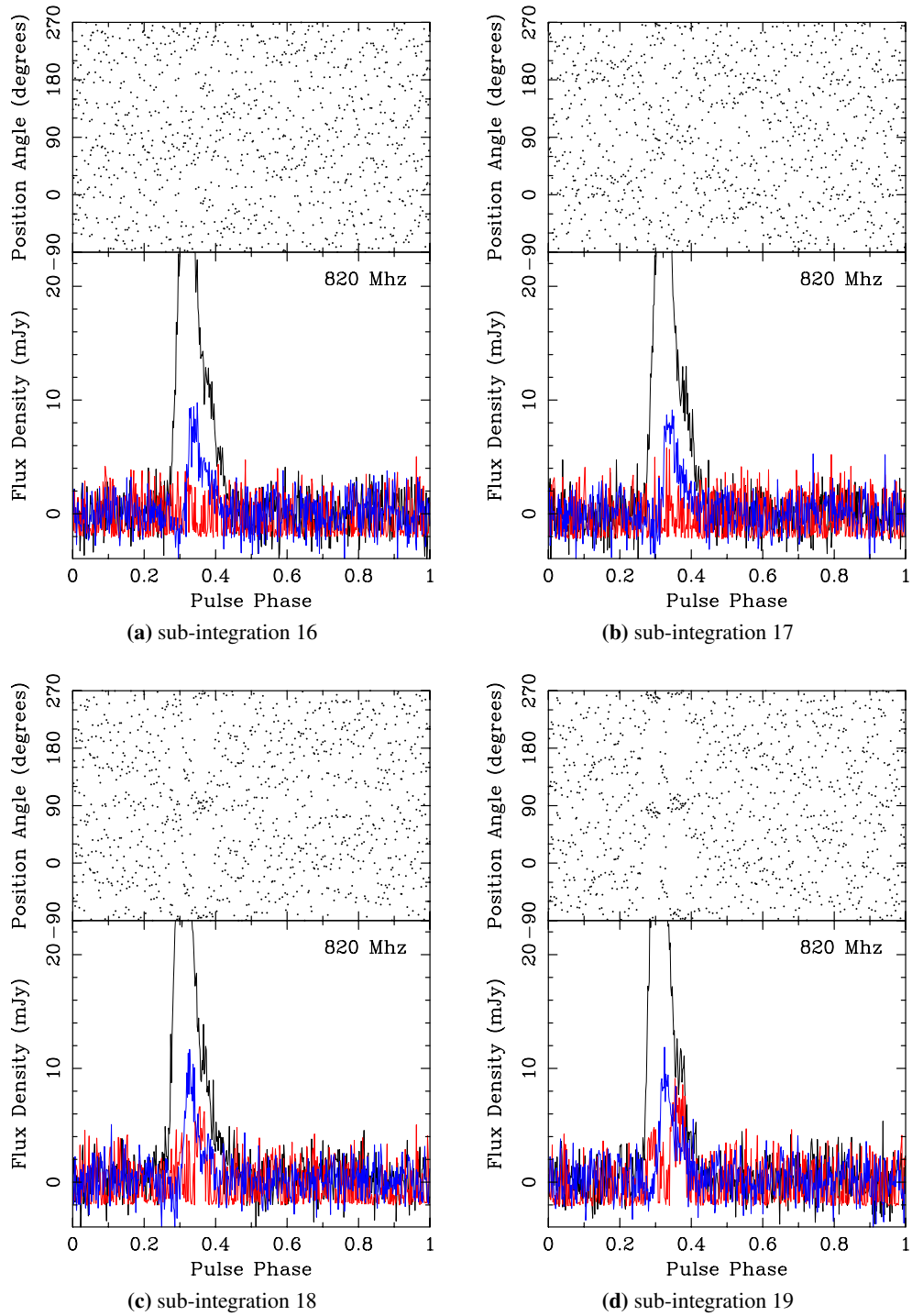


Figure 4.24: tscrunch polarization profiles for select sub-integrations at 820 MHz on MJD 55 181, zoomed in on the baseline to make changes in L more apparent

Figure 4.21 on the left shows the same observation and time-period as Figure 4.19, but the sub-integrations have been summed together, 16 at a time, and we have zoomed in to the on-pulse region on the x-axis. Sub-integrations 16 to 23 were then selected - over this range the pulsar signal exits the blip and recovers its initial form. PA profiles for these select sub-integrations were then plotted over each other to form the plot on the right. We see that upon exiting the blip the PA profile seems to have the same shape but has been shifted up (and is then wrapped down to the bottom of the PA's range).

Figure 4.22 shows polarization profiles for sub-integrations 17 to 20 for the same observation; we can clearly see a progression from zero linear polarization to a growing L with an above-average Ψ , to the usual profile form. There may be a suggestion in Figure 4.22b that when the PA profile first reappears after the blip, it has a steeper shape, but this is clearly not conclusive.

Figures 4.23 and 4.24 are equivalent plots for the 820 MHz observation on MJD 55 181. The SNR is too low for any PA shift, if it occurs, to be detected, but these figures do confirm the pulsar signal has no linear polarization during the blip.

We conclude the clump or clumps of material causing the blips are linearly depolarizing the pulsar signal but leaving the circular polarization unaffected.

Figure 4.25 shows the PA profiles shown in Figure 4.21, wrapped into the range -45° to 135° and including their uncertainties (as output by PSRCHIVE). A quadratic function was fit (over the pulse phase range shown) to data from the GUPPI 350 MHz total polarization profile (Figure 4.16). We assume there are no measurable changes in the shape of the PA profile, and apply the same quadratic fit to sub-integrations 18 to 23 while allowing only the offset to vary.

From Figure 4.21, by sub-integrations 20 to 23 the pulse has “recovered” from the effects of the blip, however in Figure 4.25 sub-integration 20 appears to deviate from the shape of the other PA profiles between pulse phases ≈ 0.35 to 0.36 resulting in a lower fit line. Sub-integration 20 is the closest “recovered” sub-integration to the eclipse, and contains less data than the others as it includes the region which was corrupted by RFI. Therefore sub-integration 20 was neglected and the baseline offset for an un-shifted PA profile was calculated using the weighted mean of the

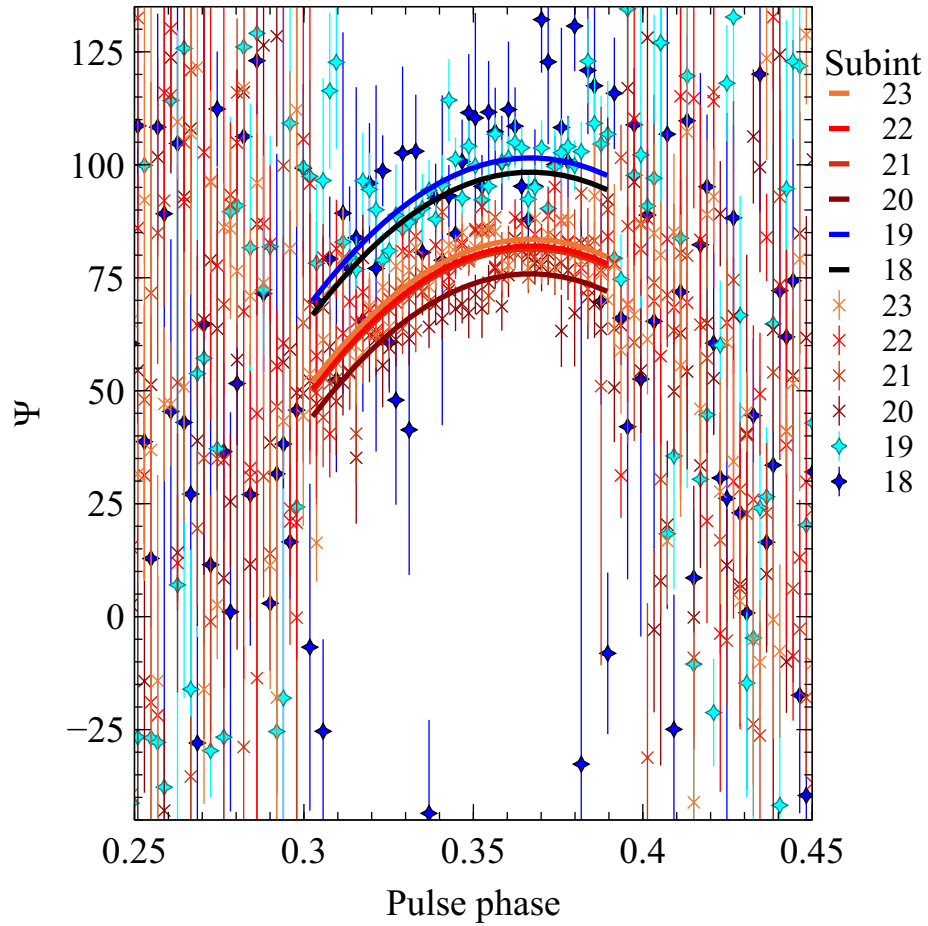


Figure 4.25: Fits for the PA profile of select sub-integrations (on MJD 55 191 at 350 MHz) to determine the PA shift. A quadratic was fit to the PA data from the total polarization profile (Figure 4.16), then only the y-intercept was allowed to vary as the fit was performed on the sub-integrations shown. Solid lines show the resulting fits and the range over which the functions were fit. Differentiating between fit lines for sub-integrations 21, 22 and 23 may be difficult as their offsets are very close

fits to sub-integrations 21 to 23.

The offsets fit to sub-integrations 18 and 19 agree within two sigma and a weighted mean of the two was taken to find the PA shift with respect to the baseline derived from sub-integrations 21 to 23. In this way we determine there was a $17.5(9)^\circ$ PA shift upon exiting the blip.

At a central frequency of 350 MHz, that shift would correspond to a RM of $0.42(2)$ rad/m². Given that (a) the timing of this PA shift - just after the blip - and (b) neither the ionosphere nor the galactic magnetic field are likely to change on this time scale, we are confident this shift is due to material in the system.

From the excess DMs calculated in Section 4.2, an average (including both GASP and GUPPI data) was calculated over the sub-integrations showing PA shifts (orbital phases 0.3175 to 0.3252 which would correspond to sub-integrations 18 and 19 in Figure 4.21). This gave an excess DM of $0.13(2) \times 10^{-3}$ cm⁻³pc in the PA shifted region. For comparison the average excess DM formed from later sub-integrations in the same observation, between orbital phases 0.34 to 0.37 (showing no PA shift), is $-0.027(11) \times 10^{-3}$ cm⁻³pc.

Combining the RM and DM in the PA shifted region gives a magnetic field along the line of sight of $3.9(6)$ mG ($3.9(6) \times 10^{-7}$ T). This is much larger than the Galactic magnetic field which is on the order of μ G [122, 123]. It is also much larger than the likely magnetic field of the pulsar at this distance. Assuming a simple dipole field, the magnetic field of the pulsar would have a $1/R^3$ dependence [124]; combining this with the derived value for the surface magnetic field given in Table 4.2 gives 0.17 nG.

Taking the location in orbital phase of the PA shifts to be the center of the range over which they were seen, then taking half that range as the uncertainty, the PA shifts occur at an orbital phase of $0.321(4)$. Assuming the material follows in the orbit of the companion as per Section 4.2 and taking the eclipse center as the location of that companion, we can estimate the distance between the companion and the location of our magnetic field component measurement. Using the inclination angle from the optical companion paper, this distance is $0.76(8) R_\odot$, assuming $i = 90$, it is $0.73(4) R_\odot$. In terms of the companion's effective Roche lobe radius,

results using either inclination angle correspond to $3.3(3)R_L$.

We believe this is the first successful detection of a line-of-sight magnetic field in eclipsing material in a BW or RB system. Notably for the original black widow pulsar, B1957+20, the line-of-sight magnetic field was measured as $-1.5(45)$ G before the eclipse and $0.4(10)$ G post-eclipse in 1990 [125]. As stated in Subsection 1.2.3 the Faraday effect rotates linear polarization causing PA shifts such as this one. A delay between the left- and right-handed circular polarizations is also introduced by Faraday rotation, and it is this delay that Fruchter et al. [125] were measuring. Following Fruchter et al. [125, Equation 4], with our dispersion delay and a $3.9(6)$ mG line of sight magnetic field, we would expect a delay between LCP and RCP of $0.14(3)$ ns. This is too small for us to detect and so is consistent with the observation of linear polarization changes with no corresponding change in the circular polarization.

Interestingly, for Ter5A, both polarization changes around eclipses and a high degree of eclipse variability with clumps of material remaining in the system have been seen [126]. The linear polarization was shown to fade out before the circular polarization upon entering an eclipse, and come back later after the eclipse exit. We do not see changes in the linear polarization preceding PSR J2256-1024's eclipse, but this may be due to the abruptness of the eclipse entry. Additionally, the same paper measured the RM of Ter5A and observed a high degree of variability with a 190 rad/m^2 average and 10 rad/m^2 standard deviation; as such, Ter5A would be a prime candidate for line of sight magnetic field measurements.

The possibility of a companion with magnetic field has been considered and thoroughly discussed for the Redback J1023+0038 in Archibald et al. [127]. If the eclipsing material of J1023+0038 is trapped in the companion's magnetosphere, the authors calculate the companion would need a field of 13 G to maintain that magnetosphere in the presence of the pulsar wind. Assuming an isotropic wind, and that the wind luminosity is equal to the pulsar's spin down power, the radiation pressure at the companion is given by

$$P_{wind} = \frac{\dot{E}_{rot}}{4\pi ca}$$

where a is the semi-major axis of the binary orbit. Setting this equal to the magnetic pressure we calculate the companion would need a magnetic field of at least 3.3 G to support a magnetosphere ¹¹. This number is several orders of magnitude above the measured magnetic field component; the companion could not support a magnetosphere under these assumed conditions. In reality the pulsar is unlikely to be 100 % efficient in converting spin down power into a pulsar wind, and the wind itself is unlikely to be isotropic [128]. In any case, we do detect a magnetic field within the material “blown” from the companion, even if the source of that field is uncertain.

¹¹Fields were calculated using all combinations of using 90° or $68(11)^\circ$ as the inclination angle, and correcting for galactic acceleration using either the distance derived from the parallax measurement or that from the DM and the YMW16 model. The value given is the minimum field resulting from these combinations

Chapter 5

Conclusion

We have used radio observations between MJDs 55005.385 and 56093.266 to compute a timing solution for PSR J2256-1024, a Black Widow (BW) pulsar in an eclipsing binary.

Data were taken at frequencies of 350 MHz, 820 MHz and 1500 MHz with the GBT, using GUPPI and GASP backend machines. This timing solution provides measurements of the pulsar’s coordinates, spin period, three period derivatives, Keplerian orbital parameters for the system, and a dispersion measure (which describes the number of free electrons along the line of sight).

Using these fitted parameters we are able to derive some properties of the pulsar including, but not limited to, its minimum surface magnetic field and a characteristic age. Using the YMW16 model for the electron density in the galaxy, we derive a distance of 2.0(6) kpc from the dispersion measure.

Combining parameters in this timing solution with an inclination angle found in a study of the optical companion [1], we find the pulsar is in a 5.109 183 1284(9) hour orbit with a semi-major axis of 4.1(3) lt – sec, and has a 0.0312(9) M_{\odot} companion with an effective Roche lobe radius of 0.232(2) R_{\odot} .

Comparing three radio observations of the eclipse we find a minimum radius for the eclipsing material of 0.42(4) R_{\odot} , approximately twice the radius of the companion’s Roche lobe. This confirms the “classic” picture of a BW where the

escaping material forms a cloud, partially trailing the companion, which is then larger than the companion itself. We also see at least one excess dispersion measure event in the region after PSR J2256-1024 has exited eclipse, likely due to a clump of material. From this we infer that the eclipsing cloud is probably clumpy itself and its exact structure may vary in time. We also find from examining polarization properties around the eclipse, that this (or these) clumps are causing Faraday rotation of the pulsar signal, corresponding to a measured rotation measure of $0.57(10)$ rad/m² on one occasion.

Combining this with an excess DM measurement at the same orbital phase from the same observation, we find a line-of-sight magnetic field of $3.9(6)$ mG occurring a minimum of $3.3(3)$ companion-Roche-lobe-radii from the companion's position. We believe this to be the first successful detection of a magnetic field component in eclipsing material within a BW or Redback (RB) system.

At each central frequency we also present a polarization profile and compute a mean flux density, resulting in a spectral index of $-1.56(17)$.

Due to the sparsity and length of the data set a reliable proper motion was unable to be determined; only one spin frequency derivative and no orbital frequency derivatives were measured. These are obvious targets for future observations and study. The orbital frequency derivative may be particularly interesting as we expect some orbital evolution for this system due to its Black Widow nature.

Similarly although variations in the dispersion measure are expected, due to the low number of multi-frequency epochs in the data set these were unable to be measured. In a system where we know there is excess material exiting the companion, studying DM variations could be particularly interesting. In addition, monitoring PSR J2256-1024 at a higher cadence around the eclipse region, looking for other excess DM events caused by clumps, could provide a very useful constraint for models of the escaping matter from the companion[129], and a constraint on the time-scale for variations within the eclipsing cloud. Given we observed a clump causing Faraday rotation (a frequency dependent phenomenon), polarization observations at lower frequencies, where the pulsar is also more powerful, are encouraged and could provide further magnetic field measurements in the system.

Bibliography

- [1] **R. P. Breton, et al.**; Discovery of the Optical Counterparts to Four Energetic Fermi Millisecond Pulsars; *The Astrophysical Journal* (2013): 769(2); 1302.1790 → pages xi, 22, 54, 60, 67, 101
- [2] **D. R. Lorimer and M. Kramer**; *Handbook of pulsar astronomy* (Cambridge University Press) (2004) → pages xiii, 3, 4, 9, 11, 19, 38, 58
- [3] **A. Hewish, et al.**; Observation of a Rapidly Pulsating Radio Source; *Nature* (1968): 217(5130):709–713 → pages 1
- [4] **S. J. Bell Burnell**; Little Green Men, White Dwarfs or Pulsars?; *Cosmic Search, Vol. 1, Issue 1, p.16* (1979): 1:16 → pages 1
- [5] **F. Pacini**; Energy Emission from a Neutron Star; *Nature* (1967): 216(5115):567–568 → pages 1
- [6] **T. Gold**; Rotating Neutron Stars as the Origin of the Pulsating Radio Sources; *Nature* (1968): 218(5143):731–732 → pages 1
- [7] **W. Baade and F. Zwicky**; On Super-Novae; *Proceedings of the National Academy of Sciences* (1934): 20(5):254–259 → pages 1
- [8] **W. Baade and F. Zwicky**; Cosmic Rays from Super-Novae; *Proceedings of the National Academy of Sciences* (1934): 20(5):259–263 → pages 1
- [9] **R. A. Hulse and J. H. Taylor**; Discovery of a pulsar in a binary system; *The Astrophysical Journal* (1975): 195:L51 → pages 2
- [10] **A. Wolszczan and D. A. Frail**; A planetary system around the millisecond pulsar PSR1257 + 12; *Nature* (1992): 355(6356):145–147 → pages 2
- [11] **M. D. Young, R. N. Manchester, and S. Johnston**; A radio pulsar with an 8.5-second period that challenges emission models; *Nature* (1999): 400(6747):848–849 → pages 2

- [12] **J. W. T. Hessels**; A Radio Pulsar Spinning at 716 Hz; *Science* (2006): 311(5769):1901–1904 → pages 2
- [13] **A. Burrows**; Colloquium : Perspectives on core-collapse supernova theory; *Reviews of Modern Physics* (2013): 85(1):245–261 → pages 3
- [14] **A. K. Harding**; Pulsar Emission Physics: The First Fifty Years; *IAU Symposium 337 "Pulsar Astrophysics: The Next Fifty Years"* (2017): 1712.02409 → pages 4
- [15] **D. Mitra**; Nature of Coherent Radio Emission from Pulsars; *Journal of Astrophysics and Astronomy* (2017): 38(3):52 → pages
- [16] **D. B. Melrose**; Coherent Emission Mechanisms in Astrophysical Plasmas; *Reviews of Modern Plasma Physics* (2017): 1(1):5; 1707.02009 → pages 4
- [17] **P. Goldreich and W. H. Julian**; Pulsar Electrodynamics; *The Astrophysical Journal* (1969): 157:869 → pages 4
- [18] **V. L. Ginzburg, V. V. Zheleznyakov, and V. V. Zatsev**; Coherent Radio-Emission Mechanisms and Magnetic Pulsar Models; *Soviet Physics Uspekhi* (1969): 12(3):378–398 → pages 4
- [19] **W. Becker** (Ed.) *Neutron Stars and Pulsars; Astrophysics and Space Science Library*, vol. 357 (Springer Berlin Heidelberg, Berlin, Heidelberg) (2009) → pages 4
- [20] **D. Bhattacharya**; Formation and evolution of binary and millisecond radio pulsars; *Physics Reports* (1991): 203(1-2):1–124 → pages 5
- [21] **I. H. Stairs**; Pulsars in Binary Systems: Probing Binary Stellar Evolution and General Relativity; *Science* (2004): 304(5670):547–552 → pages
- [22] **T. M. Tauris and E. van den Heuvel**; Formation and Evolution of Compact Stellar X-ray Sources; in **W. Lewin and M. van der Klis** (Eds.) *Compact stellar X-ray sources*; vol. 39; 623–665 (Cambridge University Press, Cambridge, UK) (2006): 0303456 → pages
- [23] **T. M. Tauris, N. Langer, and M. Kramer**; Formation of millisecond pulsars with CO white dwarf companions - II. Accretion, spin-up, true ages and comparison to MSPs with He white dwarf companions; *Monthly Notices of the Royal Astronomical Society* (2012): 425(3):1601–1627; 1206.1862 → pages 5

- [24] **A. M. Archibald, et al.**; A Radio Pulsar/X-ray Binary Link; *Science* (2009): 324(5933):1411–1414; 0905.3397 → pages 5, 8, 74
- [25] **N. R. Manchester**; ATNF Pulsar Catalogue; URL <http://www.atnf.csiro.au/research/pulsar/psrcat/> → pages 5
- [26] **R. N. Manchester, et al.**; The Australia Telescope National Facility Pulsar Catalogue; *The Astronomical Journal* (2005): 129(4):1993–2006; 0309219 → pages 5
- [27] **M. S. E. Roberts**; Surrounded by Spiders! New Black Widows and Redbacks in the Galactic Field; *Proceedings of the International Astronomical Union* (2012): 8(S291):127–132; 1210.6903 → pages 5
- [28] **A. S. Fruchter, D. R. Stinebring, and J. H. Taylor**; A millisecond pulsar in an eclipsing binary; *Nature* (1988): 333(6170):237–239 → pages 6, 64
- [29] **Z. Arzoumanian, A. S. Fruchter, and J. H. Taylor**; Orbital variability in the eclipsing pulsar binary PSR B1957+20; *The Astrophysical Journal* (1994): 426:85–88; 9312032 → pages 6
- [30] **A. S. Fruchter, et al.**; Optical detection and characterization of the eclipsing pulsar’s companion; *Nature* (1988): 334(6184):686–689 → pages 6
- [31] **M. T. Reynolds, et al.**; The light curve of the companion to PSR B1957+20; *Monthly Notices of the Royal Astronomical Society* (2007): 379(3):1117–1122 → pages 6
- [32] **S. R. Kulkarni and J. J. Hester**; Discovery of a nebula around PSR1957 + 20; *Nature* (1988): 335(6193):801–803 → pages 6
- [33] **H. H. Huang and W. Becker**; XMM-Newton Observations of PSR B1957+20; *Astronomy & Astrophysics* (2007): 463(2):L5–L8; 0612594 → pages 6
- [34] **R. H. H. Huang, et al.**; X-ray studies of the Black Widow Pulsar PSR B1957+20; *The Astrophysical Journal* (2012): 760(1):92; 1209.5871 → pages 6
- [35] **P. C. C. Freire**; Eclipsing Binary Pulsars; in **F. A. Rasio and I. H. Stairs** (Eds.) *Binary Radio Pulsars* (Aspen) (2004): 405; 0404105 → pages 7

- [36] **A. Patruno**; Millisecond Pulsar Catalogue; URL
<https://apatruno.wordpress.com/about/millisecond-pulsar-catalogue/> →
 pages 7
- [37] **E. Ergma and A. V. Fedorova**; Orbital evolution of binaries with
 ultra-rapid pulsars; *Astronomy and Astrophysics* (1992): 265(1):65–70 →
 pages 7
- [38] **P. Podsiadlowski, S. Rappaport, and E. Pfahl**; Evolutionary Binary
 Sequences for Low- and Intermediate-Mass X-ray Binaries; *The
 Astrophysical Journal* (2001): 565(2):1107–1133; 0107261 → pages 7
- [39] **H.-L. Chen, et al.**; Formation of Black Widows and Redbacks - Two
 Distinct Populations of Eclipsing Binary Millisecond Pulsars; *The
 Astrophysical Journal* (2013): 775(1):27; 1308.4107 → pages 8
- [40] **O. G. Benvenuto, M. A. De Vito, and J. E. Horvath**; Understanding the
 evolution of close binary systems with radio pulsars; *The Astrophysical
 Journal* (2014): 786(1):L7; 1402.7338 → pages 8
- [41] **J. Roy, et al.**; Discovery of PSR J1227-4853: A transition from a low-mass
 X-ray binary to a redback millisecond pulsar; *The Astrophysical Journal*
 (2014): 800(1):L12; 1412.4735 → pages 8
- [42] **A. Papitto, et al.**; Swings between rotation and accretion power in a binary
 millisecond pulsar; *Nature* (2013): 501(7468):517–520; 1310.7803 →
 pages 8
- [43] **D. F. Torres, et al.**; A Search for Transitions between States in Redbacks
 and Black Widows Using Seven Years of Fermi -LAT Observations; *The
 Astrophysical Journal* (2017): 836(1):68; 1612.07083 → pages 8
- [44] **H. J. Pletsch, et al.**; Binary Millisecond Pulsar Discovery via Gamma-Ray
 Pulsations; *Science* (2012): 338(6112):1314–1317 → pages 8
- [45] **J. M. Yao, R. N. Manchester, and N. Wang**; A New Electron Density
 Model for Estimation of Pulsar and FRB Distances; *The Astrophysical
 Journal* (2016): 835(1):29; 1610.09448 → pages 9, 55
- [46] YMW16 electron-density model; URL
<http://119.78.162.254/dmodel/index.php?> → pages 9, 55
- [47] **J. M. Cordes and T. J. W. Lazio**; NE2001.I. A New Model for the
 Galactic Distribution of Free Electrons and its Fluctuations; *ArXiv
 Astrophysics e-prints* (2002): 0207156 → pages 9, 55

- [48] Cordes-Lazio NE2001 Electron Density Model; URL <https://www.nrl.navy.mil/rsd/RORF/ne2001/model.cgi> → pages 9, 55
- [49] **T. H. Hankins and B. J. Rickett**; Pulsar signal processing; *Methods in Computational Physics. Volume 14 - Radio astronomy* (1975): 14:55 → pages 10
- [50] **R. N. Manchester and J. H. Taylor**; Parameters of 61 Pulsars; *Astrophysical Letters* (1972): 10:67–70 → pages 10
- [51] **J.-L. Han and R. Wielebinski**; Milestones in the Observations of Cosmic Magnetic Fields; *Chinese Journal of Astronomy and Astrophysics* (2002): 2(4):293–324; 0209090 → pages 11
- [52] **J. L. Han, et al.**; Pulsar Rotation Measures and the LargeScale Structure of the Galactic Magnetic Field; *The Astrophysical Journal* (2006): 642(2):868–881 → pages 12
- [53] **P. R. Brook, et al.**; Emission-rotation correlation in pulsars: new discoveries with optimal techniques; *Monthly Notices of the Royal Astronomical Society* (2016): 456(2):1374–1393; 1511.05481 → pages 12
- [54] **D. Mitra and J. M. Rankin**; On the Subpulse Modulation and Carousel Circulation Time of PSR B185726; *AIP Conference Proceedings* (2008): 983(1):109–111; 0712.1338 → pages 12
- [55] **J. H. Taylor**; Pulsar Timing and Relativistic Gravity; *Philosophical Transactions of the Royal Society A: Mathematical, Physical and Engineering Sciences* (1992): 341(1660):117–134 → pages 13, 35
- [56] **M. Born and E. Wolf**; *Principles of optics : electromagnetic theory of propagation, interference and diffraction of light* (Cambridge University Press); 7th edn. (1999) → pages 13, 17
- [57] **J. Tinbergen and Jaap**; *Astronomical polarimetry* (Cambridge University Press) (1996) → pages 14
- [58] **S. Trippe**; Polarization and Polarimetry: A Review (2014): 1401.1911 → pages 14
- [59] **C. Heiles**; A Heuristic Introduction to Radioastronomical Polarization; in **S. Stanimirovi, et al.** (Eds.) *SingleDish Radio Astronomy: Techniques and Applications*; vol. 278 (2002): → pages 14, 20

- [60] **R. C. Jones**; A New Calculus for the Treatment of Optical SystemsI
Description and Discussion of the Calculus; *Journal of the Optical Society
of America* (1941): 31(7):488 → pages 15
- [61] **G. G. Stokes**; On the Change of Refrangibility of Light; *Philosophical
Transactions of the Royal Society of London* (1852): 142(0):463–562 →
pages 15
- [62] **J. Naghizadeh-Khouei and D. Clarke**; On the statistical behaviour of the
position angle of linear polarization; *Astronomy and Astrophysics* (1993):
274:968 → pages 16
- [63] **J. E. Everett and J. M. Weisberg**; Emission Beam Geometry of Selected
Pulsars Derived from Average Pulse Polarization Data; *The Astrophysical
Journal* (2001): 553(1):341–357 → pages 16
- [64] **T. Robishaw**; *Magnetic fields near and far: Galactic and extragalactic
single-dish radio observations of the Zeeman effect*; Ph.D. thesis;
University of California, Berkeley (2008) → pages 16
- [65] **W. van Straten, et al.**; PSRCHIVE and PSRFITS: Definition of the Stokes
Parameters and Instrumental Basis Conventions; *Publications of the
Astronomical Society of Australia* (2010): 27(1):104–109; 0912.1662 →
pages 16
- [66] **J. D. Kraus and M. Tiuri**; *Radio astronomy* (McGraw-Hill) (1966) →
pages 16, 17
- [67] **C. Heiles, et al.**; Mueller Matrix Parameters for Radio Telescopes and
Their Observational Determination; *Publications of the Astronomical
Society of the Pacific* (2001): 113(788):1274–1288 → pages 20
- [68] **J. Boyles, et al.**; New Discoveries from the GBT 350-MHz Drift-Scan
Survey; in *AIP Conference Proceedings* (2011): 32–35 → pages 21
- [69] **A. A. Abdo, et al.**; Fermi Large Area Telescope First Source Catalog; *The
Astrophysical Journal Supplement Series* (2010): 188(2):405–436;
1002.2280 → pages 22
- [70] **A. A. Abdo, et al.**; The Second FERMI Large Area Telescope Catalog Of
Gamma-Ray Pulsars; *The Astrophysical Journal Supplement Series* (2013):
208(2):17 → pages 22, 84

- [71] Green Bank Observatory Proposer’s Guide for the Green Bank Telescope; URL <https://science.nrao.edu/facilities/gbt/proposing/GBTpg.pdf> → pages 24
- [72] **P. Demorest**; *Measuring the Gravitational Wave Background using Precision Pulsar Timing*; Ph.D. thesis; University of California, Berkeley (2007) → pages 27
- [73] **R. D. Ferdman**; *Binary pulsars: evolution and fundamental physics*; Ph.D. thesis; University of British Columbia (2008) → pages 27
- [74] **S. M. Ransom, et al.**; GUPPI: Green Bank Ultimate Pulsar Processing Instrument; in *American Astronomical Society, AAS Meeting #214, id.605.08; American Astronomical Society Meeting Abstracts #214*, vol. 214 (2009): → pages 27
- [75] **R. DuPlain, et al.**; Launching GUPPI: the Green Bank Ultimate Pulsar Processing Instrument; in *Advanced Software and Control for Astronomy II. Edited by Bridger*; vol. 7019 (2008): → pages 27
- [76] **D. L. Kaplan, et al.**; The Green Bank Telescope Pulsar Spigot; *Publications of the Astronomical Society of the Pacific* (2005): 117(832):643–653 → pages 27
- [77] **A. W. Hotan, W. van Straten, and R. N. Manchester**; PSRCHIVE and PSRFITS An Open Approach to Radio Pulsar Data Storage and Analysis; *Publications of the Astronomical Society of Australia* (2004): 21(3):302–309; 0404549 → pages 28, 74
- [78] **W. van Straten, P. Demorest, and S. Osłowski**; Pulsar data analysis with PSRCHIVE; *ArXiv Astrophysics e-prints* (2012): 1205.6276 → pages 28, 29
- [79] PSRCHIVE; URL <http://psrchive.sourceforge.net/> → pages 28, 30
- [80] **E. Petroff, et al.**; Identifying the source of perytons at the Parkes radio telescope; *Monthly Notices of the Royal Astronomical Society* (2015): 451(4):3933–3940; 1504.02165 → pages 28
- [81] **A. W. Hotan, M. Bailes, and S. M. Ord**; PSR J0737-3039A: baseband timing and polarimetry; *Monthly Notices of the Royal Astronomical Society* (2005): 362(4):1267–1272 → pages 34

- [82] **R. R. Coifman and D. L. Donoho**; Translation-Invariant De-Noising; in **A Antoniadis and G Oppenheim** (Eds.) *Wavelets and Statistics*; 125–150 (Springer, New York, NY) (1995): → pages 34
- [83] TEMPO; URL <http://tempo.sourceforge.net/> → pages 36
- [84] **R. T. Edwards, G. B. Hobbs, and R. N. Manchester**; Tempo2, a new pulsar timing package. II: The timing model and precision estimates; *Monthly Notices of the Royal Astronomical Society* (2006): 372(4):1549–1574; 0607664 → pages 36
- [85] **R. Blandford and S. A. Teukolsky**; Arrival-time analysis for a pulsar in a binary system.; *The Astrophysical Journal* (1976): 205:580 → pages 39
- [86] **S. M. Ord, S. Johnston, and J. Sarkissian**; The Magnetic Field of the Solar Corona from Pulsar Observations; *Solar Physics* (2007): 245(1):109–120 → pages 40
- [87] **X. P. You, et al.**; An Improved Solar Wind Electron Density Model for Pulsar Timing; *The Astrophysical Journal* (2007): 671(1):907–911; 0709.0135 → pages
- [88] **X. P. You, et al.**; Measurement of the electron density and magnetic field of the solar wind using millisecond pulsars; *Monthly Notices of the Royal Astronomical Society* (2012): 422(2):1160–1165 → pages 40
- [89] **Z. Arzoumanian, et al.**; The NANOGrav Nine-year Data Set: Observations, Arrival Time Measurements, and Analysis of 37 Millisecond Pulsars; *The Astrophysical Journal* (2015): 813(1):65; 1505.07540 → pages 41, 46
- [90] **S. Osłowski, et al.**; High signal-to-noise ratio observations and the ultimate limits of precision pulsar timing; *Monthly Notices of the Royal Astronomical Society* (2011): 418(2):1258–1271; 1108.0812 → pages 41
- [91] **R. M. Shannon, et al.**; Limitations in timing precision due to single-pulse shape variability in millisecond pulsars; *Monthly Notices of the Royal Astronomical Society* (2014): 443(2):1463–1481; 1406.4716 → pages 41
- [92] **W. van Straten**; Radio Astronomical Polarimetry and High-Precision Pulsar Timing; *The Astrophysical Journal* (2005): 642(2):1004–1011; 0510334 → pages 41

- [93] **P. D. Lasky, et al.**; Pulsar timing noise and the minimum observation time to detect gravitational waves with pulsar timing arrays; *Monthly Notices of the Royal Astronomical Society* (2015): 449(3):3293–3300; 1503.03298 → pages 41
- [94] **J. A. Ellis and N. J. Cornish**; Transdimensional Bayesian approach to pulsar timing noise analysis; *Physical Review D* (2016): 93(8):084048; 1601.00650 → pages 41
- [95] **S. M. Kopeikin**; Proper Motion of Binary Pulsars as a Source of Secular Variations of Orbital Parameters; *The Astrophysical Journal* (1996): 467(2):L93–L95 → pages 45
- [96] **M. J. Keith, et al.**; Measurement and correction of variations in interstellar dispersion in high-precision pulsar timing; *Monthly Notices of the Royal Astronomical Society* (2013): 429(3):2161–2174; 1211.5887 → pages 46
- [97] **P. B. Demorest, et al.**; Limits on the Stochastic Gravitational Wave Background from the North American Nanohertz Observatory for Gravitational Waves; *The Astrophysical Journal* (2013): 762(2):94; 1201.6641 → pages 46
- [98] **X. P. You, et al.**; Dispersion measure variations and their effect on precision pulsar timing; *Monthly Notices of the Royal Astronomical Society* (2007): 378(2):493–506; 0702366 → pages 46
- [99] **D. J. Nice and J. H. Taylor**; PSR J2019+2425 and PSR J2322+2057 and the proper motions of millisecond pulsars; *The Astrophysical Journal* (1995): 441:429 → pages 56, 57
- [100] **I. S. Shklovskii**; Possible Causes of the Secular Increase in Pulsar Periods.; *Soviet Astronomy, Vol. 13, p.562* (1970): 13:562 → pages 56
- [101] **K. Kuijken and G. Gilmore**; The mass distribution in the galactic disc - I. A technique to determine the integral surface mass density of the disc near the Sun; *Monthly Notices of the Royal Astronomical Society* (1989): 239(2):571–603 → pages 57
- [102] **T. Damour and J. H. Taylor**; On the orbital period change of the binary pulsar PSR 1913 + 16; *The Astrophysical Journal* (1991): 366:501 → pages 57

- [103] **M. J. Reid, et al.**; Trigonometric Parallaxes of High Mass Star Forming Regions: the Structure and Kinematics of the Milky Way; *The Astrophysical Journal* (2014): 783(2):130; 1401.5377 → pages 57, 58
- [104] **P. P. Eggleton**; Approximations to the radii of Roche lobes; *The Astrophysical Journal* (1983): 268:368 → pages 60
- [105] **I. M. Hook, et al.**; The GeminiNorth MultiObject Spectrograph: Performance in Imaging, LongSlit, and MultiObject Spectroscopic Modes; *Publications of the Astronomical Society of the Pacific* (2004): 116(819):425–440 → pages 60
- [106] **V. S. Dhillon, et al.**; ULTRACAM: an ultrafast, triple-beam CCD camera for high-speed astrophysics; *Monthly Notices of the Royal Astronomical Society* (2007): 378(3):825–840; 0704.2557 → pages 60
- [107] **F. A. Rasio, S. L. Shapiro, and S. A. Teukolsky**; What is causing the eclipse in the millisecond binary pulsar?; *The Astrophysical Journal* (1989): 342:934–939 → pages 67, 74
- [108] **R. Main, et al.**; Pulsar emission amplified and resolved by plasma lensing in an eclipsing binary; *Nature* (2018): 557(7706):522–525; 1805.09348 → pages 74
- [109] **J. S. Deneva, et al.**; Multiwavelength Observations of the Redback Millisecond Pulsar J1048+2339; *The Astrophysical Journal* (2016): 823(2):105; 1601.03681 → pages 74
- [110] **E. J. Polzin, et al.**; The low-frequency radio eclipses of the black widow pulsar J1810+1744; *Monthly Notices of the Royal Astronomical Society* (2018): 476(2):1968–1981; 1802.02594 → pages 74
- [111] **B. W. Stappers, et al.**; Probing the Eclipse Region of a Binary Millisecond Pulsar; *The Astrophysical Journal* (1996): 465(2):L119–L122 → pages 74
- [112] **A. Noutsos, et al.**; New pulsar rotation measures and the Galactic magnetic field; *Monthly Notices of the Royal Astronomical Society* (2008): 386(4):1881–1896 → pages 75
- [113] **R. T. Gangadhara**; Orthogonal polarization mode phenomenon in pulsars; *Astronomy and Astrophysics* (1997): 327:155–166; 9707168 → pages 76
- [114] **R. Ramachandran, et al.**; Effect of QuasiOrthogonal Emission Modes on the Rotation Measures of Pulsars; *The Astrophysical Journal* (2004): 606(2):1167–1173; 0401534 → pages 76

- [115] **C. Sotomayor-Beltran, et al.**; Calibrating high-precision Faraday rotation measurements for LOFAR and the next generation of low-frequency radio telescopes; *Astronomy & Astrophysics* (2013): 552:A58 → pages 78
- [116] International Reference Ionosphere; URL <https://iri.gsfc.nasa.gov> → pages 78
- [117] **W. M. Yan, et al.**; Rotation measure variations for 20 millisecond pulsars; *Astrophysics and Space Science* (2011): 335(2):485–498 → pages 78
- [118] **D. R. Stinebring, et al.**; Five Years of Pulsar Flux Density Monitoring: Refractive Scintillation and the Interstellar Medium; *The Astrophysical Journal* (2000): 539(1):300–316 → pages 84
- [119] **F. Jankowski, et al.**; Spectral properties of 441 radio pulsars; *Monthly Notices of the Royal Astronomical Society* (2018): 473(4):4436–4458; 1709.08864 → pages 84
- [120] **M. Kuniyoshi, et al.**; Low-frequency spectral turn-overs in millisecond pulsars studied from imaging observations; *Monthly Notices of the Royal Astronomical Society* (2015): 453(1):828–836; 1507.03732 → pages 84
- [121] **D. A. Frail, et al.**; Known Pulsars Identified in the GMRT 150 MHz All-Sky Survey; *The Astrophysical Journal* (2016): 829(2):119 → pages 84
- [122] **R. Jansson and G. R. Farrar**; A New Model of the Galactic Magnetic Field; *The Astrophysical Journal* (2012): 757(1):14; 1204.3662 → pages 98
- [123] **R. Jansson and G. R. Farrar**; The Galactic Magnetic Field; *The Astrophysical Journal* (2012): 761(1):L11; 1210.7820 → pages 98
- [124] **J. D. Jackson and R. F. Fox**; Classical Electrodynamics, 3rd ed .; *American Journal of Physics* (1999): 67(9):841–842 → pages 98
- [125] **A. S. Fruchter, et al.**; The eclipsing millisecond pulsar PSR 1957 + 20; *The Astrophysical Journal* (1990): 351:642–650 → pages 99
- [126] **A. Bilous**; *Single-Pulse Study of Radio Pulsars*; Ph.D. thesis; University of Virginia (2010) → pages 99
- [127] **A. M. Archibald, et al.**; Long-Term Radio Timing Observations of the Transition Millisecond Pulsar PSR~J1023+0038 (2013): 1311.5161 → pages 99

- [128] **S. S. Komissarov and Y. E. Lyubarsky**; Synchrotron nebulae created by anisotropic magnetized pulsar winds; *Monthly Notices of the Royal Astronomical Society* (2004): 349(3):779–792 → pages 100
- [129] **Alessandro Ridolfi**; *Probing Eclipse Mechanisms in Black Widow Pulsars and Redbacks: Development of a Code and its Applications*; Ph.D. thesis; Sapienza University of Rome (2012) → pages 102

Appendix A

Supporting Materials

PSR		2256-10
RAJ	22 ^h 56 ^m 56.39273355 ^s	1 0.00002162
DECJ	-10° 24 ^m 34.3768536 ^s	1 0.0008202
PX	0.5101	1 0.1444
POSEPOCH		55549.0000
F0	435.8187550969490189	1 0.0000000000018967
F1	-2.156043842255 × 10 ⁻¹⁵	1 1.270396355151 × 10 ⁻¹⁹
PEPOCH		55549.000000
START		55005.385
FINISH		56093.266
DM	13.776020	1 0.000003
SOLARN0		5.00
EPHEM		DE436
CLK		TT(BIPM)
UNITS		TDB
TIMEEPH		FB90
T2CMETHOD		TEMPO
CORRECT_ TROPOSPHERE		N
PLANET_ SHAPIRO		N
DILATEFREQ		N
NTOA		773
TRES		0.99
TZRMJD		55980.83119322229112
TZRFRQ		352.147
TZRSITE		GB
MODE		1
NITS		1
BINARY		BTX
A1	0.082965761	1 0.000000052
E		0.0000000000
T0	55548.9243523884	1 0.0000000615
OM		0.000000000000
FBO	5.436833458453 × 10 ⁻⁵	1 9.468814216737 × 10 ⁻¹⁵
JUMP -f Rcvr1_ 2_ GUPPI		-0.000001062
JUMP -f Rcvr1_ 2_ GASP		-0.000003444
JUMP -f Rcvr_ 800_ GASP		0.000003369
JUMP -f Rcvr_ 350_ GASP		0.000015772
JUMP -f Rcvr_ 342_ GUPPI		-0.000000186

Table A.1: Complete parameter file as output by TEMPO

(i) Using TEMPO Fit Parameters			
Symbol	Description	Value	
\dot{F}	F1, corrected for Galactic acceleration	$-2.055(12) \times 10^{-15} \text{ s}^{-2}$	
(ii) Assuming a Pulsar with Moment of Inertia 10^{38} kg m^2			
τ	Characteristic age	3.361(20) Gyr	
E_{rot}	Rotational kinetic energy	$3.74922559066686(3) \times 10^{44} \text{ J}$	$3.74922559066686(3) \times 10^{51} \text{ erg}$
\dot{E}_{rot}	Rate of change of rotational kinetic energy	$-3.535(21) \times 10^{27} \text{ W}$ $-9.24(5) L_{\odot}$	$-3.535(21) \times 10^{34} \text{ ergs}^{-1}$
B_{min}	Minimum surface magnetic field	$1.594(5) \times 10^4 \text{ T}$	$1.594(5) \times 10^8 \text{ G}$
(iii) Assuming a Pulsar Mass of $1.4 M_{\odot}$			
m_c^{min}	Minimum Companion Mass	$0.030248746(19) M_{\odot}$	

Table A.2: Alternate values for parameters in Table 4.2, where \dot{F} has been corrected for galactic acceleration using the parallax distance. Only parameters whose values were altered are listed

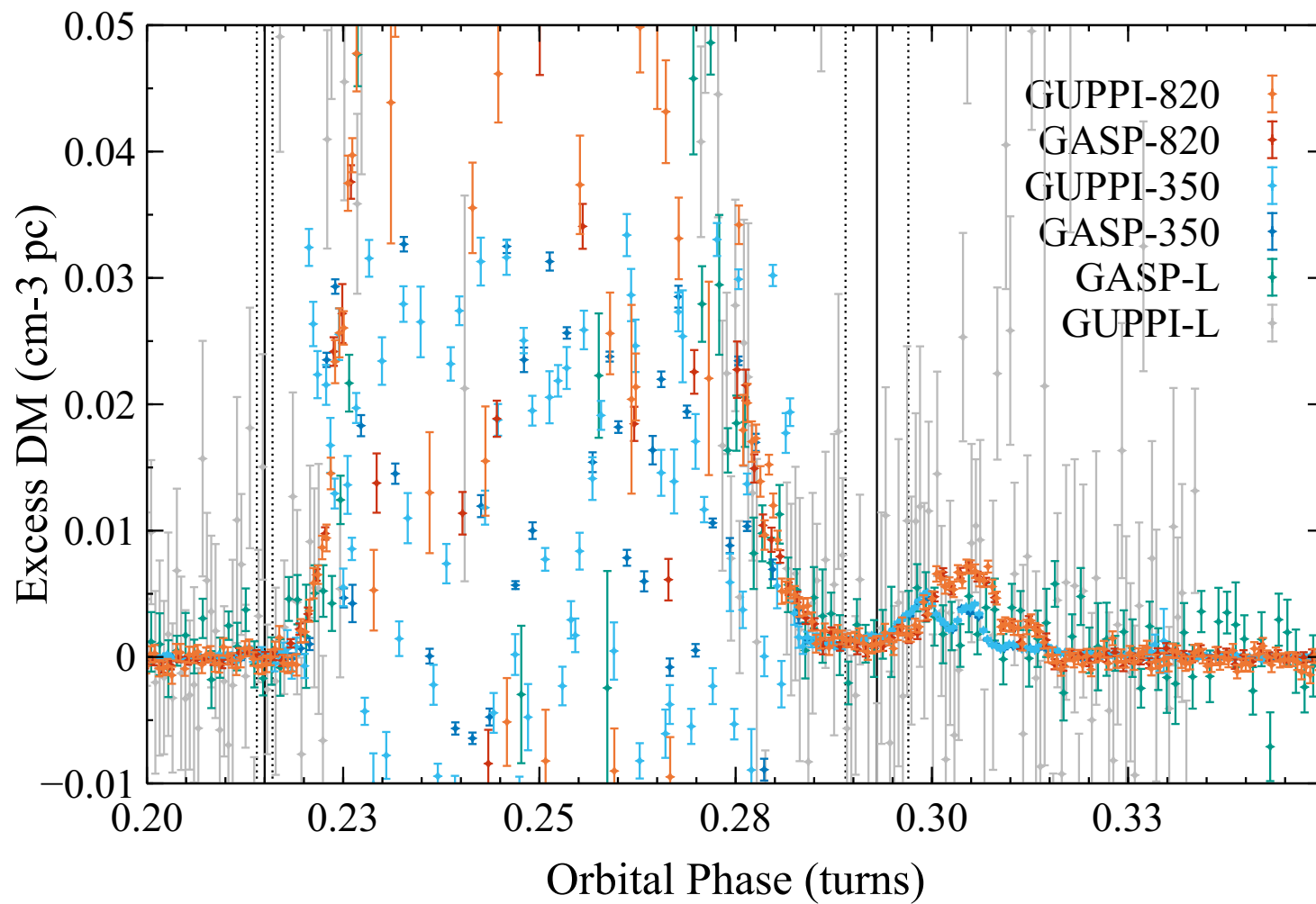


Figure A.1: Higher time resolution close-up of all eclipses observed: “Excess DM” vs Orbital Phase